Background Studies for Axion & WIMP Detection Experiments Using the XRPIX Silicon Detector

東京大学
THE UNIVERSITY OF TOKYO

Johnny Alejandro Mora Grimaldo

Department of Physics

The University of Tokyo

This dissertation is submitted for the degree of

Master of Science in Physics

Graduate School of Science

August 2017

To the memory of my grandfather

Acknowledgements

The author would like to acknowledge the joint efforts of the Axion-WIMP search group to the members of the Aihara-Yokoyama Laboratory in the University of Tokyo, and to Kuniko Kono. He also would like to express his gratitude to Tatsuki Ose for the dedicated work on the detector setup and the data taking, as well for pictures of the XRPIX FPGA and chip boards; to Yoshiyuki Onuki for the patient guidance and help during the elaboration of this work, and for the schematics of the XRPIX5b stack detector; to the XRPIX group for their critical thinking, and the pictures of the XRPIX2b and XRPIX5 chips, as well as for the original diagram of the XRPIX physical design; to Inoue Yoshizumi for his valuable efforts in measuring the radioactivity of the XRPIX5b board components; and to Shelvia Wongso, Irina Skudnova and Haochen Yan for their support in the first background measurements.

Abstract

The present text resumes the first feasibility study for an experiment aiming to stablish new bounds on the cross section $\sigma_{\chi,n}$ for the interaction between dark matter and baryonic matter, and the axion mass and scale parameter, by using the XRPIX silicon on insulator (SoI) pixel detector, developed by the University of Kyoto and KEK collaboration. This study was performed by analyzing the shielding properties of different geometrical configurations against the main expected background sources. The results indicate that, though an axion search is feasible, the current experimental setup is not adequate for dark matter studies. A suggested shielding scheme is also provided.

After evaluating the limits of the passive shields, the necessities of *1.* A more extensive background study and *2.* The use of active methods of background rejection were made clear. To solve both requirements, it was noted that pixel detectors respond differently to different kinds of radiation, and that this quality may be used to improve the energy resolution of the detector, search for radioactive background sources, and reject undesirable events. Hence, an analysis framework was developed, which aims to identify the type of particle hitting the detector according to the geometric properties of the cluster. In order to establish the parameters needed for identification, a detailed simulation of the detection process inside the XRPIX was also developed. The efficiency of this primary work was evaluated using ^{241}Am and ^{90}Sr data taken with the XRPIX2b chip model.

Table of contents

Chapter 1

Introduction

After the discovery of the Higgs boson on July of 2012, the last piece of the Standard Model of Particle Physics was set in place. However, as remarkable as this achievement is for the physics community, it is evident that our understanding of natural processes is far from complete. Indeed, problems like the baryon asymmetry, the hierarchy anomaly, the total number of Higgs bosons, and the stability of the proton are just some of the questions that motivate physicists to push forward the boundaries of the current scientific knowledge.

Two of the main unsolved problems in cosmology and high energy physics are the existence of a non-baryonic kind of matter, and the absence of a completely acceptable (under the current state of affairs) Charge-Parity-violating term in the strong interaction Lagrangian; these have come to be known as the Dark Matter and the Strong *CP* problems. Though relatively old (the Dark Matter hypothesis was already considered in 1932 by Jan Oort when observing the movement of some celestial bodies in the galaxy, whereas the Strong *CP* problem is as old as Quantum Chromo-Dynamics) the solution of these matters have eluded scientist until today.

In an attempt of delivering some insight to these questions, briefly explained in chapter 2, an experimental setup, which uses the newly developed XRPIX silicon pixel detector, aims to establish new limits in the physical properties of the WIMPs and the Axion, hypothetical particles that are meant to explain the Dark Matter and the Strong *CP* problem, respectively. The pilot ensemble consists of a thermal chamber, an air clean unit, an active shield scintillator, and passive lead and copper shielding, and is discussed in chapter 3.

The current work is the first feasibility study of this new experiment, and focuses on the behavior of the passive shields against the most important background sources for the experiment (in this first run, the axion is the main goal; hence, particles like photons and electrons constitute the gruesome of the discussion. Neutron background, though of primary importance for dark matter searches, is not considered, given that the current permeability of the experiment is not high enough to deliver new results) and on the response of the XRPIX to different kinds of radiation. In doing so, new tools, which can be used to study the electric properties of pixel detectors and to expand the field of applicability of the XRPIX detector, were developed. Chapter 4 depicts the first background analysis in which use was made of an CdTe detector in exchange of the XRPIX; it delivers a promising result for the axion search. Next, chapter 5 explains briefly the new tools developed for the XRPIX analysis: a clustering framework, which can group and identify different kind of clusters in the detector, and a simulation of the signal production process in the detector, which was used to get an insight in the cluster properties each kind of particle has. In chapter 6, the main results of this research are summarized, and some suggestions of future works are given, based on the limitations the current one had.

Chapter 2

Physics Motivations

In order to elucidate the spirit behind this study, this chapter gives a brief review of the physics underlying the axion and WIMP searches. Section 2.1 deals with the Strong *CP* Problem, the axion as its solution, and the experimental method for detecting it; section 2.2 then gives a short review on the evidence aiming to the existence of dark matter, introduces the weakly interactive massive particle (WIMP) as the preferred candidate for its constituent, and finally gives a small compendium of the analysis procedures used in establishing limits on the WIMPs physical properties.

2.1 The Axion

Though the Standard Model has proven to be astonishing adequate to describe the processes happening at quantum scales, and for a broad energy spectrum, there are still questions it does not provide an answer to; here, one of those questions is presented and the search for one of its possible solution constitutes the main physics motivation for the detection experiment being currently developed. It has come to be known as the Strong *CP* problem.

2.1.1 The Strong *CP* Problem

For starting, consider the QCD Lagrangian density:

$$\mathscr{L} = \overline{\psi}\left(i\not{D} - m\right)\psi - \frac{1}{4}G^{a}_{\mu\nu}G^{\mu\nu}_{a}. \tag{2.1}$$

This expression can be easily obtained by requiring for the physics model to be invariant under transformations of the $SU(3)$ group. This in turn, implies that in the solution there are eight[1] gauge bosons, which are associated with eight gluon fields. The first term in (2.1) represents the interaction of the quarks with the gluon fields, as well as the quark mass term; the second term corresponds to the strength of the gluons fields, and represents different kinds of self interaction processes. The field tensors $G^a_{\mu\nu}$ are defined by

$$G^a_{\mu\nu} = \partial_\mu A^a_\nu - \partial_\nu A^a_\mu + g f_{abc} A^b_\mu A^c_\mu \tag{2.2}$$

where f_{abc} are the structure constants of the Lie Algebra of the $SU(3)$ group; A^a_μ corresponds to the gluon vector field, and a is the index that distinguish among the eight gluons of the theory.

The necessity for gluons to be massless comes from the fact that a mass term for a gluon field A^a_μ, which would have the form

$$A^\mu_a m_a A^a_\mu$$

is not invariant under $SU(3)$ transformations. However, there is an extra term involving the tensor field in (2.2), which has been omitted under the assumption that (2.1) is invariant under CP transformations; this term corresponds to the expression

$$\mathscr{L}_{\text{CP viol.}} = \theta \frac{g^2}{32\pi^2} \tilde{G}^{a\mu\nu} G_{\sigma\rho a} \qquad\qquad \tilde{G}^{a\mu\nu} = \frac{1}{2}\varepsilon^{\mu\nu\sigma\rho} G^a_{\sigma\rho}, \tag{2.3}$$

which is invariant under charge conjugation, but not under parity transformations.

One would, at first sight, find for the axial current $j^{5\mu}$

$$\partial_\mu j^{5\mu} = \partial_\mu \left(\overline{\psi} \gamma^\mu \gamma^5 \psi \right) = 2m \overline{\psi} i \gamma^5 \psi \tag{2.4}$$

to be conserved when the fermion ψ is massless, so one would be tempted to postulate that $U(1)_A$ is a symmetry of QCD in the limit of vanishing quark masses. However, if this were true, there should exist a pseudo Nambu-Goldstone Boson (NGB) for this symmetry, with properties similar to the pions: the η meson. However, $m^2_\eta \gg m^2_\pi$, suggesting that this is not the case.

Indeed, a possible solution is obtained if one considers the existence of chiral anomalies and the true structure of the vacuum in gauge theories. The following conclusions derive from the treatment done by Peccei in [1, 2]. Though, from (2.4), it is expected for the axial current to have a vanishing divergence in the limit when $m \to 0$, this is not the case, for the

[1] remember, for a $SU(N)$ group there are $N^2 - 1$ generators; and, in a Yang-Mills theory, to each generator corresponds a boson field.

existence of triangle-like interactions (shown in figure 2.1) between one axial current $j^{\mu 5}$ and two vector currents $j^{\mu} = \overline{\psi}\gamma^{\mu}\psi$, induces an extra term in (2.4), which looks exactly like the one in equation (2.3). Effectively, for the $m \to 0$ limit it becomes

$$\partial_{\mu} j^{5\mu} = \frac{g^2}{32\pi^2}\tilde{G}^{a\mu\nu}G_{\sigma\rho a}.$$

For N_f flavors, the result generalizes to

$$\partial_{\mu} j^{5\mu} = \frac{g^2 N_f}{32\pi^2}\tilde{G}^{a\mu\nu}G_{\sigma\rho a}. \tag{2.5}$$

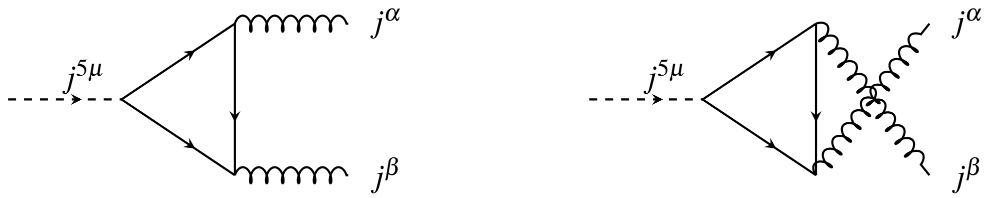

Fig. 2.1 Triangle diagrams for QCD, which add a nonvanishing term to the divergence of the axial current $j^{5\mu}$. A fine treatment of the mathematics can be found in [3].

It can be shown, however, that the pseudo-scalar term in the right part of equation (2.5) is the divergence of the quantity K^{μ} given by

$$K^{\mu} = \varepsilon^{\mu\nu\alpha\beta}A^{a}_{\alpha}\left(G_{\beta\gamma a} - \frac{g}{3}f_{abc}A^{b}_{\beta}A^{c}_{\gamma}\right), \tag{2.6}$$

so

$$\partial_{\mu}K^{\mu} = \tilde{G}^{a\mu\nu}G_{\sigma\rho a} \tag{2.7}$$

and one obtains that the action S of the theory is only modified by the surface term

$$\delta S \propto \int d\sigma_{\mu}K^{\mu}. \tag{2.8}$$

From here, using the naive boundary condition that the gauge fields A^{a}_{μ} should vanish at spatial infinity, one obtains $\delta S = 0$ and the $U(1)_A$ symmetry of the theory is restablished. However, the correct boundary condition is for the fields to be pure gauge fields at infinity. This is, $A^{a}_{\mu} = 0$ or a gauge transformation of zero. These transformations can be associated to vacuum to vacuum transitions in which the vacuum winding number changes by a certain, integer value ν [4]. This, in turn, postulates the existence of an infinite but discrete number of vacuum states, $|n\rangle$, defined by the winding number $n \in (-\infty, \infty)$, which can tunnel into each other through the action of the gauge fields A^{a}_{μ}. Wrongly, it was usually assumed that the vacuum of QCD corresponded to the state $|n=0\rangle$ and $A^a_\mu = 0$. Actually, these vacua form a basis of the vacum space, from which the true vacum state for QCD can be written. For this, it can be shown –see, for example, [4]– that there exists a unitary gauge transformation T such that $T\,|n\rangle = |n+1\rangle$. Since this is a gauge transformation, it commutes with the Hamiltonian, so eigenstates of T are also energy eigenstates; moreover, since it is a unitary operator, its eigenvalues should be of the form $e^{i\theta}$. One then has that an eigenstate $|\theta\rangle$ of T has the form

$$|\theta\rangle = \sum_n e^{in\theta}\,|n\rangle\,. \tag{2.9}$$

This, the so called θ-vacuum, corresponds to the true vacum of QCD. The new, more complex form of the vacuum, effectively adds a new term to the Lagrangian (2.1) [1, 2], so the new theory reads

$$\mathscr{L}_{\text{Corr}} = \overline{\psi}\left(i\not{D} - m\right)\psi - \frac{1}{4}G^a_{\mu\nu}G^{\mu\nu}_a + \theta\frac{g^2}{32\pi^2}\tilde{G}^{a\mu\nu}G_{\sigma\rho a}. \tag{2.10}$$

The existence of this CP violating term would have noticeable effects; in particular, it would lead to an observable electric dipole moment in the neutron [5, 6]. Current measurements [7] show a limit on the value for the electric dipole of $|d_N| < 6.3\times 10^{-26}\,e\cdot$ cm, which corresponds to an upper limit on the value of the angle θ of $\sim 10^{-10}$. If the fact that the mass matrix $\mathbf{M}$ for the Standard Model Lagrangian is usually complex, and for diagonalizing it one should perform a chiral transformation about an angle $\rho = \text{Arg}\left[\det\left(\mathbf{M}\right)\right]$, is also included, a transformed vacuum:

$$e^{i\rho Q_5}\,|\theta\rangle = |\theta+\rho\rangle$$

is obtained. Though, in principle, any value of the effective angle $\overline{\theta} = \theta+\rho$ is equally likely, the fact that it is very small has come to be known as the Strong *CP* Problem; or, in other words: why has nature chosen for QCD processes to respect CP symmetry, when it would be equally likely for them to violate it?

2.1.2 The Axion

Three main solutions have been postulated for the Strong *CP* problem [1, 8]: first, linking the angle value with the confinement property for quarks; this is, for $\overline{\theta}\neq 0$, the quarks would no longer be subject to asymptotic freedom. Then, the CP symmetry conservation would follow from the non-existence of free quarks.

The second solution is to postulate that CP is spontaneously broken, so one can set $\theta = 0$ at the Lagrangian level. However, experimental data seems to be in extremely good agreement with the CKM Model, where the CP is explicitly, and not spontaneously broken.

The final solution corresponds to the introduction of a new chiral symmetry, which, effectively, rotates the θ-vacua away. Two suggestions have been made to implement this symmetry: the first one corresponds to a massless u quark; the other postulates the existence of a new, global, $U(1)$ chiral symmetry. Currently, this one seems to be the most cogent solution the the Strong *CP* problem.

This symmetry –which has come to be known as a $U(1)_{PQ}$ symmetry– is necessarily spontaneously broken, and its introduction in the theory replaces the CP-violating angle $\overline{\theta}$ with a new field –the *axion*. The axion would be the NGB of this new symmetry, so under a $U(1)_{PQ}$ transformation, the axion field $\phi_{\mathrm{A}}(x)$ would translate

$$\phi_{\mathrm{A}}(x) \to \phi_{\mathrm{A}}(x) + \alpha f_A,$$

where f_A is the order parameter associated with the breaking of $U(1)_{PQ}$. The Standard Model Lagrangian would then be augmented by the axion interactions:

$$\mathscr{L}_{\text{total}} = \mathscr{L}_{\text{SM}} + \overline{\theta}\frac{g^2}{32\pi^2}\tilde{G}^{a\mu\nu}G_{\sigma\rho a} - \frac{1}{2}\left|\partial_\mu\phi_{\mathrm{A}}\right|^2 + \mathscr{L}_{\text{int}}\left[\partial_\mu\phi_{\mathrm{A}};\psi\right] + \xi\frac{\phi_{\mathrm{A}}}{f_A}\frac{g^2}{32\pi^2}\tilde{G}^{a\mu\nu}G_{\sigma\rho a} \tag{2.11}$$

where the last term is there to ensure that the $U(1)_{PQ}$ current indeed has a chiral anomaly; it also represents an effective potential for the axion field, which minimum occurs at $\langle a\rangle = -f_A\overline{\theta}/\xi$:

$$\left\langle\frac{\partial V_{\text{eff}}}{\partial\phi_{\mathrm{A}}}\right\rangle = -\frac{\xi}{f_A}\frac{g^2}{32\pi^2}\left\langle\tilde{G}^{a\mu\nu}G_{\sigma\rho a}\right\rangle\Big|_{\langle\phi_{\mathrm{A}}\rangle} = 0. \tag{2.12}$$

As explained in [9], the extra $U(1)_{PQ}$ theory, combined with the QCD effects, generates an effective potential for the action field which is periodic in $\overline{\theta} + \xi\left\langle\phi_{\mathrm{A}}\right\rangle/f_A$:

$$V_{\text{eff}} \sim \cos\left(\overline{\theta} + \xi\frac{\langle\phi_{\mathrm{A}}\rangle}{f_A}\right)$$

which is indeed minimal when $\langle\phi_{\mathrm{A}}\rangle = -f_a\overline{\theta}/\xi$. If the Lagrangian in (2.11) is written in terms of $\phi_{A,\text{phys}} = \phi_{\mathrm{A}} - \langle\phi_{\mathrm{A}}\rangle$, there is CP violating term no more. The mass of the axion is given by the expression

$$m_A^2 = \left\langle\frac{\partial^2 V_{\text{eff}}}{\partial\phi_{\mathrm{A}}^2}\right\rangle = -\frac{\xi}{f_a}\frac{g^2}{32\pi^2}\frac{\partial}{\partial\phi_{\mathrm{A}}}\left\langle\tilde{G}^{a\mu\nu}G_{\sigma\rho a}\right\rangle\Big|_{\langle\phi_{\mathrm{A}}\rangle}. \tag{2.13}$$

The explicit calculation for m_a has already been done [10]; here, only the solution [11] is reproduced, to leading order in chiral perturbation theory:

$$m_A = \frac{z^{1/2}}{1+z} \frac{f_\pi m_\pi}{f_A} \tag{2.14}$$

where $z = m_u/m_d$ is the ratio of the up and down quarks' masses, f_π is the pion decay constant, and $m_p i$ the pion mass.

Originally, the scale parameter of the theory, f_A, was thought to be of the same order of magnitude as the one for the electroweak breaking $v_F \approx 250$ GeV. However, this model has been ruled out by experiments since long ago. The reader can refer to figure 2.2 to confirm the major exclusion ranges for the values of f_A —and, consequently, for m_A. In the figure, two main models are used to establish these limits: the KSVZ and the DFSZ models; the first one introduces a scalar field σ such as $\langle\sigma\rangle = f_A$ and a superheavy quark Q, with mass $m_Q \sim f_A$ as the only ones carrying PQ charge. The DFSZ model adds to the PQ model a scalar field χ, which carries PQ charge and for which $\langle\chi\rangle = f_A$. For these two models, $f_A \gg v_F$, making the axion very light, very weakly coupled and very long lived. These properties have earned these models the name of invisible axion models.

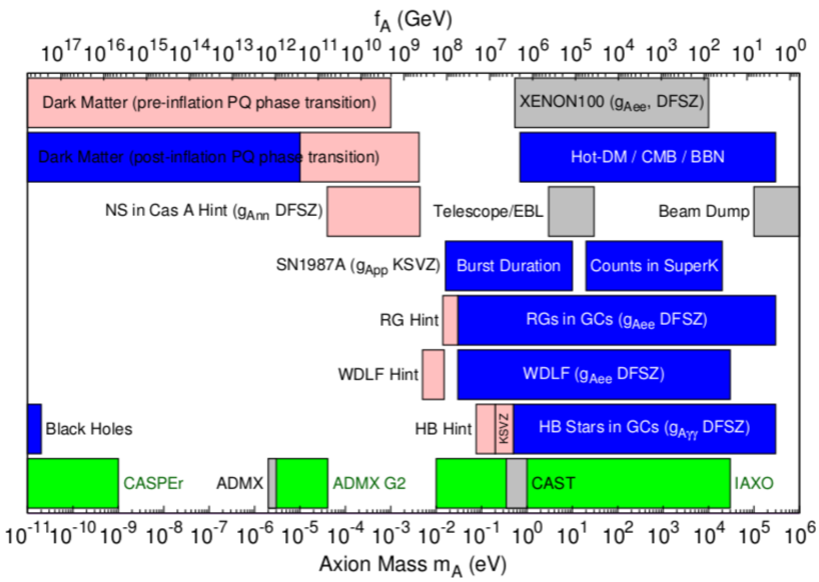

Fig. 2.2 Main exclusion ranges for the axion mass m_A (or, equivalently, for f_A). The green regions in the bottom correspond to the projected reach of the experiments. The limits on m_A and f_A are calculated using the KSVZ values for the coupling strengths of the axion to the other particles in the SM, and a value of $z = 0.56$, if not indicated otherwise. Image taken from [11].

2.1.3 Axions from the Sun

Through cosmological arguments (see, for example, [1]), one can establish a first upper limit to the *PQ* scale:

$$f_A < 3 \times 10^{11}\,\text{GeV} \qquad\qquad m_A > 2.1 \times 10^{-5}\,\text{eV}. \tag{2.15}$$

From here, and taking into account the excluded regions in figure 2.2, it is noticeable that there remains a window for the hadronic axion, around $3 \times 10^5\,\text{GeV} < f_A < 3 \times 10^6\,\text{GeV}$, which cannot be rulled out by existing arguments. Back in 1983, Sikivie [12] showed that the hadronic (KSVZ) axion, restricted to interact with the electromagnetic field through a chiral anomaly term of the form

$$\mathscr{L}_{A\gamma\gamma} = \kappa \frac{\phi_{\text{A,phys}}}{f_A} \frac{e^2}{12\pi^2} F_{\mu\nu}\tilde{F}^{\mu\nu} \qquad\qquad \tilde{F}^{\mu\nu} = \frac{1}{2}\varepsilon^{\mu\nu\sigma\rho}F_{\sigma\rho}, \tag{2.16}$$

couples with the electric and magnetic fields through the next equations

$$\nabla \cdot \overrightarrow{\mathbf{E}} = \frac{e^2}{3\pi^2 f_A} \overrightarrow{\mathbf{B}} \cdot \nabla\phi_{\text{A,phys}}, \qquad \nabla \times \overrightarrow{\mathbf{B}} - \frac{\partial \overrightarrow{\mathbf{E}}}{\partial t} = \frac{e^2}{3\pi^2 f_A}\left[\overrightarrow{\mathbf{E}} \times \nabla\phi_{\text{A,phys}} - \overrightarrow{\mathbf{B}}\frac{\partial \phi_{\text{A,phys}}}{\partial t}\right],$$
$$\Box a = \frac{e^2}{3\pi^2 f_A} \overrightarrow{\mathbf{E}} \cdot \overrightarrow{\mathbf{B}} - m_A^2 \phi_{\text{A,phys}} \tag{2.17}$$

and would then transform into a photon under the presence of a strong, inhomogeneous magnetic field; this process has come to be known as the Primakoff effect and it has been widely used to detect axions emitted from the sun [13, 14], where the former conditions are met. However, this method is strongly dependent on the axion-photon coupling parameter κ in equation (2.16), which is the least known parameter among those describing the low energy dynamics of the hadronic axion.

In 1995, Moriyama [15] noted that there is another mechanism which accounts for a very convenient axion source from the Sun: if some nuclides have magnetic dipole (M1) transitions and are excited thermally, axion emission from nuclear deexcitation would also be possible. He suggested to study the M1 transition of ^{57}Fe, since it is one of the stable iron isotopes, and it is exceptionally abundant among the heavy elements in the Sun; moreover, the transition energy is 14.4 keV, which would lead to a very distinctive, narrow peak in the measured spectrum. The whole process is resumed in figure 2.3.

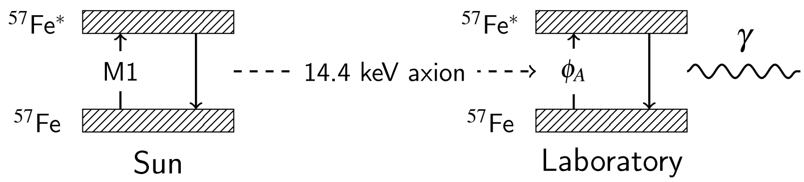

Fig. 2.3 Mechanism of axion production and detection. The deexcitation of an iron-57 nucleus in the sun is acompannied by the emission of a 14.4 keV axion, which reaches a piece of the same material —this is, of ^{57}Fe— in the laboratory. The nuclei of iron in the laboratory rises to its first excited level, and in the deexcitation process emits a 14.4 keV photon, which is captured by the detector.

The ^{57}Fe axion emission would involve the coupling of hadronic axions to nucleons. Srednicki [16] showed that the axion-nucleon interaction term can be written as

$$\mathscr{L}_{ANN} = \phi_{\mathrm{A,phys}} \overline{\Psi}_N i\gamma^5 \left(g_0 + g_3\tau_3\right) \psi_N, \tag{2.18}$$

where g_0 and g_3 are model dependent parameters, and τ_3 is a Pauli matrix in isospin space. For the KSVZ model one obtains [15]:

$$\begin{gathered} g_0 = -7.8\times 10^{-8}\left(\frac{6.2\times 10^6}{f_A/1\,\mathrm{GeV}}\right)\left(\frac{3F-D+2S}{3}\right) \\ \text{and} \\ g_3 = -7.8\times 10^{-8}\left(\frac{6.2\times 10^6}{f_A/1\,\mathrm{GeV}}\right)\left[(D+F)\frac{1-z}{1+z}\right], \end{gathered} \tag{2.19}$$

where D and F denote the reduced matrix elements of the $SU(3)$ octet axial vector currents, and S represents the total axial charge of the singlet current ($S = \Delta u + \Delta d + \Delta s$)[2].

S is a poorly constrained parameter; because of this, it is convenient to group the dependence on its value (and the dependence on the values of D, F and z as well) in the constant C defined as

$$C \equiv (D+F)\frac{1-z}{1+z} - 1.19\left(\frac{3F-D+2S}{3}\right). \tag{2.20}$$

Then, as explained in [15], the differential flux of axions coming from this M1 transition, at an axion energy $E_A = 14.4$ keV, can be shown to be

$$\Phi_A = 2C^2\left(\frac{10^6\,\mathrm{GeV}}{f_A}\right)^2 \times 10^{13}\mathrm{cm}^{-2}\mathrm{s}^{-1}\mathrm{keV}^{-1}. \tag{2.21}$$

[2] A similar, if somehow more complex treatment can be done for the DFSZ model; the biggest difference is that the DFSZ axion does couple at tree level with leptons and the Higgs bosons, which makes the algebra more laborious. The interested reader is compelled to review reference [16]

These axions are expected to excite a sample of ^{57}Fe in the laboratory. The rate of excitation per nucleus is [15]

$$R_N = \frac{\pi}{2}\Phi_A \sigma_{0,A}\Gamma_{\mathrm{tot}} \qquad\qquad \sigma_{0,A} = 2\sigma_{0,\gamma}\frac{\Gamma_A}{\Gamma_\gamma} \tag{2.22}$$

where $\sigma_{0,\gamma} = 2.6\times10^{-18}\,\mathrm{cm}^2$ is the maximum resonant cross section of γ rays —an analogous definition for axions would follow for $\sigma_{0,A}$—, $\Gamma_{\mathrm{tot}} = 4.7\times10^{-12}$ keV is the total decay width of the first excited state of ^{57}Fe, and Γ_A/Γ_γ represents the branching ratio of the ^{57}Fe excited state decay into an axion (Γ_A) and a photon (Γ_γ). This last value was calculated by Haxton and Lee in [17], and it happens to be

$$\frac{\Gamma_A}{\Gamma_\gamma} = \frac{1}{2\pi\alpha}\frac{1}{1+\delta^2}\left[\frac{g_0\beta + g_3}{(\mu_0-1/2)\,\beta+\mu_3-\eta}\right]^2, \tag{2.23}$$

with δ the electric quadrupole to magnetic dipole mixing ratio (E2/M1), μ_0 and μ_1 the isoscalar and isovector magnetic moments, and η and β nuclear-structure-dependent terms. The most common values for these parameters [15], as well as for z, are summarized in table 2.1.

Parameter	**Value**
δ	$\sim$0
β	-1.19
$\mu_0 - 1/2$	$\sim$0.38
μ_3	$\sim$4.71
η	0.8
z	0.56

Table 2.1 Values for the parameters used in the derivation of equations (2.21) and (2.24)

The total excitation rate per unit mass of ^{57}Fe would then be

$$R = 3C^4\left(\frac{10^6\,\mathrm{GeV}}{f_A}\right)^4 \times 10^2\mathrm{day}^{-1}\mathrm{kg}^{-1}. \tag{2.24}$$

The deexcitation of this nuclei, through the emission of a 14.4 keV photon, would then be detected. The counting of these photons would the be proportional to f_A^{-4} or to m_A^4. Common values of C and f_A give rates of around 3 events per day per kilogram of detector.

Former experiments have employed this technique to stablish new constrains on the axion's mass for the hadronic window. The first one was Namba [18], using silicon photoscintilators on opposite faces of the iron foil; the whole setup was cooled down to 205

Kelvin using a coldfinger, and used lead shields of 10 cm of thickness. Derbin et al [19] used a silicon planar detector, copper and iron shields, and cooled the detector down to liquid nitrogen temperatures (77.35 K); this experiment established the most recent limit on the axion mass by the means of iron foils. Assuming

$$g_0 = -4.03\times 10^{-8}\left(\frac{6\times 10^6\,\mathrm{GeV}}{f_A}\right) \qquad \text{and} \qquad g_3 = -2.75\times 10^{-8}\left(\frac{6\times 10^6\,\mathrm{GeV}}{f_A}\right)$$

as well as $z = 0.56$, and $S = 0.5$, they obtained that $m_A \leq 145$ eV at a 95% confidence level. A comparison between the background rates and the energy resolutions at 14.4 keV for both experiments is shown in table 2.2.

Experiment	**Background Rate ($\times 10^{-3}$ h$^{-1}\times$ mm$^{-2}\times$ keV^{-1})**	**Energy Resolution (FWHM at 14.4 keV)**
Namba (2007)	1.76	2.36 keV
Derbin (2011)	1.09	1.48 keV

Table 2.2 Background rates and energy resolution at 14.4 keV for former axion search experiments using ^{57}Fe.

The experimental setup discused in Chapter 2 aims to use the same principle for probing the existence of axions, using a new SOI pixel detector; it is expected to yield more constraining limits to the value of m_A, by lowering the background counts and improving the energy resolution in comparison with the experiments in table 2.2.

2.2 WIMP

Having considered the Strong *CP* problem, the attention is now turned to the second motivation for the experiment described in this work: that of the existence of an unidentified matter density that permeates the whole universe and whose existence, up to now, has been put in evidence without doubt only by its gravitational effects. As for the Strong *CP* problem, different solutions have been postulated, from which the existence of Weakly Interactive Massive Particles, or WIMPs, seems to be the most convincing.

2.2.1 Evidence of a New Kind of Matter

Consider now the formula for the velocity of bodies in a stable Keplerian orbit of radius is r around a galaxy:

$$v(r) = \sqrt{\frac{GM(r)}{r}} \tag{2.25}$$

where G is the gravitational constant, and $M(r)$ is the mass of the galaxy contained in a sphere of radius r. If the visible mass density $\rho(r)$ drops to zero for certain value R of r, one would expect the velocity $v(r)$, for values $r > R$, to behave like $v(r) \propto 1/\sqrt{r}$. However, one finds that the rotation speed becomes approximately constant for even the largest values of r for which the rotation curve can be meassured. This implies the existence of a mass density $\rho_D(r) \propto r^2$ which accounts for a mass term $M_D(r) \propto r$ that, however, is not observable through telescopes. This kind of matter, which at first seems only to interact through the gravitational force, has come to be called dark matter. Since the first observations on the gravitational potential of galaxy clusters [20], many other studies on cluster of galaxies have been performed, all of them pointing at the presence of an unobservable amount of matter [21], or to possible modifications of the equations governing the gravitational interactions [22, 23]; in [23] a comparison of the mass estimations for different methods is done. The discrepancies between the results from X-ray brightness observations and the ones obtained through the consideration of Newtonian gravitational effects are quite notorious; however non-Newtonian dynamics theories, such as MOND (Modified Newtonian Dynamics), or non-Newtonian gravitational theories, such as MSTG (Metric-Skew-Tensor Gravity), seem to adjust better to the data, without the need for the introduction of an unobservable mass source.

Currently, the most compelling piece of evidence for the existence of dark matter is the study of gravitational lensing in the Bullet Cluster (1E 0657-558), consisting of two colliding clusters of galaxies (see figure 2.4); these observations seem to present an irrefutable proof, independent of assumptions on the nature of the gravitational force law [24]. Using weak lensing to establish a gravitational potential map of the two clusters system, the centers of both clusters —where the mass concentration would be bigger— were traced to be spatially segregated from the X-ray baryonic plasma. This would imply that the biggest amount of mass in both clusters comes, not from the observable matter, but from a non-interacting dark matter, which would not experience ram pressure during the collision.

2.2.2 The WIMP

Set to the task of understanding what are the primary constituents of this non-baryonic dark matter, multiple hypothesis arise; however, all of the candidates should satisfy several conditions [25]: they must be stable on cosmological time scales, for otherwise they would have decayed by now; they should couple weakly with the electromagnetic field (owing to the name of *dark* matter); and they must have the right relic density Ω_{nbm}, as to fit [26]

$$\Omega_{\text{nbm}} h^2 = 0.1186 \pm 0.002 \tag{2.26}$$

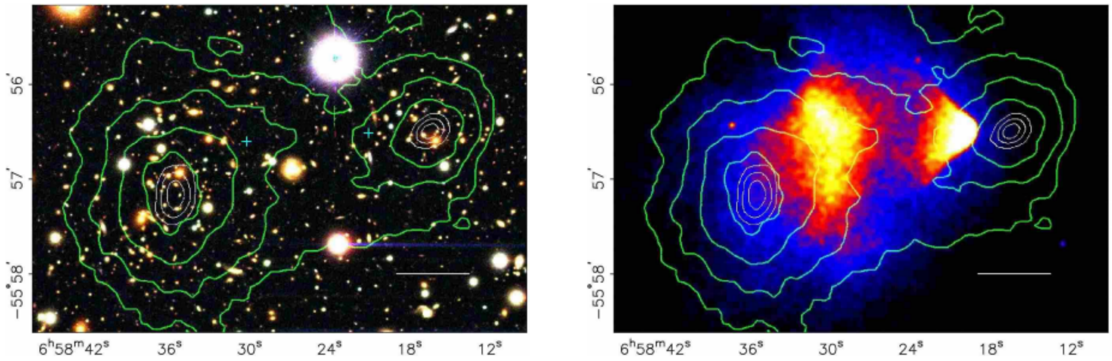

Fig. 2.4 Images of the bullet cluster. In the left, a photography of the cluster, with the gravitational potential map inferred from gravitational lensins superimosed. In the right, the same map over an X-ray image of the same cluster. It is seen that the regions with higher mass concentration (centers of the two circumferences) are not the ones where the baryonic mass (orange region) are. Image courtesy of [24].

where h is the Hubble constant in units of 100 km/(s·Mpc). The contribution of light neutrinos to this relic density has an upper bound of [26]

$$\Omega_\nu h^2 \leq 0.0062 \qquad \text{at} \qquad 95\%\text{C.L.} \tag{2.27}$$

From here, the candidates include primordial black holes, *axions* and WIMPs [25].

Though axions were originally postulated as a solution for the Strong *CP* problem, they constitute a candidate for non-thermal, cold, dark matter. The term non-thermal refers to the fact that they were not created thermally in the early universe, but rather through a phase transition: at high temperatures, before the $U(1)_{PQ}$ symmetry breaking, the axion was massless; once the temperature of the universe went lower than the QCD energy scale, the axion effective potential tilted, and the axion acquired a mass due to instanton effects. If at this point the axion field was not in a minimum of its potential, it would begin to oscillate and, without a damping mechanism for these oscillations, this energy remains until today as physical axion quanta. The contribution of this mechanism to axion relic density has been found to be

$$\Omega_A h^2 = \kappa_A \left(\frac{f_A}{10^{12}\text{GeV}} \right)^{1.175} \theta_i^2, \tag{2.28}$$

where κ_A is a numerical factor of the order of the unity, and θ_i is a parameter, called the misalignment angle, that relates to the value of the axion effective potential at the moment of the *PQ* phase transition.

Finally, the WIMPs constitute the largest group of candidates; these are elementary particles χ, with very large masses —from 10 GeV to a few TeV—, and with cross sections of the order of the weak interaction; being originally in thermal equilibrium with the rest of particles produced after the inflation, the WIMPs density started to drop out exponentially once the temperature $T < m_\chi$. Effectively, WIMP pairs where annihilating into SM particles, but the reverse process could not longer happen, for $T < m_\chi$ implies there was not enough energy for the SM particles to annihilate into a χ pair. From Boltzmann relation

$$\rho_\chi \propto e^{-m_\chi/k_B T}. \tag{2.29}$$

Eventually, the density of WIMPs was small enough for these annihilations to stop being efficient. This is known as *freeze out*. At a first approximation, freeze out happens at a temperature $T_F \simeq m_\chi/20$ for any WIMP model [25]. From this moment, the WIMP density remains practically constant, and it is approximately given by [25]

$$\Omega_\chi h^2 \simeq 0.1 \frac{\mathrm{pb} \cdot c}{\langle \sigma_{(\chi,\mathrm{SM})} v \rangle} \tag{2.30}$$

where c is the speed of light, v is the relative velocity of two WIMPs in their Center of Mass system, and $\sigma_{(\chi,\mathrm{SM})}$ is the total annihilation cross section of a pair of WIMPs into SM particles; the product $\sigma_{(\chi,\mathrm{SM})} v$ is thermally averaged.

Currently, a wide variety of experiments is trying to detect a WIMP signal through two main mechanisms: the first one is to measure an excess of SM model particles, which cannot be accounted by the current known cosmological sources, and associate it with the products of $\chi - \chi$ annihilations; currently, AMS-02 has taken precise measurements of the electron and positron fluxes in primary cosmic rays, as well as protons and Helium fluxes [27–29] which can be used to impose constraints on dark matter properties (see, for example, [30]). The second mechanism involves the direct detection of WIMPs through their interaction with different kind of detectors; DAMIC [31] with Silicon CCD, CoGeNT [32] with Germanium, DAMA/LIBRA [33] with NaI scintillators and XMASS [34] with liquid Xenon, are just but a few of the experiments that opted for this path. Most of these experiments use materials with high Z, which are sensitive mainly to WIMPs with masses of the order of 100 GeV; direct production at CERN also aims for a similar mass scale. The less studied region of $m_\chi < 10$ GeV has received a great deal of attention recently, by using matured detectors with low energy thresholds. In the current experiment a Silicon on Insulator Pixel Detector is used to explore this low mass region. The detection process and analysis framework for this experiment is explained in the next section.

2.2.3 Constrains on the WIMPs Physical Properties

Figure 2.5 resumes the dark matter detection process in a SoI pixel detector.

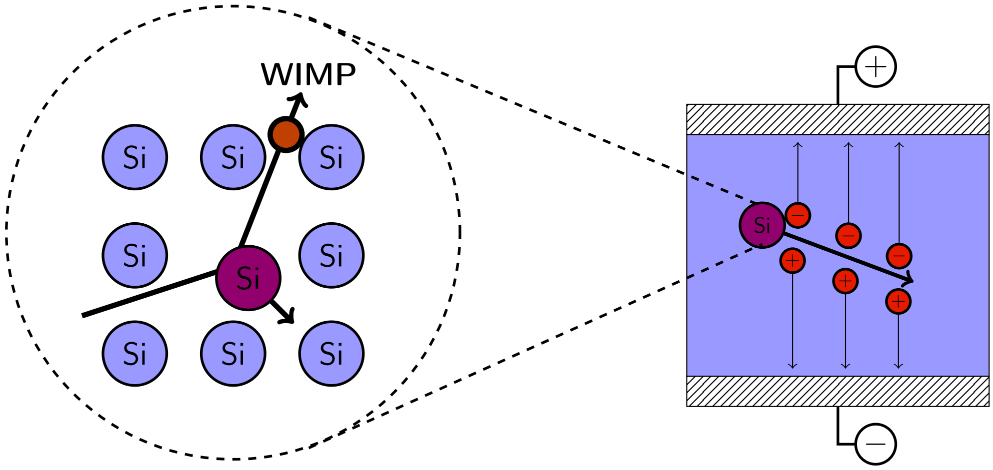

Fig. 2.5 Detection process for WIMPs in a SoI pixel detector; the elastic nuclear recoil of the WIMP with the Si nuclei produces electron-hole pair shower inside the bulk material of the pixel. The displacement of the Si nucleus has been exaggerated here for othegr purposes. Since galactic velocities are of the order of $10^{-3}c$, values of the WIMP mass in the 10-1000 GeV range would lead to typical recoil energies in the range 1-100 keV.

Experiments aiming to detect, or set limits on, nuclear recoils arising from collisions between the heavy particles and the target nuclei, have a common theoretical basis. The differential energy spectrum of these recoils obeys, according to [35], the following differential equation:

$$\frac{dR}{dE_R} = \frac{R_0}{E_0 r} e^{-E_R/E_0 r} \tag{2.31}$$

where R is the event rate per unit of mass, R_0 is the total event rate, E_R is the recoil energy, E_0 is the most probable incoming kinetic energy for a dark matter particle χ of mass m_χ, and r is the kinematical factor, which, for a nucleus of mass M is

$$\frac{4Mm_\chi}{(M+m_\chi)^2}.$$

All experimental efforts aim to measure the differential rate —this is, the left side of equation (2.31). However, the right side of this equation is considerably more complex than it suggests; on its formulation, the assumptions made are not adequate to yield trustworthy results. In particular, the equation assumes a static detector, it does not take into account the spin dependence of the nuclear interactions, and it ignores the effects of a finite size of the nucleus. A more correct form of the differential rate is given by equation (2.32)

$$\frac{dR}{dE_R} = S(E)F^2(E)I \tag{2.32}$$

where $S(E_R)$ is the modified spectral function, taking into account the physical properties of the detection setup, $F(E_R)$ is a form factor which correction term for the size of the target nuclei and I is a function involving the spin dependence of the χ-nucleon interaction. Lewin and Smith [35] propose multiple solutions for the form of these terms. Here, only those relevant for the current study are mentioned. The reader can refer to the original publication for the other cases. Ignoring any dependency on the detector efficiency, the modified spectral function $S(E_R)$ would be

$$S(E_R) = \frac{k_0}{k_1}\left[\beta(E_R) - \frac{R_0}{E_0 r} e^{v_{\mathrm{esc}}^2/v_0^2}\right] \tag{2.33}$$

with

$$\beta(E_R) = \frac{R_0}{E_0 r}\frac{\pi^{1/4}}{4}\frac{v_0}{v_E}\left[\mathrm{erf}\left(\frac{v_{\min}+v_E}{v_0}\right) - \mathrm{erf}\left(\frac{v_{\min}-v_E}{v_0}\right)\right]. \tag{2.34}$$

In the former equations, v_{esc} is the escape velocity of the Milky Way galaxy, v_E the Earth's speed, v_0 a parameter obtained from the dark matter velocity distribution

$$f(\mathbf{v},\mathbf{v}_E) = e^{-(\mathbf{v}+\mathbf{v}_E)^2/v_0^2},$$

the ratio

$$\frac{k_0}{k_1} = \left[\mathrm{erf}\left(\frac{v_{\mathrm{esc}}}{v_0}\right) - \frac{2}{\pi^{1/2}}\frac{v_{\mathrm{esc}}}{v_0} e^{v_{\mathrm{esc}}^2/v_0^2}\right]^{-1}$$

and $v_{\min}$ the variable that encloses the E_R dependence:

$$v_{\min} = \left(\frac{E_R}{E_0 r}\right)^{1/2} v_0.$$

For a spin-independent form factor, we get

$$F(qr_n) = 3\frac{j_1(qr_n)}{qr_n} e^{-(qs)^2/2} \tag{2.35}$$

where $j_1(x)$ is the first Bessel function, $q = (2ME_R)^{1/2}$ the momentum transfer, s is a measure of the nuclear skin thickness, r_n an effective nuclear radius:

$$r_n^2 = c^2 + \frac{7}{3}\pi^2 a^2 - 5s^2 \text{ with } c \simeq 1.23A^{1/3} - 0.6\,\mathrm{fm},\ a \simeq 0.52\,\mathrm{fm}$$

and A the atomic mass of the target nuclei in amu.

The limit on R_0/r obtained from the recoil differential rate is exactly equivalent to the ratio σ_0/μ^2 [35], with σ_0 the cross section at zero momentum transfer, and μ the reduced mass of the system

$$\mu = \frac{Mm_\chi}{M+m_\chi}.$$

This translates into a dependency relation among σ_0 and m_χ for different values of dR/dE_R. The result of this analysis for different experiments, normalized to a single nucleon, is shown in figure 2.6.

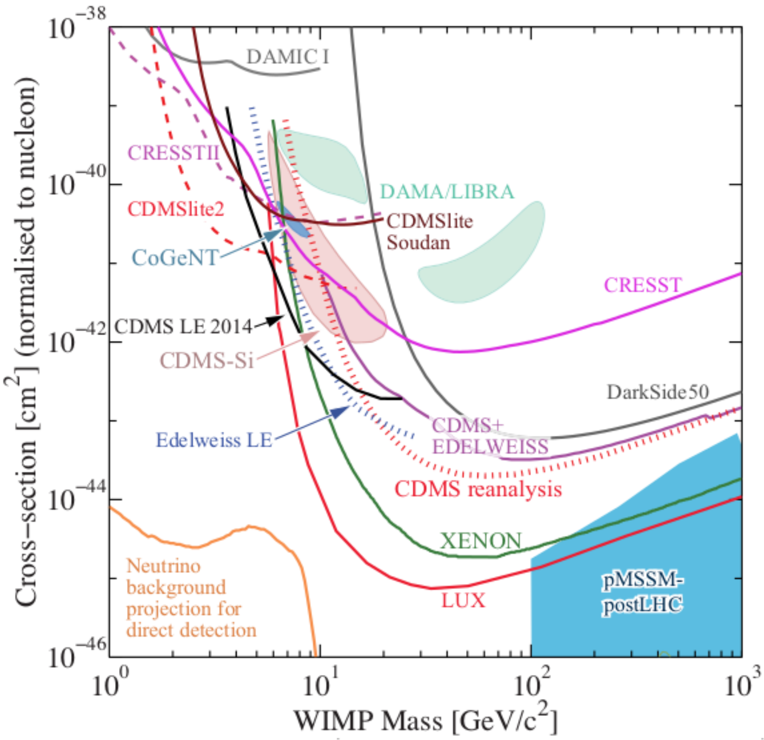

Fig. 2.6 WIMP cross sections for spin-independent coupling versus mass. The blue region corresponds to the region of interest for the pMSSM, a version of the Minimal Super Symetric Model with 19 free parameters, done by the ATLAS colaboration. Image obtained from [25].

For common values of the parameters in equation 2.32 one obtains an expected event rate that ranges from about one event to less than 10^{-3} events per kilogram of detector material per year [36]. Hence, direct WIMP searches require extremely low background levels. A long term objective of this experiment is to obtain a high purity, which would translate into a lower upper limit —sensitivity— for the WIMP mass than previous experiments. The most recent result from XENON1T sets the current benchmark for dark matter detectors' background at $(1.93 \pm 0.25) \times 10^{-4}$ events/(kg $\times$ day $\times$ keV$_{ee}$), and the most stringent exclusion limits for the spin-independent WIMP-nucleon cross section, with a minimum of 7.7×10^{-47} cm^2 for a 35 GeV WIMP at 90% confidence level [37].

Chapter 3

The Experimental Setup

Have already portrayed the main physics objectives that motivate this experiment, the attention is now driven to the experimental setup. Section 3.1 will deal with the physical properties of the silicon on insulator pixel detector known as XRPIX. Section 3.2 will describe the experimental setup proposed.

3.1 The XRPIX SOI Detector

Developed in a joint effort between the University of Kyoto and High Enery Accelerator Research Organization (KEK) in Japan, the XRPIX (X-Ray PIX) detector was originally conceived as Silicon on Insulator Pixel Detector (SOIPIX) for future X-ray astronomical satellites [38]. Being in the need for a faster detector with better time resolution and a wider energy range, for observational studies that require the distinction between X-rays from cosmic events and charged particles tracks. The main components of the pixel detector are shown in figure 3.1.

The XRPIX is a monolithic pixel detector, which includes a thin CMOS layer of around 8 μm, a buried oxide layer of around 0.2μm, and a n-type, thick Si-sensor layer, stacked vertically on a single chip [38, 39]. The presence of a CMOS in each pixel,and the absence of bumping bonds, allows for a faster readout time and higher energy resolution.

The detector can be used in two diferent forms. The first, called the *frame mode*, consists of the next three steps [39]:

1. The photo-diodes of all pixels are reset to a constant voltage.

2. The photo-diodes await for the incoming radiation, in a constant integration time (effective exposure) that can be determined by the user; common used times are between 0.01 and 0.1 milliseconds.

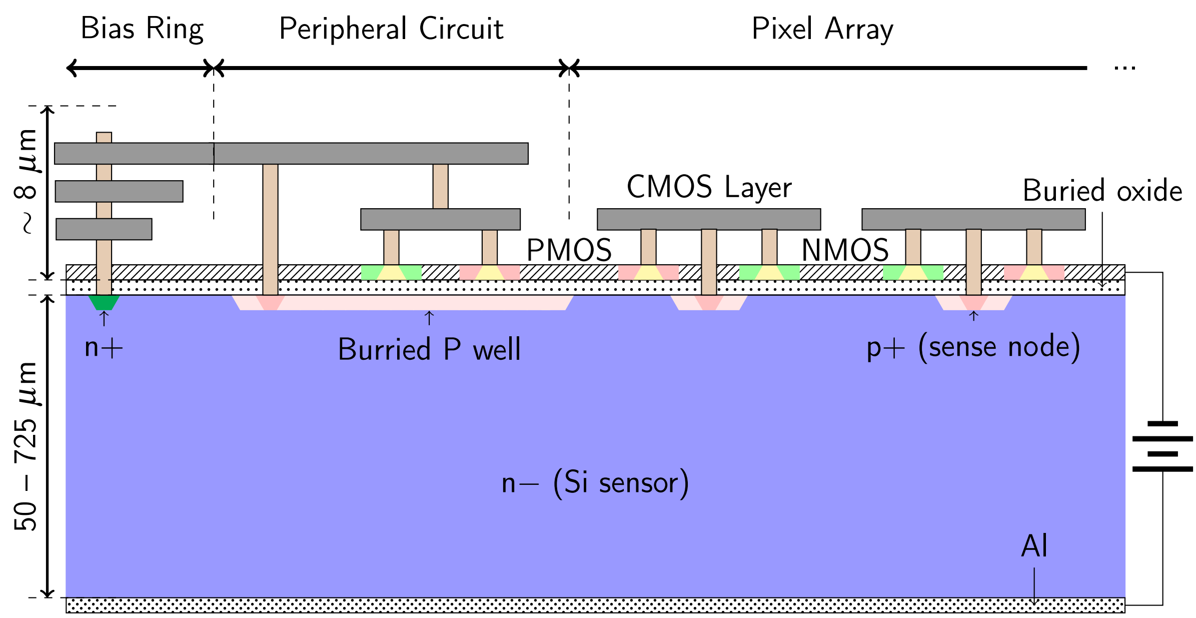

Fig. 3.1 Layout of the XRPIX detector; the pixel array size, the depletion region size, and the size of a single pixel depend on the model being used. Specifications for the XRPIX2b and XRPIX5 chips, which are the ones used in the elaboration of this work, are shown in table 3.1. The main components are: the bias ring, the peripheral circuit, and the pixel array. Radiation would penetrate in the n-doped Si region, producing an electron-hole shower; the device is back biased, and reaches full depletion at around 150 V. The holes are collected in the sense node. To avoid any back gate effect, the central p+ diode is surrounded with a light p-type region called the burried P well. The Buried Oxide (SiO_2) layer thickness is 0.2 μm. The aluminium layer is also 200 nm thick.

3. Analog voltage outputs of all the pixels are read, and converted to digital signals.

So, even when there are not significant signals present, there will still be an output, with the readout of each pixel. The second form, called the *event mode*, is based on a single-pixel readout mode [39]:

1. The photo-diodes of all pixels are reset to a constant voltage.
2. The photo-diodes await for the incoming radiation; once there is a hit in one of the pixels, it is accessed directly.
3. The analog voltage of the pixel is transformed into a digital signal, and transferred to the DAQ-PC.
4. If there is no signal, the system is reset periodically.

In newer versions of the XRPIX, the event mode scans not only the pixel with the highest signal (central pixel), but also the values of the pixels surrounding it. A usual pattern is a 3×3 grid, with the central pixel in the center. Later versions of the detector allow for the user to determine the size of this grid up to an 8×8 square.

In table 3.1 the characteristics of the XRPIX2b and XRPIX5 chips are listed. A picture of both is also shown in figure 3.2.

Physical Properties		
	XRPIX2b	XRPIX5
Total size (mm^2)	6×6	24.6×15.3
Effective size (mm^2)	4.6×4.6	21.9×13.8
Pixel size (μm^2)	30×30	36×36
Readout channels	144×144	608×384
Sensor layer thickness (μm)	500	500
Readout noise	70 e^-	48 e^-
FWHM at 13.95 keV (Am-241)	1.28 keV	580 eV

Table 3.1 Properties of the two XRPIX chips used for the development of this work. The XRPIX5 is considerably larger than the XRPIX2b, resulting in a higher luminosity. Full depletion is reached around 200 Volts for both components.

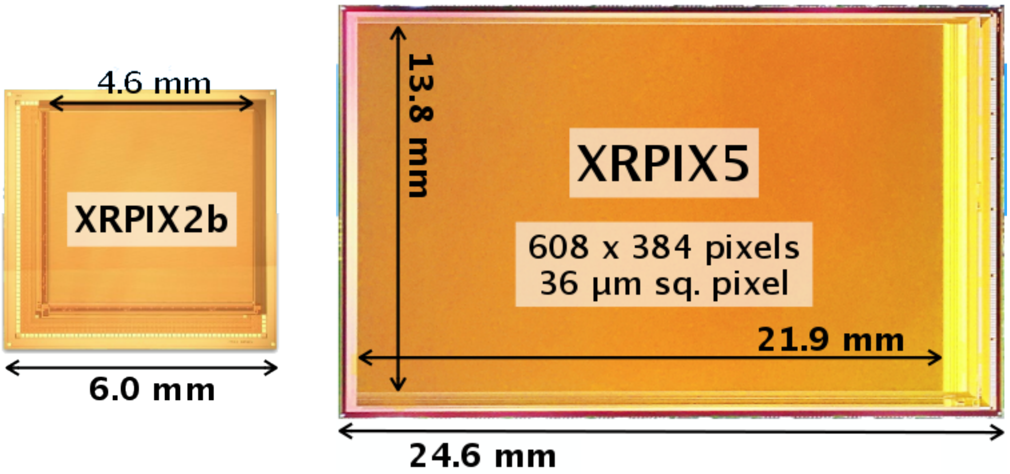

Fig. 3.2 Photographs of the XRPIX2b (left) and the XRPIX5 (right).

A first analysis was done using Americium 241 in order to estimate the energy resolution around the region of interest. The measurements performed are shown in figure 3.3. A FWHM of 1.28 keV around 13.95 keV, which is 9.2% of the maximum value, was obtained. The latest report from the XRPIX group informs of a width of 400 eV at 13.95 keV, using the XRPIX3-CZ model. Though this represents an astonishing improvement in comparison with the most recent experiment using the same detection technique executed by Derbin et. al. [19] —the percentage is 10.2 at 14.4 keV— and former results with the XRPIX1 (1.5 keV at 13.9 keV [39]), an improvement in the energy resolution can be obtained. The experimental setup described in the next section, as well as the background studies developed in the following chapters, aim precisely to achieve this.

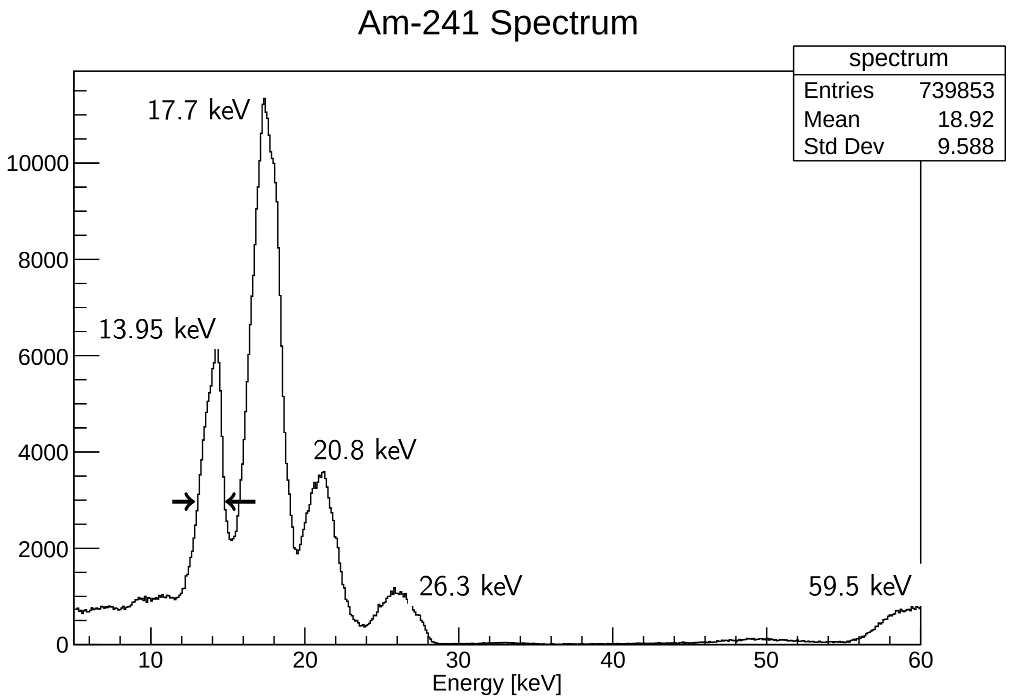

Fig. 3.3 γ-energy spectrum for ^{241}Am obtained with the XRPIX2b chip at -80°C and with a bias voltage of 200 V in the frame mode. The arrows show the half maximum point for the 13.95 keV peak. The width is of 1.28 keV, which corresponds to a 9.2% of the peak value.

3.2 The Experimental Setup

A schematics of the planned experimental setup is shown in figure 3.4. It is located in a laboratory in the sixth floor of the Graduate School of Science of the University of Tokyo, Japan.

The lead blocks were obtained from a former experiment in the University of Tokyo, and there are two sizes available: a $5 \times 10 \times 10$ cm^3 box, and a $5 \times 10 \times 20$ cm^3 one. The fact that the size and the shape of these blocks cannot be changed represents an obstacle for the hermiticity of the experiment, since the space needed for the cables to pass effectively opens a gap between the blocks. This was temporary solved by making the connections to run parallel to the edges of the blocks.

The copper in the inner layer is a highly pure one [40]. Known as oxygen-free copper, the presence of oxygen is less than 0.001%, and copper accounts for at least 99.95% of the material.

The polyethylene layer from the thermostatic chamber is enough to stop practically all of the incoming α particles. Most β and γ rays are expected to be blocked by the lead shield. Copper is used to reduce the amount of events generated by secondary photons or electrons produced during the attenuation of primary radiation, and to stop the particles emitted by radioactive components in the lead shield.

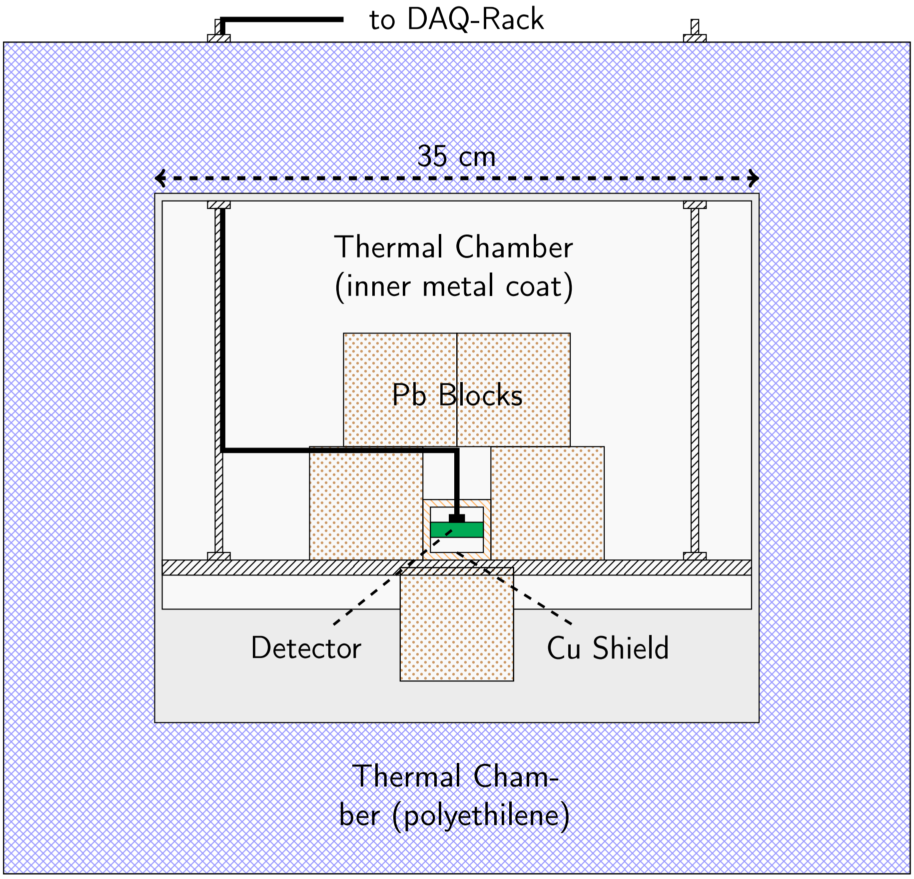

Fig. 3.4 Simple schematics of the pilot experiment; the blue layer corresponds to a thermal chamber, which usually runs at -80°C. It has 4 holes in the upper face, which allow to connect the detector with the DAQ-PC and the power sources (here we only draw two); the whole setup is located inside a clean booth, and a clean air unit is also in use. The inner space corresponds to a $35 \times 35 \times 35$ cm^3 box. The second layer corresponds to pilled up lead blocks; there are lead blocks in the front and rear ends too. The final layer corresponds to a copper plate covering most of the detector; there are some gaps to connect the peripherals. The determination of the adequate thickness of these two layers is part of the present work.

This scheme suggests that the main expected sources of external background are γ rays from environmental radioactivity, and cosmic rays' related particles. Though the later can be effectively reduced by the use of an active shield such as a VETO counter, showers produced in the shielding material still require a deeper consideration; radioactivity also requires a more detailed analysis, for there are naturally occurring radioisotopes whose decay chain elements happen to have spectral lines in the energy range of interest (0 to 20 keV). Moreover, even if some of these particles have energies way over the keV range, the energy deposited in the detector may still be around a few tenths of keV. A complete discussion on this topic can be found in the next chapter. A picture of the experimental setup is depicted in figure 3.5.

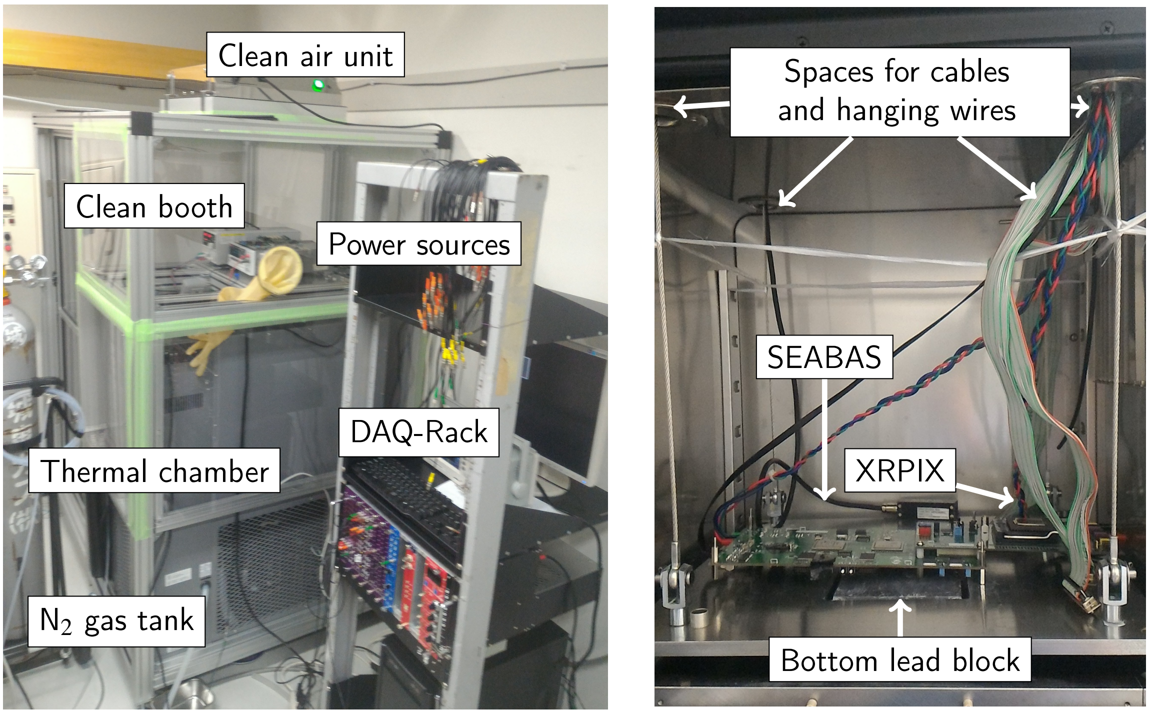

Fig. 3.5 Photographs of the experimental setup (left) and the interior of the thermal chamber (right). The power sources correspond to two voltages sources situated above the thermal chamber. The XRPIX used is the XRPIX2b model, and the lead and copper shields have been removed, except for the bottom shield, embedded in the chamber. N_2 gas is used to reduce the humidity in the inner cavity, which seems to affect the lead blocks (there was a white coating on them, as can be appreciated in the bottom lead block).

The sizes of the subboard and the SEABAS conversion board also represent a challenge for proper hermiticity. A picture of both is shown in figure 3.6. The subboard contains the XRPIX chip. The SEABAS (Soi EvAluation BoArd with Sitcp, [38]) universal main board contains two FPGAs, used for chip control and data taking, and for data transmission, and is responsible for the data conversion and control tasks. In order to reduce the space used inside the chamber, a pair of conversion boards is used, so only the subboard and the conversion board are located inside the thermal chamber. The SEABAS and the extra conversion board would then be located outside, and D-sub cables would be used to connect both of the conversion boards through the holes in the roof of the thermal chamber.

From the background results exposed in the next chapter it became evident that a WIMPs search is not feasible yet, so the first experimental setup has been oriented towards the search of solar axions. The detector designed for this is shown in figure 3.7. A stack of XRPIX5 chips is used in order to increase the quantum efficiency of the experiment. Between each pair of chips there will be a ^{57}Fe foil (see bottom picture in figure 3.7), so the photon emitted after the absorption of the axion can be detected by any of the two devices.

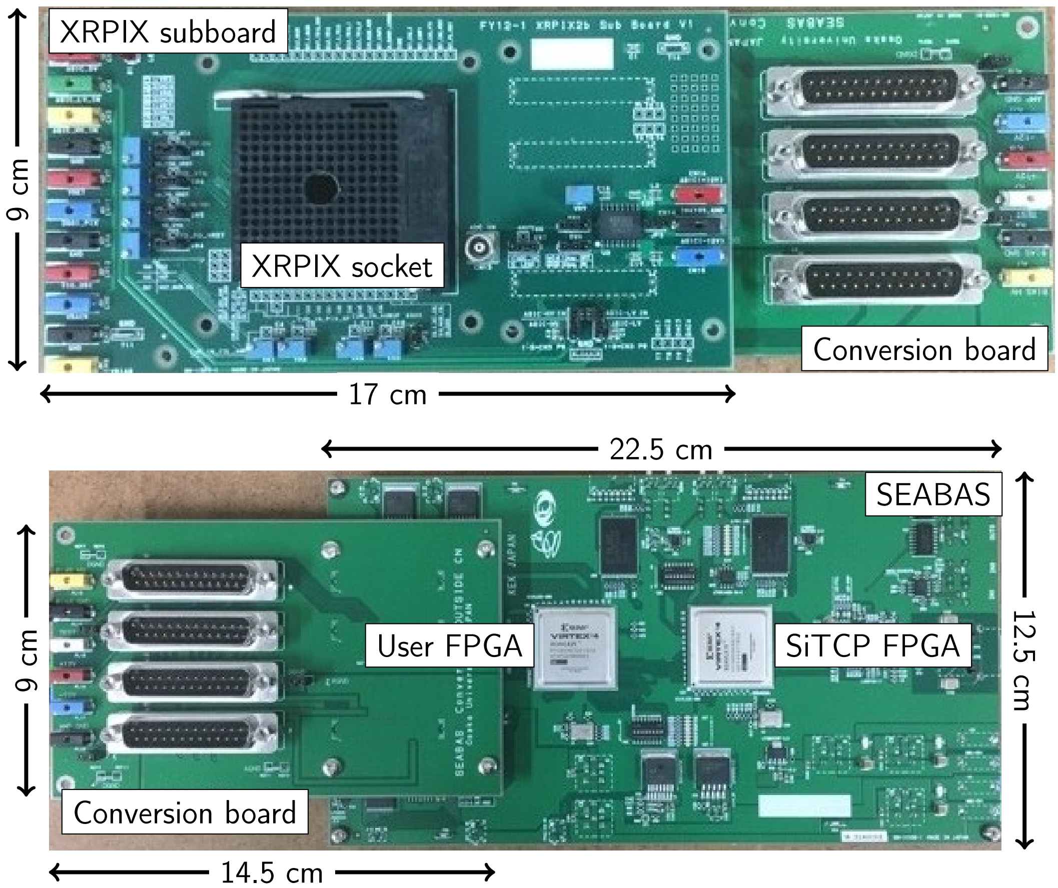

Fig. 3.6 Photographs of the XRPIX2b subboard and a conversion board (up), and the SEABAS main board with a conversion board (down). The four sockets are used to connect the two conversion boards using D-sub cables. The User FPGA is responsible for data taking and chip control, whereas the SiTCP FPGA is used for data transmision.

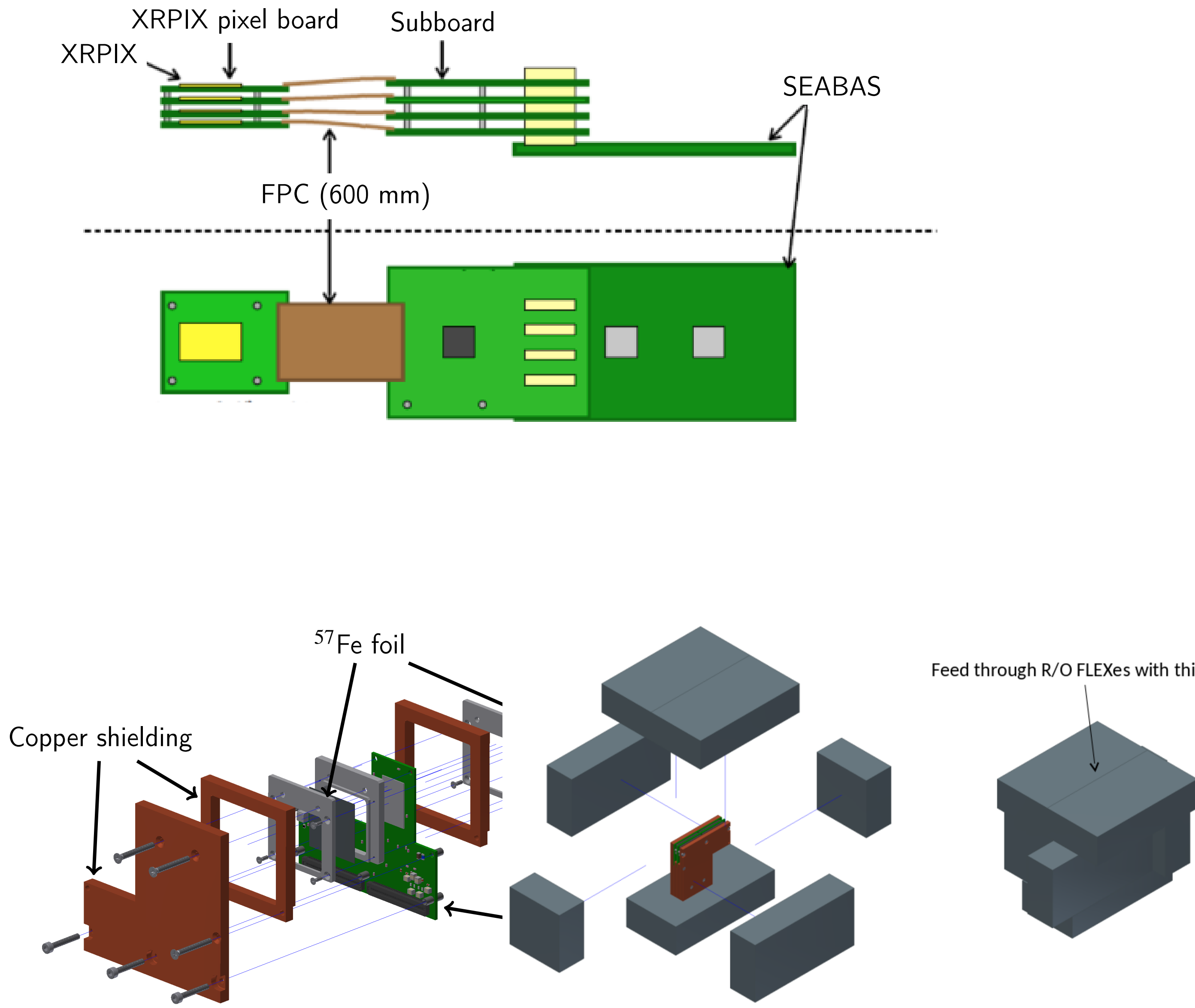

Fig. 3.7 Top: side and top views of the XRPIX based detector prototipe for solar axion search. *Bottom:* schematics of the XRPIX pixel board; in dark gray are the ^{57}Fe foils; in light gray, the holders designed for these foils, made of PEEK (Polyether Ether Ketone). In brown is the copper shielding, and green represents the XRPIX pixel boards. This image displays two boards stacked; for this geometry, the size is $98{\times}90{\times}25$ mm^3.

Chapter 4

A Preliminary Background Study

Up to this point the main objectives and the experiment designed to accomplish them have been explained. As a primary step in the elaboration process, a study of the background sources is at place. The main objectives are to *identify the main external background sources*, to *estimate their relative contribution to the total background spectrum*, and to *stablish a first limit on the background rate for this experiment at 14.4 keV*; however, direct measurements with the XRPIX were not available at the moment of this study, so the next steps were taken: in the first section of this chapter, a brief review of the most important external background sources for WIMP and solar axions searches is given. The second section shows the first background measurements performed with a CdTe detector. Finally, the third section explores the shielding properties of lead and copper against the main sources mentioned in section 4.1; the detection efficiency of the XRPIX and the CdTe are evaluated, and from the results of section 4.2 an estimation of the events rate for the XRPIX is obtained.

4.1 Main Sources of External Background

In a detection experiment, the background is usually any kind of signal produced by a radiated particle different from the searched one. The nature of this unwanted radiation depends on the properties of the detector and, in a broader sense, on the experimental design. Given the fact that there no measurements can be performed on the XRPIX components, the current analysis focuses in the background sources coming from outside the detector. In most detection experiments, including this one, the primary external background sources are environmental radioactivity and cosmic rays muons.

4.1.1 Radioactivity

Radioactivity refers to the emission of particles from nuclei as a result of nuclear instability; these unstable nuclei are present at different proportions in most of the materials used in daily life. The most naturally abundant radioactive isotopes are ^{232}Th, ^{238}U, ^{40}K, deposited in the shielding elements and in the detector materials, found in the soil and in the walls of the experimental room, and ^{222}Rn gas, which is a decay product of the long-lived ^{238}U and ^{232}Th, and is a persistent source of radiation even for properly sealed experiments, since it can be produced by surface emanations from impurities in the internal detector components; the constant air circulation provided by the clean air in the experimental design (chapter 2) aims to reduce the amount of ^{222}Rn generated by these impurities in the cavity. The emission spectra for the four radioactive sources mentioned are shown in figure 4.1.

Being the experiment located in a sixth floor, the contribution of the soil radioactivity can be in principle ignored[1]. As an ilustrative scheme, a study done by Suzuki et. al. [42], reported the mean activities of different radioelements present in Japanese concrete. Their results are summarized in table 4.1.

Radionuclide	**Mean Activity (Bq kg^{-1})**
^{40}K	505.2
^{238}U	32.3
^{232}Th	25.6
^{228}Th	23.2
^{226}Ra	22.1

Table 4.1 Mean activity of the the most common radionuclides in Japanese concrete; the concrete mixture is composed by 12% cement, 10% water, 10% admixture, 26% fine aggregate, and 42% aggregate.

Radiation can be classified acording to the kind of particle emitted. Alpha particles correspond to positively charged Helium nuclei and, as charged particles, they obbey the Bethe-Bloch equation [43]:

$$\frac{dE}{d(\rho x)} = 0.307\frac{Z}{A_r}\frac{Z_i^2}{\beta^2}\left[\frac{1}{2}\ln\left(\frac{2m_ec^2\beta^2\gamma^2T_{\max}}{I^2}\right)-\beta^2-\frac{\delta(\beta)}{2}\right]\frac{\text{MeV cm}^2}{\text{g}} \tag{4.1}$$

where $dE/d(\rho x)$ is the energy loss of the particle per unit length —normalized to the density ρ of the detector material— due to its interactions with electrons in the detector material, Z_i is the charge of the incident particle, c is the speed of light, β is the speed of the particle in

[1] Effectively, [41] proposes a shieldinng factor of 0.01 for structures with more than four stories. This is, a reduction of 90% of the original radiation from soil. It also gives the next values for the average concentration of radionuclides: 370 Bq/kg (^{40}K), 25 Bq/kg (^{238}U or ^{226}Ra) and 25 Bq/kg (^{232}Th).

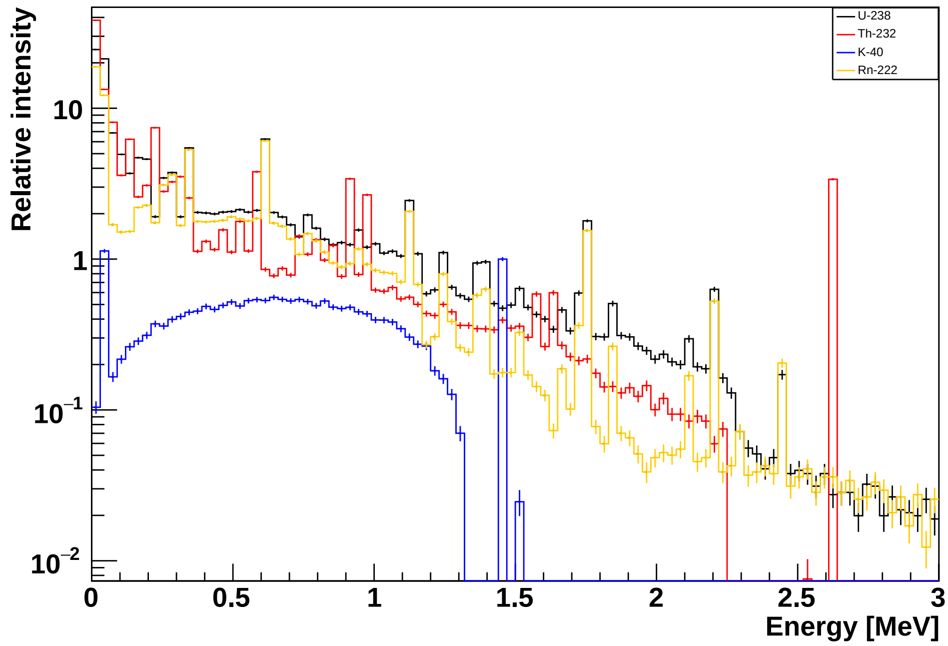

Fig. 4.1 MC simulated spectra for Uranium-238, Thorium-232, Potassium-40 and Radon-222 using the radioactive package of Geant4. All four intensities are normalized to the intensity of the 1.46 MeV gamma transition for Argon-40 in the ^{40}K decay chain after 10^4 decays (all other spectra were generated by simulating 10^4 decays as well). These spectra include the next kind of particles: electrons, neutrinos, photons and alpha particles.

units of c, γ is the relativistic factor

$$\gamma = \frac{1}{\sqrt{1-\beta^2}},$$

Z is the atomic number of the detector nuclei, A_r is the relative atomic weight of the nuclei, I is the mean excitation energy of the material, $T_{\max}$ is the maximum energy transfer to one electron, and δ is a density dependent term.

The range of alpha particles from nuclear decays (this is, with energies up to 10 MeV) never exceeds 40 μm in Pb, so the thinnest lead shield available for this experiment (5 cm) is enough to stop all α radiation. A Monte Carlo generated alpha spectrum for the ^{238}U and ^{232}Th sources is given in figure 4.5 (the spectrum of ^{222}Rn, being it a decay product of the former two, is included in this figure too. ^{40}K does not undergo α decays).

The second kind of radiation which was taken into account in this study were β rays. In contrast with α particles, high energy electrons undergo multiple scattering before losing all their energy. As a result, high energy electrons travel a greater distance in all materials. For the four radionuclides considered here, β rays have energies up to 3 MeV. For an electron at

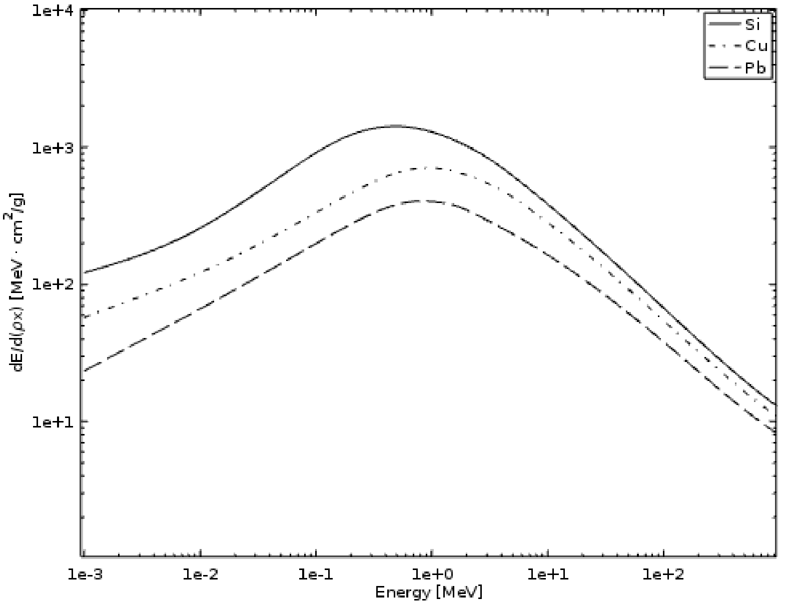

Fig. 4.2 Stopping power for alpha particles up to 1 GeV in Silicon, Lead and Copper. $T_{\max} = 2m_ec^2\beta^2\gamma^2$, with m_e the mass of the electron. The plot was generated with data from [44].

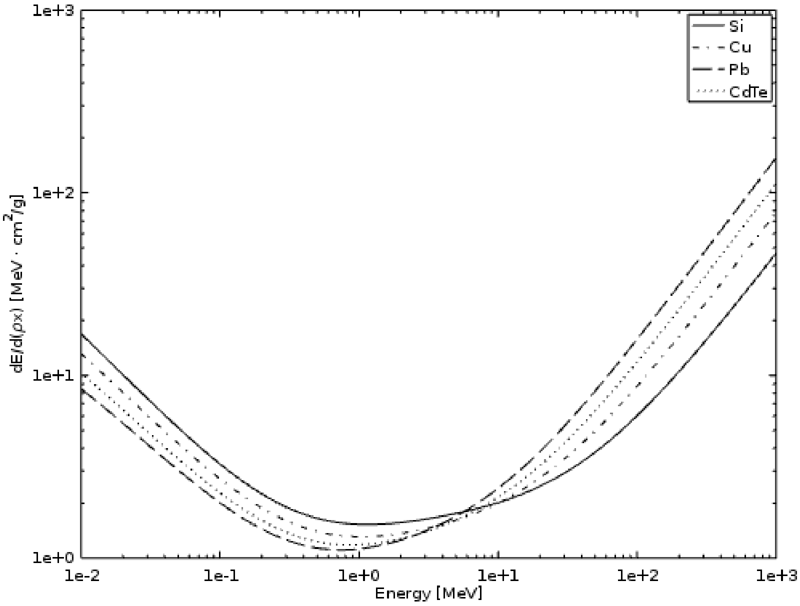

Fig. 4.3 Stopping power for beta particles up to 1 GeV in silicon, lead, copper and cadmium telluride. Here, $T_{\max} = \gamma m_ec^2$ was used, with m_e the mass of the electron. The plot was generated with data from [44].

this energy, the penetration depth in lead is around 2 mm. Again, the minimum thickness (5 cm) seems enough to stop all β radiation.

The stopping power for electrons in Si, Cu, Pb and CdTe is shown in figure 4.3. The discrepancy with the shape of the plot in figure 4.2 comes from the different expression used for $T_{\max}$. It is possible for these electrons to leave the detector volume before depositing all of their energy; this would increase the background rate due to energy depositions within the range of interest. The beta rays spectra for Uranium-238, Thorium-232, Potassium-40 and Radon-222 are shown in figure 4.5.

Electrons deposit energy through collisions and radiative processes. The later are relevant for energies above 0.2 MeV in lead; this implies that β rays with energies above this value are likely to produce photons through *bremsstrahung* radiation. An electron of energy E has an *average* energy loss due to bremsstrahlung equal to [43]

$$\frac{dE}{dx} = -\frac{E}{X_0} \tag{4.2}$$

where X_0 is the radiation length, given approximately by [43]

$$\frac{1}{X_0} \approx 4\alpha r_0^2 \frac{\rho N_A}{A_r} Z(1+Z) \ln\left(\frac{183}{\sqrt[3]{Z}}\right)$$

with α the fine structure constant, N_A the Avogradro's number and r_0 the classical electron radius. A more exact expression for X_0 can be found in [45]. The emitted photons have a $1/E$ energy spectrum, and photons with energies up to E do occur; the power spectrum for these photons is then a constant extending up to the energy of the radiating particle. This in turn implies that even if no electrons can make it through the lead shield, it is still necessary to consider the effects produced by bremsstrahlung photons.

At this stage, it is important to take into account the radioactivity of the shields, the main source being the lead blocks (as mentioned in chapter 2, the copper used for shielding is a highly pure –99.99% purity— one). Assuming lead radioactivity comes from ^{238}U contamination, the radioactivity from lead would have a continuous β spectra with energies up to 3 MeV. Electrons with energies close to 1 MeV have a penetration depth of 0.7 mm in copper. Other energies have larger stopping power, and shorter penetration depth (see figure 4.3). This implies that a copper shield of minimum thickness (6 mm) will stop all β radiation from lead. Moreover, in copper, bremsstrahlung is only relevant for electron energies above 2.5 MeV: at 1 MeV it accounts for only 3.5% of the energy lost by the electron [44] and the percentage becomes lower for lower energies. So, at this stage, the only concern related to lead radioactivity is its γ spectrum.

This leads us to the main external background source for this experiment: γ rays. This source can be further divided in: photons produced by bremsstrahlung in the shielding material (from cosmic and beta rays) and gamma rays originated from radioactive decays. For particles of mass M, bremmstrahlung is suppressed by a factor of $(m_e/M)^2$. For muons this factor is close to 0.25×10^{-4}. However, the electrons in the material can be ionized by the cosmic particles, and their energies do fall in the range were radiative losses are dominant. These electrons can, and effectively do emit bremsstrahlung radiation. There is, then, a electromagnetic component in the radiation produced by cosmic muons.

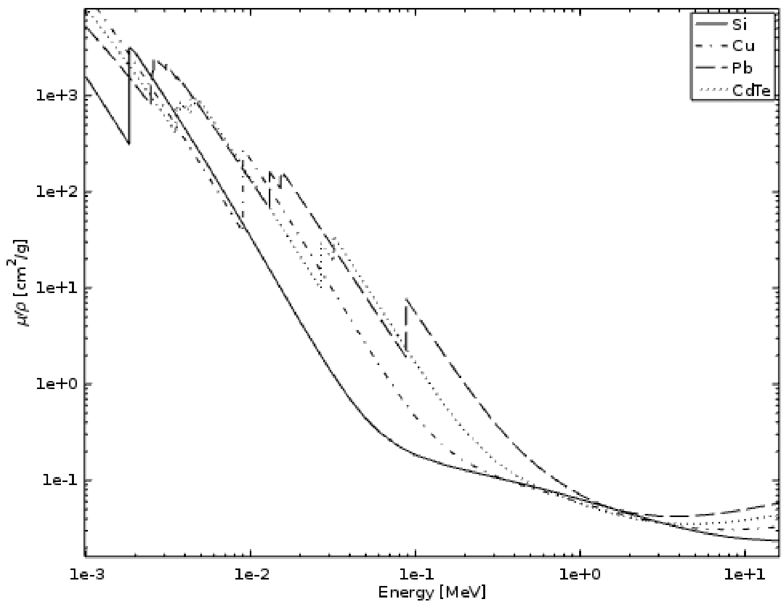

Fig. 4.4 Mass attenuation coefficient —normalized to the density of the material— for photon energies up to 10 MeV in silicon, copper, lead and cadmium telluride. The attenuation includes the contributions of the three processes mentioned: photoelectric effect, Compton scattering and pair production. The plot was generated with data from [46].

Gamma rays interact with matter through three main mechanisms: for energies less than 100 keV, the photoelectric effect is the dominant interaction. Here, the photon undergoes an interaction with one atom and completely disappears. In exchange, the energy of the photon is used to excite one of the electrons in the atom; this electron can then be raised to a higher level within the atom, or become a free electron. The excitation of this electron produces a vacancy in one of the energy levels of the atom, which is quickly filled; this process is usually accompanied by the emission of one or more X-rays.

For values of the energy between a few hundreds of keV to 1 MeV, the leading process is the Compton scattering, which is the elastic collision between a photon and a electron. If the gamma ray energy is small, the atom as a whole takes up the energy and the momentum transferred to the electron, and the interaction is called coherent Compton scattering or Rayleigh scattering; if, on the contrary, the electron leaves the atom, the interaction is called incoherent Compton scattering.

Finally, if the energy of the photon is at least twice the mass of an electron, the energy of the photon can be used to produce and electron and positron pair. This process dominates for gamma energies above 1 MeV.

Adding up, if a beam of photons with initial intensity I_0 enters matter, its intensity $I(x)$ after it has traveled a distance x in the medium obeys

$$\frac{I(x)}{dx} = -I(x)N\sigma$$

where N is the density of scattering centers, and σ is the cross section between the photons and these scattering centers. The product $N\sigma$ is known as the linear attenuation coefficient μ. The intensity of the beam is then

$$I(x) = I_0 e^{-\mu x}. \tag{4.3}$$

The mass attenuation coefficients for Si, Pb, Cu and CdTe are shown in figure 4.4. The gamma spectra for the radioactive elements mentioned before is also shown in figure 4.5.

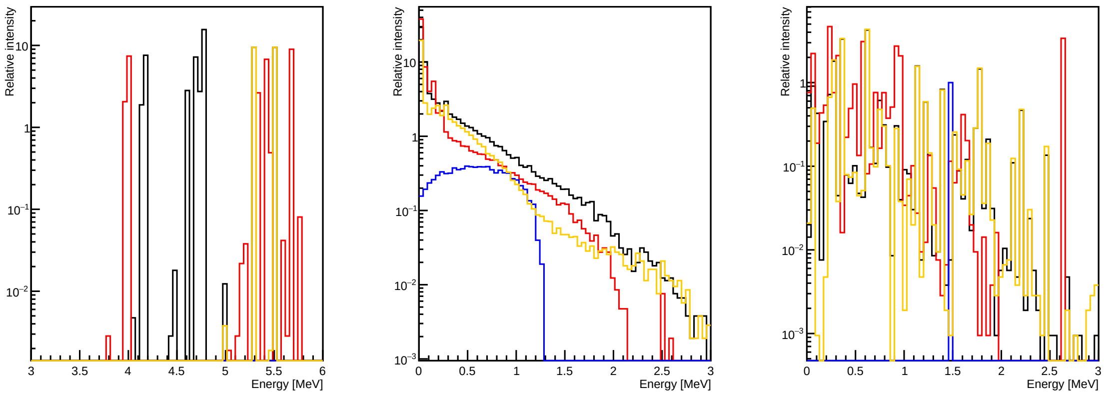

Fig. 4.5 MC simulated spectra for α (left), β (center) and γ (right) rays in ^{238}U (black), ^{232}Th (red), ^{40}K (blue) and ^{222} Rn decay chains, using the radioactive package of Geant4. All intenisties are normalized to the intensity of the 1.46 MeV gamma transition for Argon-40 in the ^{40}K decay chain after 10^4 decays. There are no α decays for potassium, and only the γ rays produced in the uranium, thorium and radon decay chains have energies in the range of interest (0 - 20 keV) [47]. Notice that the γ spectrum for ^{222}Rn is very similar to those of ^{238}U and ^{232}Th, which indeed indicates radon is a decay product of these two.

4.1.2 Cosmic Muons

Cosmic rays muons are also of interest in the current scheme. Not only, as previously stated, because of their ionization potential, but also because of the neutrons they produce through spallation and μ-absorption in the shielding material. Indeed, neutrons, being neutral, massive particles, produce the most similar signal to that expected from WIMPs. Spontaneous fission in Uranium-238 is an important component of low energy neutrons production as well.

Around 80% of all primary nucleons —this is, nucleons accelerated at astrophysical sources— in cosmic rays are protons, whereas 14% correspond to nucleons bound in helium

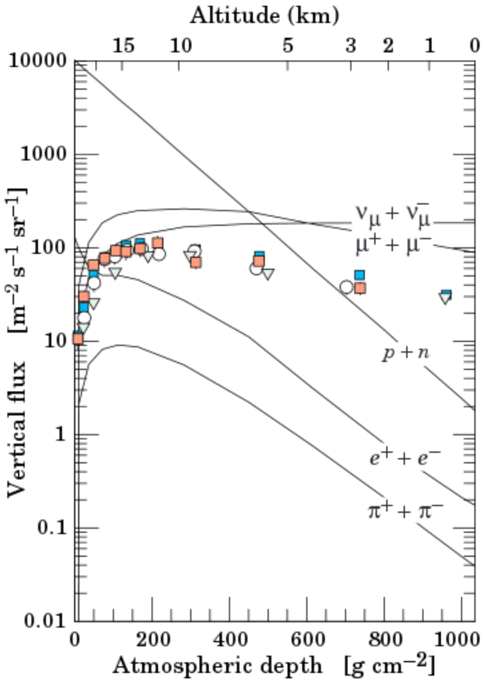

Fig. 4.6 Estimated vertical flux of cosmic rays in the atmosphere for $E > 1\text{GeV}$. The points shows data taken for negative muons fluxes. Except for protons and electrons, all particles are produced in interactions of the primary cosmic rays with the atmosphere. Notice that the flux of muons dominates that of nucleons for altitudes lower than 5 km. Image taken from [48]

nuclei, for an energy range from several GeV to around 100 TeV [48]. These particles arrive to the earth nearly isotropically at most energies, due to diffusion in the galactic magnetic field. The second component of primary cosmic rays are electrons; however, their flux is negligible in comparison to that of primary protons for all energies between 1 - 1000 GeV, as shown in figure 4.6. From the plot it is also evident that neutrinos and muons dominate the cosmic ray spectra at sea level, where the current experiment is being performed. The integral intensity of muons above $1\text{GeV}/c$ at the surface of the Earth is approximately 70 $\text{m}^{-2}\text{s}^{-1}\text{sr}^{-1}$ or, roughly, 1 $\text{cm}^{-2}\text{min}^{-1}$ for horizontal detectors [48]. An extrapolation formula for the muon flux has been obtained [48] for values of the energy for which muon decay is negligible —this is, for values of $E > 100/\cos\theta$ GeV, with θ the incoming angle of the muon—:

$$\frac{dN}{dEd\Omega} = 0.14E^{-2.7}\left[\frac{1}{1+\frac{1.1E\cos\theta}{115\,\text{GeV}}} + \frac{0.054}{1+\frac{1.1E\cos\theta}{850\,\text{GeV}}}\right]\text{m}^{-2}\text{s}^{-1}\text{sr}^{-1}\text{GeV}^{-1}. \tag{4.4}$$

A more precise scheme requires numerical or Monte Carlo calculations in order to account accurately for decay and energy-loss processes, and for energy dependences of the cross sections; luckily, the Lawrence Livermore National Laboratory implemented MC model of the Earth's atmosphere, where primary protons with energies from 1 GeV - 100

TeV are injected at the top [49]; the code traced all relevant secondary particles and tallied their fluxes at specific altitudes. From the results of this simulation they produced data tables and developed a reliable cosmic ray particles' shower generator, CRY (Cosmic Ray shower LibrarY) [50]. Figure 4.7 depicts a muon energy spectra generated with this code.

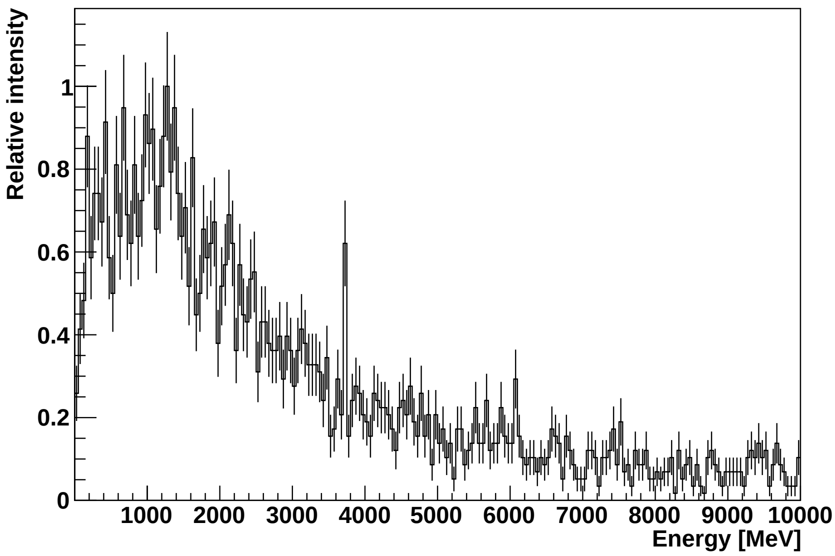

Fig. 4.7 Energy spectra of cosmic muons at sea level, generated using the CRY package [50]. The intensities are normalized to the maximum of the spectra, which happens at an energy $E = 1275$ MeV.

Being highly energetic, these muons will lose energy at an average rate given by [45]

$$-\frac{dE}{dx} = a(E) + b(E)E \tag{4.5}$$

where $a(E)$ is the ionization energy loss given by equation (4.1), and $b(E)$ is the sum of e^+e^- pair production, bremsstrahlung, and photonuclear contributions. Assuming $a(E)$ and $b(E)$ to be slowly varying functions, one gets that the mean range x_0 of a muon of energy E is

$$x_0 \approx \frac{1}{b} \ln\left(1 + \frac{E}{\varepsilon}\right), \tag{4.6}$$

with $\varepsilon = a/b$. This critical energy indicates the point where radiative effects overcome energy loss by ionization. The values of dE/dx for silicon, lead, copper and cadmium telluride are shown in figure 4.8. The values of ε are shown in table 4.2.

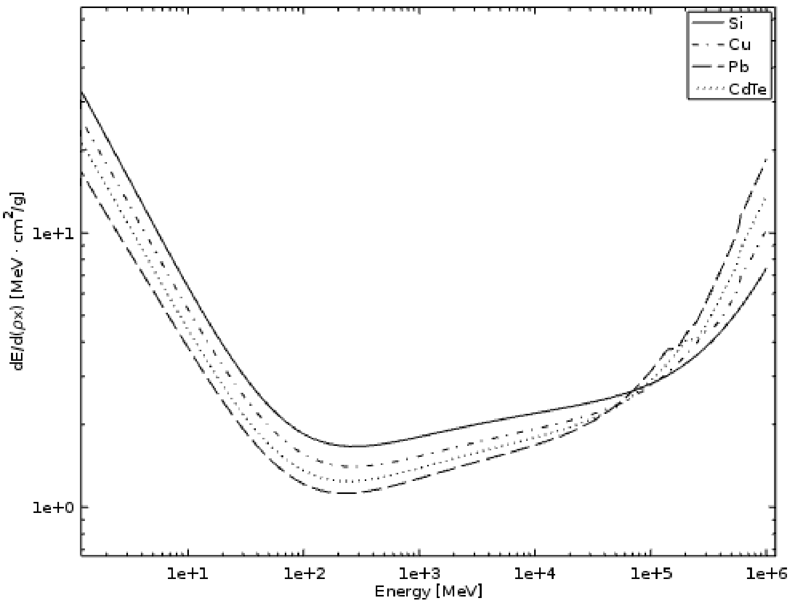

Fig. 4.8 Stopping power for muons in Si, Cu and Pb from 1 MeV to 300 GeV. The value of ε for these materials is: 582 GeV (Si), 317 GeV (Cu) and 141 GeV (Pb). The plot was generated with data from [51]

.

ε values for different materials	
Material	**ε [GeV]**
Pb	141
Cu	317
CdTe	208
Si	582

Table 4.2 Critical energy for muons in lead, copper, cadmium telluride and silicon. Up to this energies, the muons lose energy mainly through ionization. These values have all a relative intensity of less tan 10% (see equation 4.4 and figure 4.7). Data obtained from [51]

4.2 First Measurements

The experimental setup used for the first measurements is shown in figure 4.9. A full sheet with the specifications of the CdTe detector can be found in [52]. The main information is presented in table 4.3.

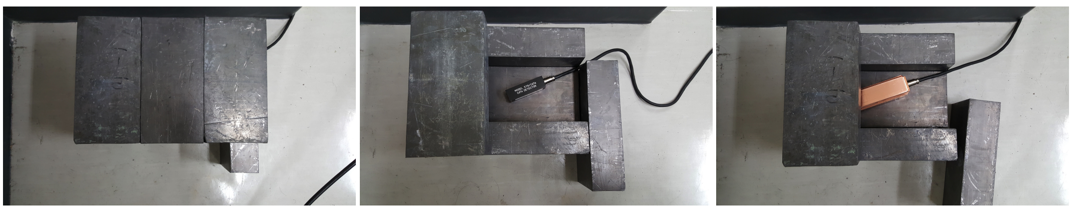

Fig. 4.9 Experimental setup for measuring background events; a total of 8 blocks of dimensions $5 \times 10 \times 20$ cm^3 were used. A better hermeticity was obtained by placing an extra block in the upper right corner, where the cable from the detector (center figure) goes through. The right image shows the CdTe detector covered by the Cu lamina.

CdTe detector characteristics	
Model	579/CdTe
Dimensions [mm^3]	$2 \times 2 \times 0.3_t$
Resolution (FWHM) [keV]	2.5 (1.5)

Table 4.3 Properties of the CdTe detector used in the first background measurements. The resolution was measured as 60 keV for ^{241}Am. Values in parenthesis were measured by us.

Events rate (h^{-1} mm^{-2} keV^{-1}) for energies between		
Measurement	**14.5 keV ± 0.5 keV**	**0.5 keV – 5 keV**
No shield	0.10985 ± 0.02039	$21.495 \times 10^3 \pm 9$
Pb 5 cm	0.08929 ± 0.03993	$14.593 \times 10^3 \pm 16$
Pb 5 cm Cu 6 mm	0.01567 ± 0.00904	$28.560 \times 10^3 \pm 12$
Pb 5 cm Cu 12 mm	0.00757 ± 0.00535	$18.184 \times 10^3 \pm 8$

Table 4.4 Events rate for the four measurements performed, at 14.5 keV, and from 0.5 keV to 5 keV.

Four measurements were performed: one without any shielding (66 hours), one with only a 5 cm lead shielding with improved hermeticity (left image, figure 4.9 – 14 hours), one with a 5 cm lead shield and a 6 mm copper shield (48 hours) and one with a 5 cm lead shield and a 12 mm copper shield, also with improved hermeticity (66 hours). The improvement comes from the shielding of the upper right corner in figure 4.9 (center) with an extra lead block. Figure 4.10 shows the measured data for energies up to 600 keV (up plot) and 50 keV (bottom plot).

The total number of events between 13 keV – 16 keV and between 0.5 keV – 5 keV for each measurement are shown in table 4.4. A binning of 2 keV/bin was used, making a compromise between the measured and the reported resolutions.

The spikes at energies below 10 keV for all four data can be associated with X-rays emission from the outermost electron shells of CdTe due to thermal excitation. Each peaks represent the center of a bin with a width of 2 keV; hence, shell M1 for telluride, with an energy of 1.006 keV, explains the peak at 1 keV; shells L3 and L2 for cadmium (with energies of 3.578 keV and 3.727 keV, respectively) would explain the peak at 3 keV, and shell L1 for cadmium and telluride shells L3, L2 and L1 (which have energies ranging from 4.018 keV to 4.939 keV) would account for the peak at 5 keV [44].

It also becomes evident that WIMP search is non-viable at the current stage; comparing with the background events rate reported by XENON1T [37], the current background is rougly 10^{10} times bigger; though this number is expected to diminish once the XRPIX is used and the thermal noise reduced by using the thermal chamber, the results presented in the next chapter still reject the idea of a WIMP search at this moment. For axions, as mentioned in chapter 2, T. Namba [18] reported a background rate of 4.07×10^{-3} h^{-1} mm^{-2}

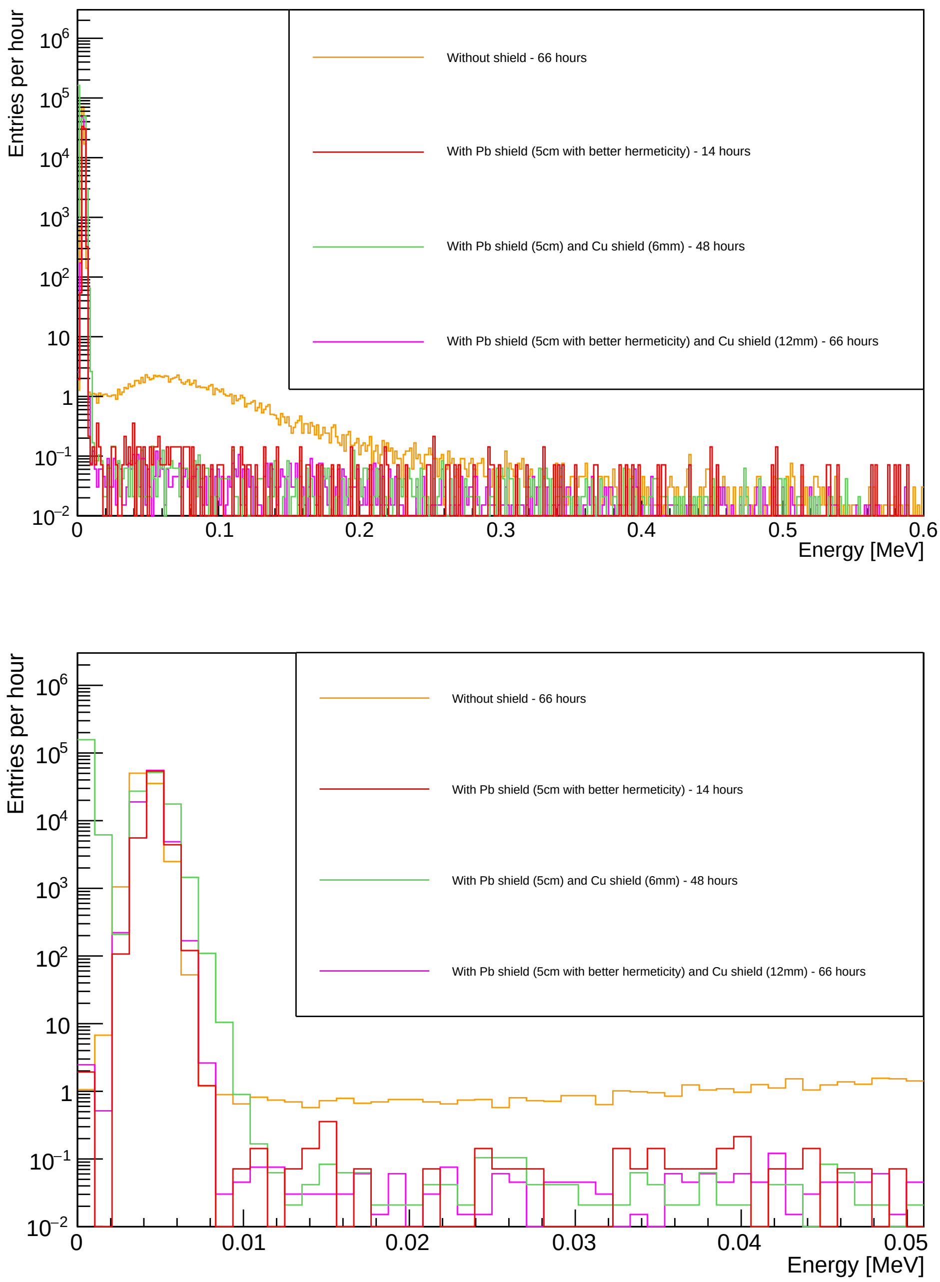

Fig. 4.10 Data taken with the CdTe detector [52].

keV^{-1}. A comparison with the best counting rate obtained in the current analysis shows that an improvement in the background rejection for axion search is also needed, recalling that Derbin *et al* [53] reported a rate of 1.09×10^{-3} h^{-1} mm^{-2} keV^{-1}. Using Derbin's rate as our benchmark, it is seen that an improvement in the background suppression factor of around 18 is required.

It rests to be tested, however, if the full set up, explained in chapter 3, can deliver more promising results.

4.3 Simulations

In order to interpret the data obtained, the effect of the shielding materials on the different background sources needs to be studied; for this, a set of simulations were performed, using the Geant4 simulation toolkit [54].

Lead was tested against the four sources mentioned in section 4.1, using the geometry shown in figure 4.11. The energies for α, β and γ particles were the ones from the ^{238}U, ^{232}Th and ^{40}K spectrum added according to their relative abundance in concrete (see figure 4.5); the energies for muons were determined from the spectrum in figure 4.7. The results showed that α and β radiation are completely stopped within the first 5 cm of lead, whereas γ rays present an exponential reduction, in accordance with equation 4.3. Cosmic rays, as minimum ionizing particles, did not present any significant reduction, and they produce the same number of secondary electrons and gammas at all depths (see table 4.6).

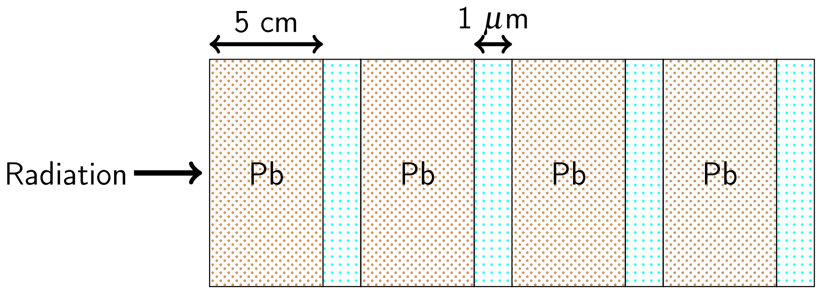

Fig. 4.11 Scheme for measuring the shielding properties of lead. A particle (α, β, γ or μ) is fired directly to the arrangement. In between each lead block there is a sensitive region of 1 μm thickness which measures the energy of the particles traversing the shield. The transversal area of the lead layers is 15×15 cm^2.

Number of remaining particles for every 10^6 incident (95% C.L.) at				
Particle	**5 cm**	**10 cm**	**15 cm**	**20 cm**
α	< 3	< 3	< 3	< 3
β	< 3	< 3	< 3	< 3
γ	$38.2 \times 10^3 \pm 376$	$3.43 \times 10^3 \pm 115$	351 ± 37	39 ± 12
μ	$981.6 \times 10^3 \pm 264$	$969 \times 10^3 \pm 340$	$954 \times 10^3 \pm 411$	$937 \times 10^3 \pm 476$

Table 4.5 Number of particles which are not absorbed after traveling distance of 5, 10, 15 and 20 centimeters in lead, from 10^6 originally fired at 95% C.L.

From these simulations we also obtained the energy spectrum of secondary photons and electrons produced by: *1.* The interaction of γ rays with the lead shield, *2.* The interaction of

Number of Secondaries at 5 cm			
Particle	Radioactivity (β)	Radioactivity (γ)	μ
e	0	932 ± 59	$(126.8 \pm 0.7) \times 10^3$
γ	14 ± 7	1832 ± 82	$(805.2 \pm 1.7) \times 10^3$
Number of Secondaries at 10 cm			
Particle	Radioactivity (β)	Radioactivity (γ)	μ
e	0	90 ± 18	$(127.2 \pm 0.7) \times 10^3$
γ	0	185 ± 26	$(881.0 \pm 1.8) \times 10^3$
Number of Secondaries at 15 cm			
Particle	Radioactivity (β)	Radioactivity (γ)	μ
e	0	< 5	$(125.9 \pm 0.7) \times 10^3$
γ	0	21 ± 9	$(865.9 \pm 1.8) \times 10^3$
Number of Secondaries at 20 cm			
Particle	Radioactivity (β)	Radioactivity (γ)	μ
e	0	0	$(55.70 \pm 0.5) \times 10^3$
γ	0	5 ± 4	$(662.2 \pm 1.7) \times 10^3$

Table 4.6 Number of secondary particles (electrons and photons) produced by the interaction with the lead shield at different depths; the second and third columns represent the number of secondaries produced by the passing of β and γ rays from uranium, thorium and potassium decay chains. The fourth column is the number of secondaries produced by the passing of cosmic muons. For each column, 10^6 particles were fired. All the values are presented with a 95 %C.L. interval. Notice that for the number of secondaries at 20 cm produced by muons diminishes by half in comparison with the other thicknesses; this is due to the fact that there is no lead material in front of the last sensor, whose interactions with the cosmic muons accounts for roughly half of the signals counted.

cosmic muons with the lead shield, and *3.* Lead radioactivity. There was not background associated with β rays produced by the environment. Also, the spectra of the γ radiation and of the cosmic rays that made it through the first shield were generated. All of this spectra —eight in total— were used to test the copper effectiveness in rejecting different types of background present inside the lead shield using the geometry shown in figure 4.12.

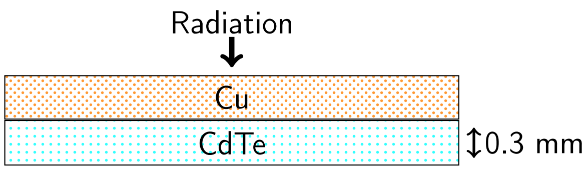

Fig. 4.12 Scheme for measuring the shielding properties of copper. The copper plate has two possible values for its thickness: 6 mm and 12 mm. The transversal area of both Cu and CdTe layers is of 2×2 mm^2.

In the simulations, 10^6 particles generated by each of the processes mentioned before —EM showers by muons, EM showers by γ radiation, radioactivity of the lead blocks (for the case of electrons), and environmental radioactivity (for the case of photons)— were fired, and the energy deposited by each one in the CdTe after crossing the copper plate was stored. The results are shown in figures 4.13 and 4.14.

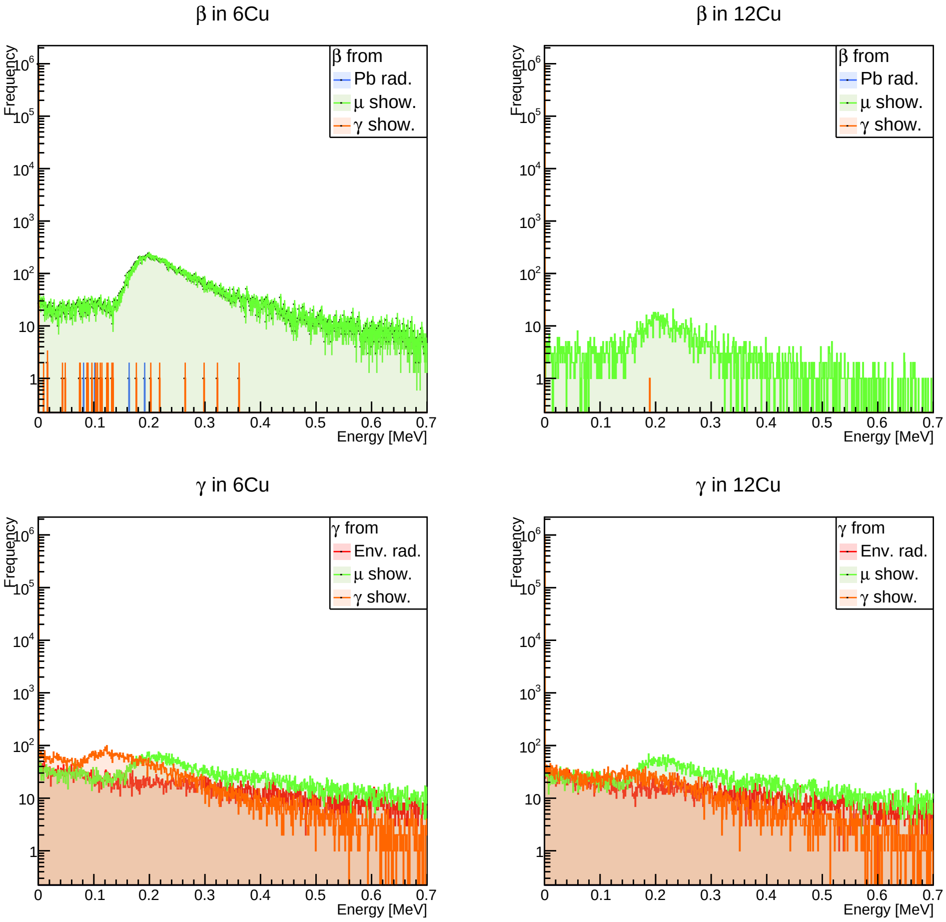

Fig. 4.13 Spectra of energies deposited in the CdTe by electrons (top) and photons (bottom) from different sources. The frequencies do not represent the true relation between the intensities of each process.

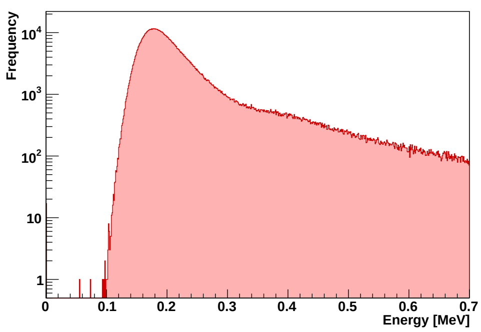

(a) μ - 6 mm

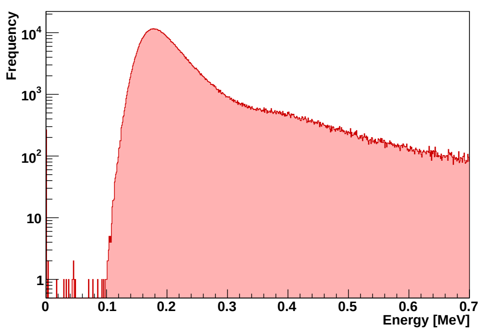

(b) μ - 12 mm

Fig. 4.14 simulation results of the energy deposited in the CdTe detector by cosmic μ with a copper layer of 6 mm (left) and 12 mm (right). The total number of simulated events is 10^6 for both cases.

It is seen that raising the copper thickness has a positive effect on the rejection of all kinds of electrons. On the other side, only secondary photons from γ rays seem to be affected by this increment (a reduction of one order of magnitude for energies under 0.3 MeV). Muons do no seem to be affected by any of the two shields, which seems to indicate that the γ particles generated by muons are produced by bremsstrahlung.

Finally, a MC estimation for the detection efficiency at 14.4 keV for the CdTe and XRPIX detectors was performed. For the XRPIX detector, the silicon bulk was considered together with the silicon dioxide and aluminium layers included, and back ilumination was implemented, whereas for the CdTe detector was assumed to be covered by a plexiglass case layer of 2 mm thickness. The results are shown in table 4.7.

XRPIX2b	**CdTe**
72.4570 %	69.0554%

Table 4.7 Detection efficiency for the XRPIX2b and the CdTe detector for photons at 14.4 keV.

4.4 Analysis

It results convenient to name the previous experimental measurements as

Measurement	**Name**
No shield	NS
5 cm Pb shield	5Pb
5 cm Pb shield and 6 mm Cu shield	6Cu
5 cm Pb shield and 12 mm Cu shield	12Cu

Data from NS is likely to contain multiple background sources, which a first analysis cannot account for. Moreover, an analysis of the sources that do have a probability of reaching the detector is more meritorious. At the same time, though data in 5Pb is the best source to test for lead radioactivity, it seems incomplete (notice, for example, the region with no inputs around 9, 16, 22 and 30, keV in figure 4.10, even though better shielded setups, 6Cu and 12Cu, do have entries for these values).

From the discussion developed in section 4.1 and the simulations performed in 4.3, α and β rays from the most common radionuclides are expected to be totally blocked by the minimum shielding scheme of 5 cm Pb and 6 mm Cu. The results also show that no gamma radiation from the lead makes it through any of the two configurations, as expected[2]. We conclude that the only kind of radiation that reaches the detector in the last two measurements

[2]The most energetic photons ^{210}Pb emits have an energy of 803.052 keV, and come from the decay of ^{210}Po; from figure 4.4, the mass attenuation coefficient for Cu at this energy is 0.1 cm^2/g or 0.896 cm^{-1}. This implies that after 6 mm, the original intensity of the γ rays has dropped to 4.62% of its original value. To lower energies correspond higher values of μ, so no radiation from Pb is expected to be found.

Best values for the parameters in equation (4.7)	
A_c	$2.684(61) \times 10^{-5}$
B_c [MeV^{-1}]	$-2.566(105) \times 10^{-5}$
C_c [MeV^2]	$5.357(218) \times 10^{-6}$
Γ_c [MeV]	$8.316(375) \times 10^{-2}$
E_c [MeV]	$2.200(3) \times 10^{-1}$

Table 4.8 Best values for the fit in figure 4.15.

(the ones containing copper shields) are γ rays from other type of contamination in lead, γ rays from environmental radioactivity, cosmic muons and the electromagnetic showers they all develop.

Cosmic muons act as minimum ionizing particles, which implies their energy loss is small compared with their kinetic energy. Effectively, from the simulations, 6Cu and 12Cu lead to similar results (see figure 4.14); the minimum energy deposited by these particles is 100 keV, which is far above the region of interest. However, for the 12Cu case there are some minor events below 100 keV, probably due to bremsstrahlung or delta rays in the copper. Being it so, we infer that muons do not contribute *directly* to the relevant background sources for this experiment.

On the other side, the EM showers initiated by the cosmic muons in the lead blocks do contribute to the background spectrum for energies under 100 keV. Since the number of photons produced in these showers that reach the detector is roughly 6.4 times bigger than the number of electrons (see table 4.6), we assume the shower is fully composed by photons. We then regard this background as the sum of a linear background and a lorentzian peak:

$$\mathrm{Bk}_{\text{cosmic showers}} = A_c + B_c E + \frac{C_c}{2\pi} \frac{\Gamma_c}{(E - E_c)^2 + (\Gamma_c/2)^2}. \tag{4.7}$$

From figure 4.15, we see there is no expected attenuation in the cosmic background after increasing the Cu thickness. The values of the parameters in equation (4.7) that give the best fit are given in table 4.8.

Next, we model the background of photons produced by the interaction of γ rays with the lead shield by a function of the form:

$$\mathrm{Bk}_{\gamma\,\text{showers}} = A_s e^{B_s E} + \frac{C_s}{2\pi} \frac{\Gamma_s}{(E - E_s)^2 + (\Gamma_s/2)^2}. \tag{4.8}$$

However, this is the part of the background that presents a reduction by the introduction of copper. This implies that the parameters are different for the cases of 6Cu and 12Cu. The

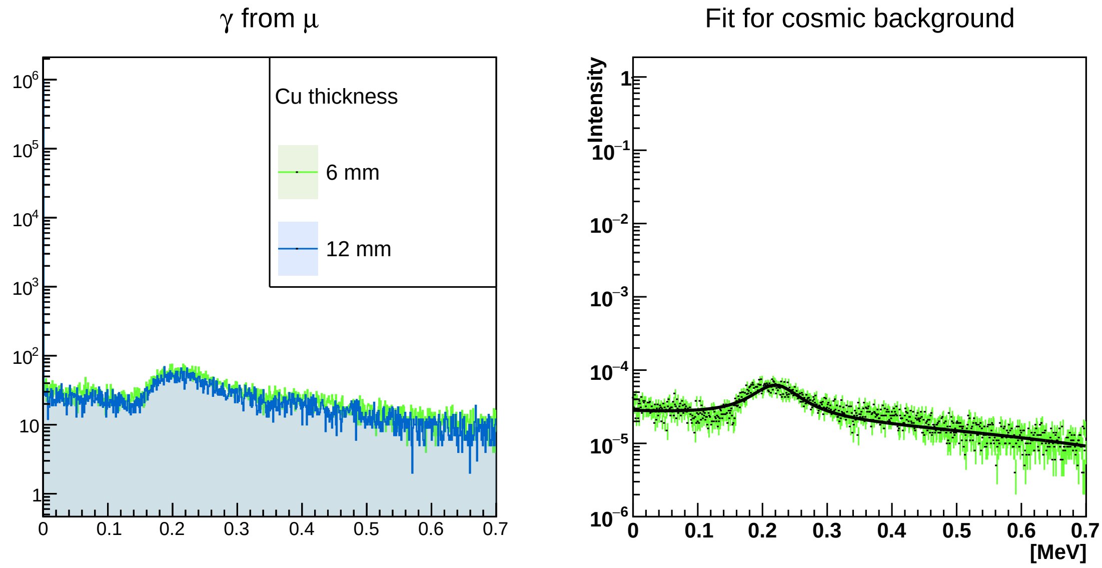

Fig. 4.15 In the left, the spectrum of γ particles produced by the interaction of cosmic rays with the lead material for the 6Cu and 12Cu cases. In the right, the best fit for this simulated spectrum.

best fitting for both histograms is shown in figure 4.16, and the parameters values in table 4.9.

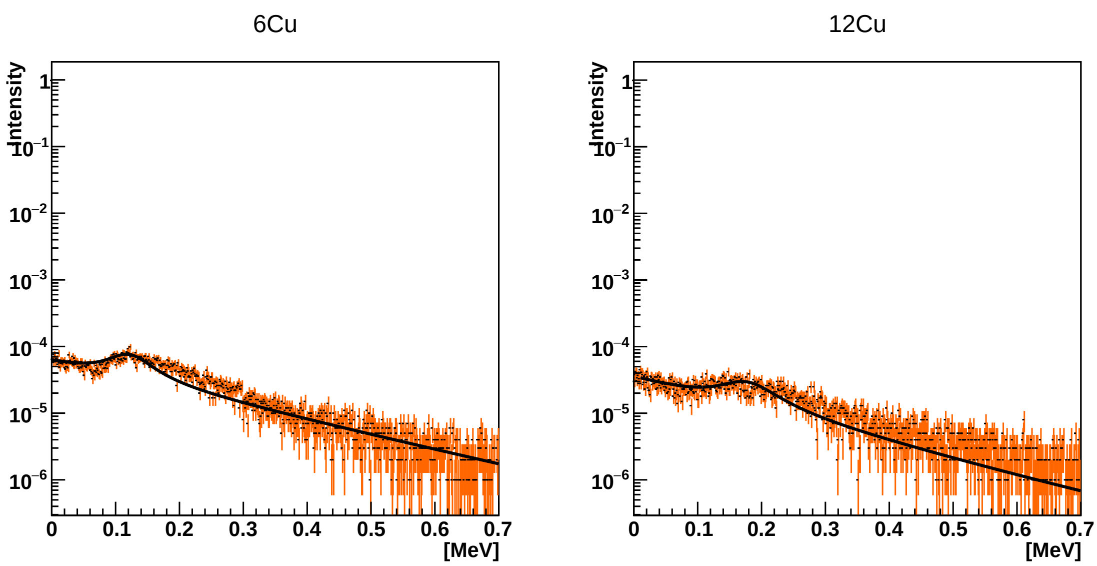

Fig. 4.16 In the left, the spectrum of photons produced by the interaction of γ rays with the lead material for the 6Cu case. In the right, the same for the 12Cu case.

Finally, we analyze the background coming from the environmental radioactivity; this is, γ particles that suffered compton scattering or that made it through the shield without losing any of their energy. This background did not present a significant reduction (as seen in figure

Best values for the parameters in equation (4.8)		
Parameter	**6Cu**	**12Cu**
A_s	$5.899(122)\times10^{-5}$	$3.449(76)\times10^{-5}$
B_s [MeV^{-1}]	$-5.221(61)$	$-6.011(000)$
C_s [MeV^2]	$5.6313(180)\times10^{-6}$	$2.875(118)\times10^{-6}$
Γ_s [MeV]	$8.000(25)\times10^{-2}$	$1.037(00)\times10^{-1}$
E_s [MeV]	$1.200(00)\times10^{-1}$	$1.749(00)\times10^{-1}$

Table 4.9 Best values for the fit in figure 4.16 for the 6Cu and 12Cu cases.

4.17), and hence we model it with a simple linear function:

$$\mathrm{Bk}_{\mathrm{radio}} = A_r + B_r E. \tag{4.9}$$

The best fit is shown in figure 4.17. The parameters are

$$A_r = 2.622(33)\times10^{-5}$$

and

$$B_r = -3.305(69)\times10^{-5}\ \mathrm{MeV}^{-1}.$$

It is interesting to notice that the negative value for the B parameter in all functions; this suggests that the background intensity decreases as the energy rises for all kinds of sources.

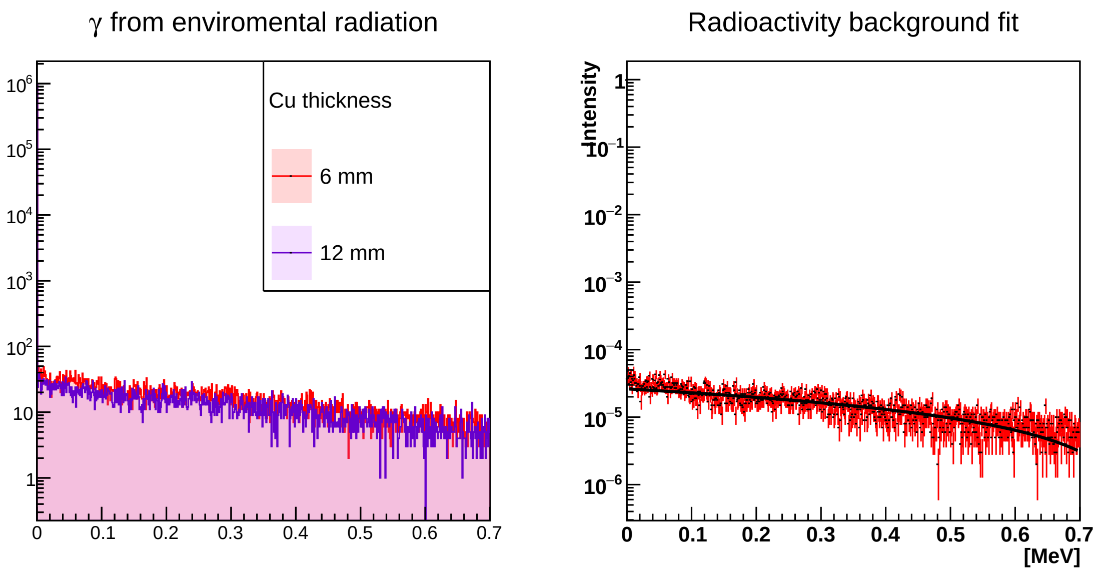

Fig. 4.17 In the left, the spectrum of γ particles produced by radioactivity outside the shields, that made it through 5 cm of lead for the 6Cu and 12Cu cases. In the right, the best fit of this simulated spectrum.

We next model the background in 6Cu and 12Cu as generated by the terms in equations (4.7), (4.8) and (4.9):

$$\mathrm{Bk} = K_c \mathrm{Bk}_{\text{cosmic showers}} + K_s \mathrm{Bk}_{\gamma\,\text{showers}} + K_r \mathrm{Bk}_{\text{radio}}. \tag{4.10}$$

From tables 4.5 and 4.6, we see that for 38.2×10^3 photons from external radioactivity, 1.832×10^3 secondary γ are produced by the primaries interaction with lead. Then it would be expected for $K_r \approx 20.85 K_s$; however, this is not the case. In the analysis, we overlooked the effect of other particles present in cosmic rays, such as photons and protons; moreover, we *have not taken into account radioactivity present in the inner components of the CdTe detector*. By letting K_r take values higher than K_s we intend to account for these sources.

We expect to obtain similar results for both fits, since the reduction produced by the thicker copper layer has been already considered, and its effects are enclosed in the different values for the fit parameters A_s, B_s and C_s (and the increasing in Γ_s) in the 12Cu case, compared with the 6Cu ones. The fits are shown in figure 4.18 and the results for K_c, K_s and K_r in table 4.10.

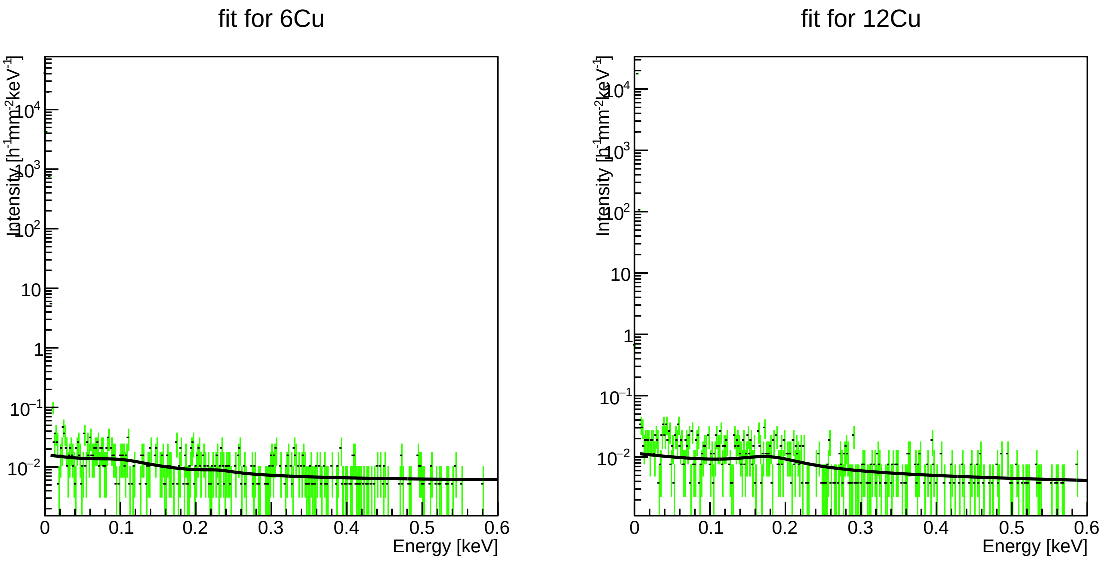

Fig. 4.18 Best fits of the background model proposed in equation 4.10 to the 6Cu and 12Cu data.

From these results we deduce that one of the primary sources of background are cosmic rays, as expected. Though the cosmic showers cannot be reduced by increasing the thickness of the lead or the copper shields, the secondary photons produced by radioactivity do diminish with the introduction of copper in the shielding. At the same time, from table 4.7, a thickness of 15 cm in lead carries a reduction by a factor of 2.85×10^3 in the background associated

Fitting constants [$h^{-1}mm^{-2}keV^{-1}$] for the spectra of the CdTe detector			
	Enviromental radiation (K_r)	**Cosmic showers (K_c)**	**γ showers (K_s, includes other sources)**
6Cu	$2.897(192)\times10^{-1}$	$0.143(370)\times10^{2}$	$0.928(165)\times10^{2}$
12Cu	$2.279(119)\times10^{-1}$	$0.523(280)\times10^{2}$	$10.738(598)\times10$
Mean	$2.588(160)\times10^{-1}$	$0.333(328)\times10^{2}$	$1.009(124)\times10^{2}$

Table 4.10 Fitting constants obtained for the 6Cu and 12Cu data, from the background model developed in the simulations. The detection efficiency of the CdTe detector was not taken into account. The events rate at low energies can be approximated by $K_cA_c+K_rA_r+K_sA_s$.

with environmental radioactivity. Being it so, a configuration of 15 cm of Pb and 20 mm of Cu is suggested.

We estimate the expected events' rate for the XRPIX under similar conditions by two methods: first, from the data in table 4.10, we calculate the total events rate (dividing by the detection efficiency of the CdTe) and multiply by the detection efficiency of the XRPIX. At 14.4 keV, any contribution besides the terms A_c+BcE, $A_se^{B_sE}$ and $Ar+BrE$ can be ignored. We thus obtain

$$R_{\text{XRPIX}}=\frac{\varepsilon_{\text{XRPIX}}}{\varepsilon_{\text{CdTe}}}\left[K_r\left(A_r+B_rE\right)+K_c\left(A_c+B_cE\right)+K_sA_se^{B_sE}\right]. \tag{4.11}$$

The second method is to use the events rate in table 4.4. Then

$$R_{\text{XRPIX}}=\frac{\varepsilon_{\text{XRPIX}}}{\varepsilon_{\text{CdTe}}}R_{\text{CdTe}}. \tag{4.12}$$

The results for both estimations are shown in table 4.11.

Estimated background rate for the XRPIX at 14.4 keV ($h^{-1}mm^{-2}$ keV^{-1})		
Configuration	**From equation (4.11)**	**From equation (4.12)**
6Cu	$0.161(171)\times10^{-1}$	$0.164(95)\times10^{-1}$
12Cu	$0.112(134)\times10^{-1}$	$0.079(56)\times10^{-1}$

Table 4.11 Estimated background rates for the XRPIX2b under the 6Cu and 12Cu set ups.

The uncertainty in the predictions of the model are due to the lack of data in the region of interest, and to the choice of the initial parameters in the fitting model. It is compulsory to proceed with new background measurements, this time for more extensive periods of time, under lower temperatures (in order to reduce the noise below 10 keV) and employing the XRPIX detector. A reduction by a factor of 109 over the background related to environmental

	Namba (07)	Derbin (11)	Current
Background $[\times 10^{-3}/(\text{mm}^2 \text{ h keV})]$	1.76	1.09	< 1.23
Energy resolution at 14.4 keV [keV]	2.36	1.48	0.58*
Temperature [K]	205	77.35	223.15

radioactivity for the 6Cu configuration is expected by using 15 cm of lead, and a reduction by a factor of 2 in the background related to γ showers by the use of a 12 mm Cu shield. Extrapolating exponentially to 20 mm, the reduction is found to be of a factor of 10 in comparison with the 6Cu data. Moreover, since the values of all the A are similar ($\sim 3 \times 10^{-5}$), we can take the sum $A_r + A_c + A_s$ as being proportional to the total background rate at low energies. Hence, 15 cm of Pb plus 20 mm of Cu are found to yield a reduction of roughly

$$\frac{K_r + K_c + K_s}{K_r/109 + K_c + K_s/(10)} = 3.26$$

times the background measured for 6Cu. This is closer to the benchmark set by Derbin *et al*; furthermore, by the use of active shields for rejecting the cosmic background, a background level close to 1.09×10^{-3} h^{-1}mm^{-2} keV^{-1} can be achieved. Effectively, assuming the cosmic muons' background can be completely rejected by the use of a scintillator, one obtains

$$R_{\text{XRPIX}}\,(14.4\text{ keV}) \approx \frac{K_r/109 + K_s/10}{K_r + K_c + K_s} \times 0.164 \times 10^{-1} = 1.23 \times 10^{-3}\text{ h}^{-1}\text{ mm}^{-2}\text{ keV}^{-1}.$$

We, however, expect the actual background rate to be lower than this value, since: *1.* We did not take into account the effect of the thermostatic chamber in reducing the thermal noise, and blocking part of the external radiation; and *2.* the XRPIX detector is expected to have components with higher purity, hence leading to a lower *internal* radioactivity (implying a smaller value for K_s). As a closure, we present the expected background rates and energy resolutions for the current experiment, as well as for the previous ones, in table .

Chapter 5

Cluster Analysis Framework

As we saw in the previous chapter, the mere use of passive shields, even in their best configuration possible, is not enough to reduce the background rate for this experiment to the levels required. Hence, the use of active shields was suggested. One of these corresponds to a scintillator located on the top of the thermal chamber, which acts as a VETO counter for cosmic muons. A second technique proposed is to pre-analyze the data stored by the XRPIX and reject it if it does not coincide with the expected signal.

Some studies have explored the particular responses a pixel detector has to different types of radiation [55, 56]; alpha particles, for example, being highly energetic and having a small penetration depth, are likely to deposit all of their energy on the surface of the detector in one single hit, producing a very large circular —a typical radius is of the order of some millimeters—, symmetric cluster; high energy electrons, on the other side, are more penetrating, and are prone to experience multiple scattering before losing all of their energy; therefore, the track they leave behind is usually gnarled, thin and asymmetric. Low energy ones lose all their energy after a few μm in the detector material. Photons of low energy are completely absorbed by the detector material, but in contrast with the α particles, the spatial extension of the cluster is usually of the order of tenths of micrometers; γ rays with energies of some MeV have usually bigger tracks, but these particles are less likely to be fully absorbed by the detector material, and so their cluster size is still not comparable to the α's one. One can then make use of the geometrical properties of the print left by radiation in order to identify it.

The necessity of an analysis like this seems arguable. Indeed, in the energy range of this experiment there are no α particles, and it seems electrons can be effectively rejected by the copper and lead shields. Moreover, clusters left by particles with energies up to 50 keV cannot be properly differentiated: photons deposit all their energy in one single interaction, whereas 50 keV electrons have an stopping power of around 16.3 MeV/cm in silicon (see figure 4.3); they travel a mean distance of 30.68 μm before being stopped, which is roughly the size of one pixel. Therefore, the cluster shape for both low energy photons and electrons is more likely to be determined by charge diffusion, which is independent of the incoming particle.

Two replies are given: first, the radioactivity from the lead blocks was overlooked in the previous analysis, under the assumption that it was only produced by radioactive isotopes of lead present in the shielding blocks; however, the existence of other radionuclides is possible, and only a more extense, detalied background analysis can settle this; if there were other radioactive sources in the lead material, it is probable copper is not enough to block most of them. Moreover, chances of contamination of the detector materials by the ^{222}Rn in the air increase with time. A cluster analysis may not only work as a method to reject this otherwise persistent background, but it also serves as a tool for radiography. Effectively, cluster analysis has been employed in the DAMIC colaboration in the next way: cluster shapes are used to identify the kind of radiation hitting the detector; from here, and with the energy of the particle, decay chains can be traced, given that two or more clusters with the appropriate energies and produced by the adequate particles are within the vicinity of each other [57]. Second, this analysis scheme extends the range of applicability of the XRPIX detector to other areas of research; more about this in section 5.1.

This chapter portrays the first prototype of such a clustering framework developed for the XRPIX. Section 5.1 describes the data output format that the XRPIX uses, and the methods used to pre-process this data and construct the clusters; then, section 5.2 addresses the simulations performed in order to stablish adequate parameters for cluster identification; finally, 5.3 shows the first results of this scheme.

5.1 Pixel Clustering

As the original purpose of the XRPIX was to search for X-rays in astronomical satellite missions [38], its event driven mode (for an explanation of the modes of operation of the XRPIX detector see chapter 3) assumes all events recorded are produced by the interaction of photons with the silicon sensitive layer. In chapter 4 it was seen that the intensity of a photons beam is reduced by a factor of $\exp(-\mu x)$ after traveling a distance x in a material with attenuation coefficient μ. The value of μ is also related to the mean free path of photons in the material, λ; indeed

$$\lambda_\gamma = \frac{1}{\mu}.$$

For silicon, at energies around a few MeV, the value of λ is roughly 4.3 cm; since the thickness of the XRPIX is 500 μm at most, it is very unlikely for high energy photons to interact more than once with the detector; for low energy photons photoelectric effect is dominant, so these photons too experience at most only one interaction. Thus, the expected signal from X-rays is a very symmetric one, containing few pixels, since the charge distribution is not governed by multiple particle-detector interactions but by charge diffusion in the bulk material. Because of this, in the event driven mode, the XRPIX only stores the data of clusters with the shapes shown in figure 5.1.

Though the XRPIX does not take into account clusters 11, 21, 31, 42 and 100 when building the final spectra of the data, these clusters do happen quite often. As an example, consider figure 3.3 in chapter 3; this spectra was constructed using 823.358×10^3 events with clusters 10, 20, 30, 40, 41 and 50; there were also 135.047×10^3 rejected events; 3.678×10^3 with label 11, 1.694×10^3 with label 21, 451 events with label 31, 420 events with label 42, and 86.155×10^3 events with label 100. Together, they represent 14.1% of the total data.

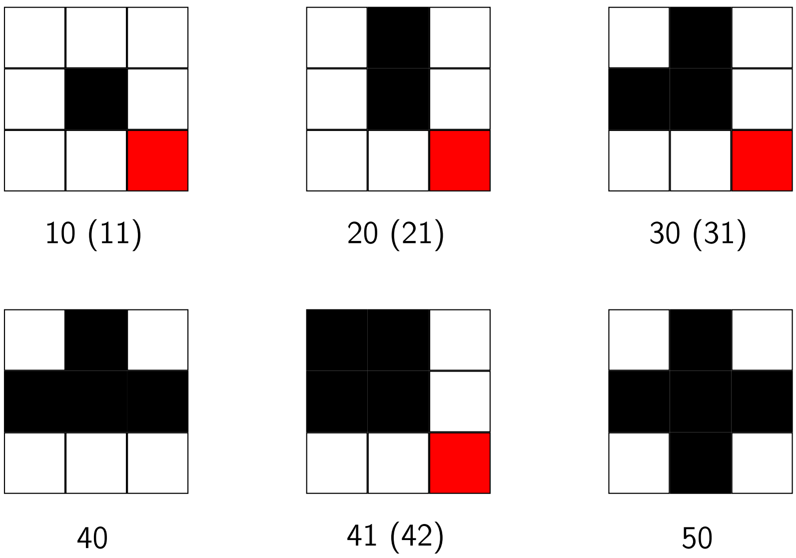

Fig. 5.1 Clusters analyzed by the XRPIX2b in the event mode. The number under each figure indicates the label used for the pattern; the central pixel is the one with the highest signal. For figures with two numbers, the combination of black and red pixels correspond to the number in parenthesis; these kind of events are not considered by the XRPIX2b when writing the output data. Any other cluster pattern not shown in here is catalogued as 100.

On the other side, consider figure 5.2. These are images of β rays from a ^{90}Sr source, and α rays from ^{241}Am taken by the XRPIX frame mode. As it is easily seen, the clusters of these two types of radiation differ strongly from any of the patterns in figure 5.1; hence, any attempt to isolate a single event using the event driven mode in the XRPIX would lead to very poor fits.

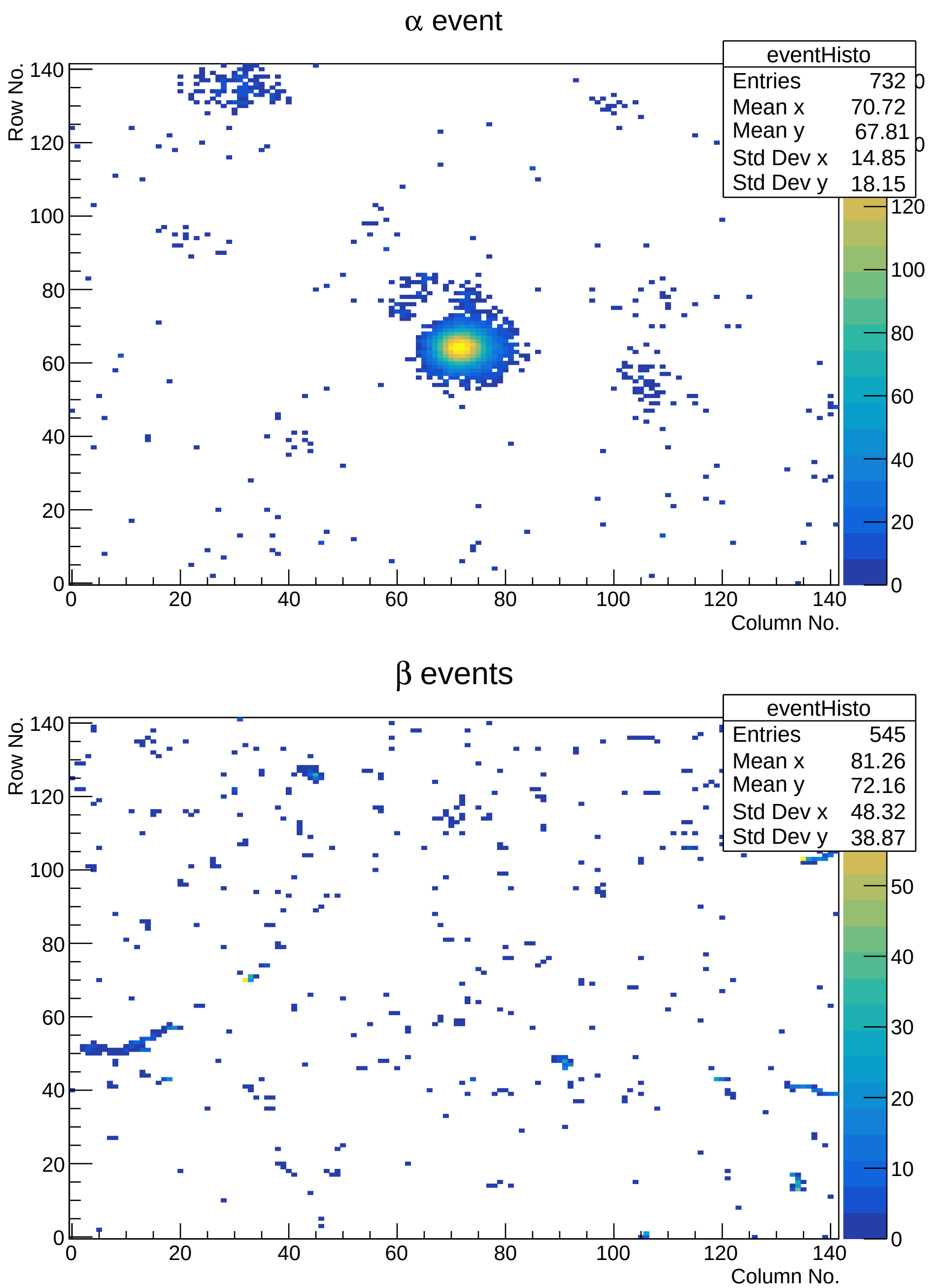

Fig. 5.2 Images obtained after pre-processing of the XRPIX data. In the top: cluster left by an alpha particle from Americium-241 (center of the frame). In the bottom: clusters left by beta particles from Stronium-90 (a very energetic one is seen around the coordinates [53,12]).

These facts clearly show that, in aiming to extend the reach of the XRPIX usefulness —this is, use it to study other types of radiation—, a more versatile clustering framework is needed.

We propose a new clustering framework. This process would start by filtering the raw data obtained by the XRPIX: a simple cut was set for pixels p with a signal s_p such that

$$s_p \in [\mu_n - k\sigma_n, \mu_n + k\sigma_n] \tag{5.1}$$

where μ_n is the mean noise per pixel in the chip, σ_n is the standard deviation of the noise distribution (a Gaussian fit is implemented), and k an integer (the minimum value of k used is 3).

The remaining pixels are the ones to be clustered. In order to do this, it is necesary for us to categorize an event —this is, to decide what constitues a single cluster in the experiment—. We regarded a cluster as a collection C_ε of pixels $\{p_1, ..., p_n\}$ such that for any pixel $p_i \in C_\varepsilon$ there is a pixel $p_k \in C_\varepsilon$ whose distance to p_i is less or equal to ε, and we developed an algorithm wich finds this type of clusters in the filtered data. Since it is not possible to know at first how many events there are in a given frame, a clustering algorithm that works for any number of clusters was needed; moreover, since there are no further restrictions in the definition of cluster, it should be able to find clusters of any shape. Because of this, the DBSCAN (Density-Based Spatial Clustering of Applications with Noise) algorithm was employed [58]. DBSCAN performs the process shown in figure 5.4 until all data points have been visited. The value of ε was chosen to be 30 μm, this is, the distance between two adjacent pixels (for the XRPIX2b). N is the minimum number of neighbors needed to form a cluster; in this case, pixels of all size must be considered, so $N = 0$. The results for a test on the algorithm —with $N = 3$ and $\varepsilon = 43.5$ μm— are shown in figure 5.3. Notice that a value of N higher than zero can help to reduce the tails produced by charge diffusion.

5.2 Signal Simulations

Once the clusters are obtained through the DBSCAN algorithm, the next parameters are also established:

- Size (number of pixels).
- Signal (sum of the signal of included pixels).
- Cluster's center coordinates (coordinates of each pixel weighted by its signal).

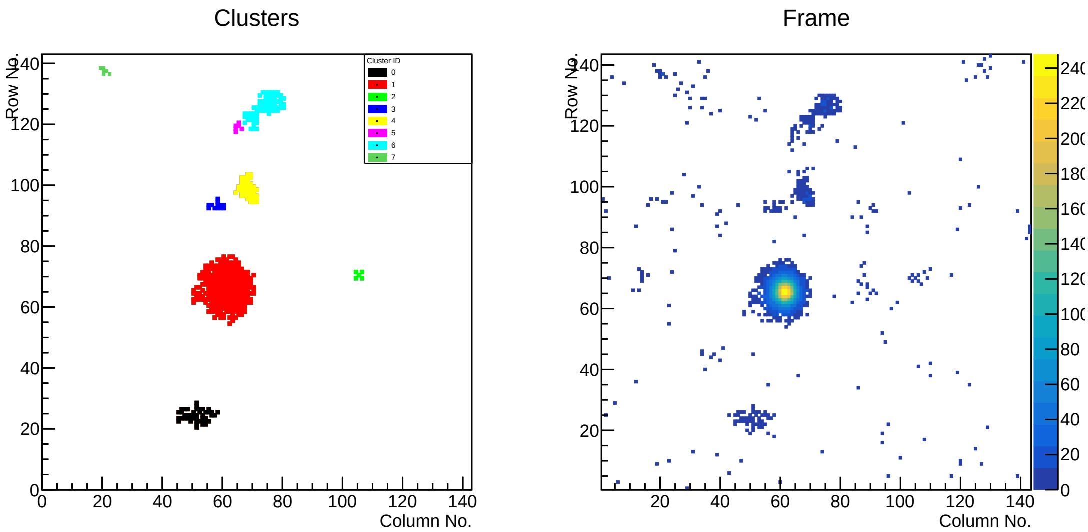

Fig. 5.3 Clusters detected through DBSCAN (left) and the original frame (right). Notice that the violet cluster is smaller (shorter) than the original in the frame. This is because DBSCAN is a density base clustering algorithm. The number of neighbors in a straight line is only 2, which is smaller than the requirement imposed for this case. However, in the general case, a value of $N = 0$ is used, so only the maximum distance ε determines the shape of the cluster.

- Bounding box dimensions (number of columns and rows of the smallest rectangular box that can contain the cluster totally).
- Center coordinates of the bounding box.

We believe that these topological parameters are enough, when possible, to identify the particle producing the cluster. The size and signal of the clusters stablish a clear distinction between α particles and other kinds of radiation. Moreover, the DAMIC colaboration [57] uses the occupation ratio, which is the ratio between the size of the cluster and the bounding box, to effectively separate β and α events of similar energies. This information is stored using the ROOT Data Analysis Framework [59] developed at CERN. A scheme of the file structure is shown in figure 5.5.

In order to get a better understanding of the cluster properties of different types of radiation in the XRPIX detector, a simulation of the signal production was carried out, following Benoit and Hamel [60] and Kraphol [61], who have performed similar studies.

The process starts with the generation of electron-hole pairs throughout the detector geometry. A particle depositing an energy E in the detector will create an average of N electron-hole pairs, with

$$N = \frac{E}{\varepsilon} \tag{5.2}$$

where ε is the ionization energy of the material; for the case of silicon, it is 3.6 eV. The true number of pairs tends to fluctuate due other forms of energy disipation (specially phonon

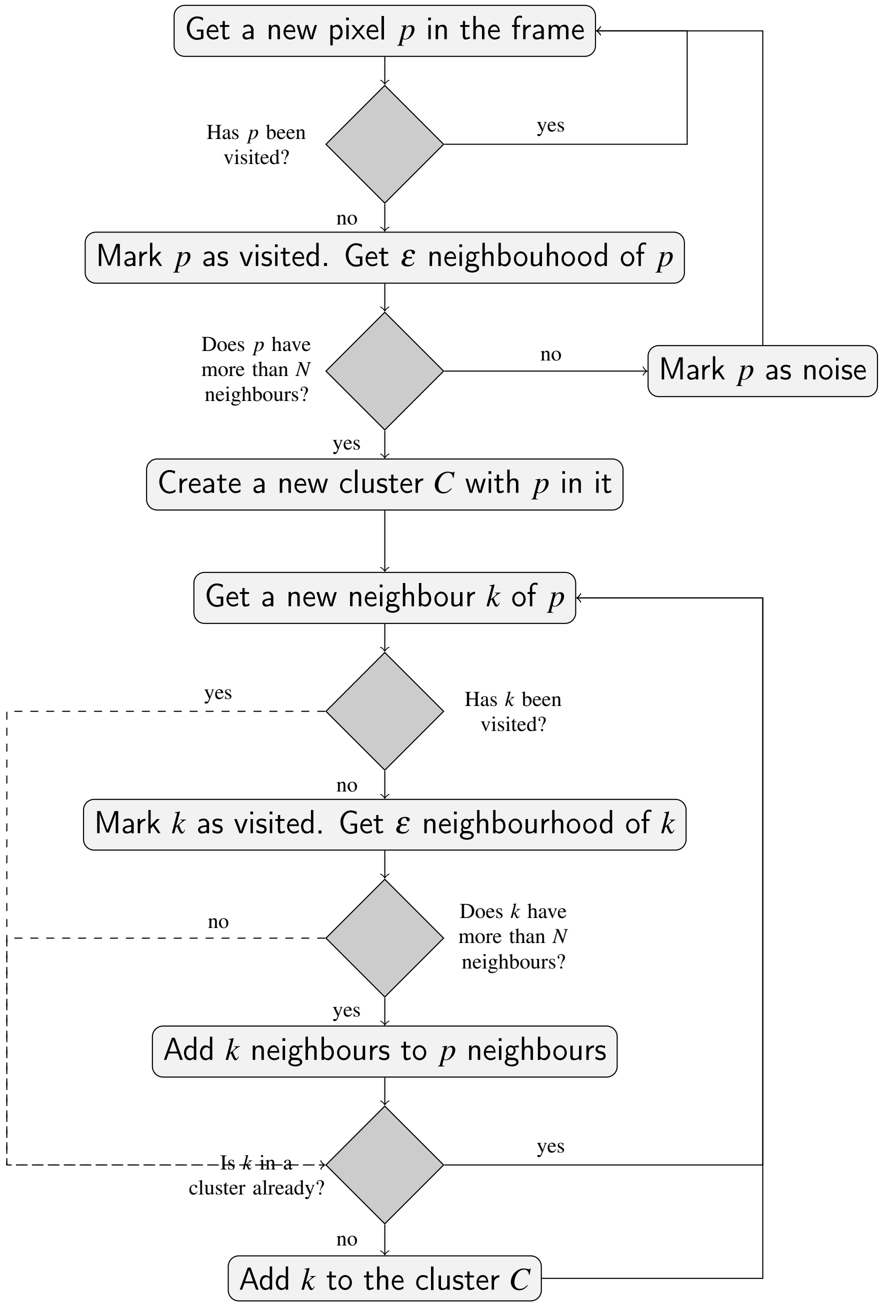

Fig. 5.4 Flow chart of the DBSCAN algorithm. The value of ε is the diagonal distance between the center of two pixels, and N is usually 1.

production, i.e., lattice excitations) around N, with a variance given by $\sigma^2 = fN$, where f is known as the Fano factor [62]. For silicon, it has the value of 0.115. Benoit and Hamel assume the initial charge distribution is parameterized by a spherically symmetric Gaussian function around the point of interaction. A quick glance to the α cluster shapes seems to confirm this (see, for example, figures 5.2 and 5.6). It seem pertinent to mention once again

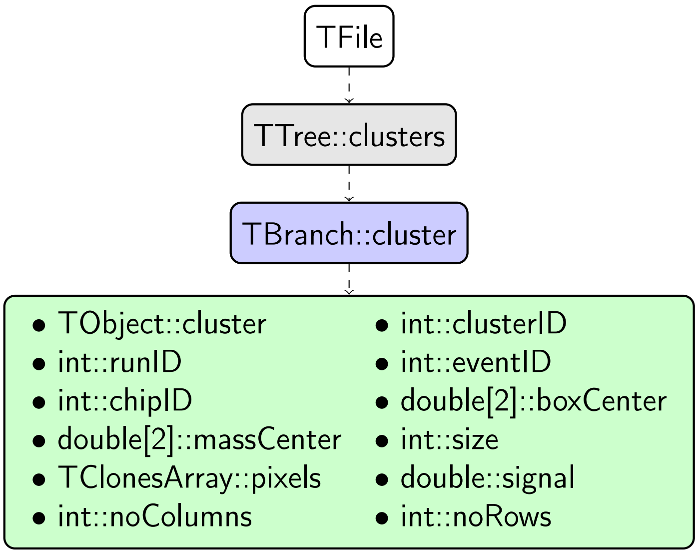

Fig. 5.5 Hierarchy of the output file produced after the clustering process. Each item in the green box represents a TLeaf object in ROOT. The class of the element, as well as its name, are shown.

that α particles deposit their energies in one single collision, on the surface of the detector. Therefore, there is no chance for charge diffusion to occur and the shape of an α cluster gives a good idea of how electron-hole pairs are distributed at the moment of the interaction. Figure 5.6 shows the signal components of two clusters obtained from Americium 241 —one of them an α cluster—.

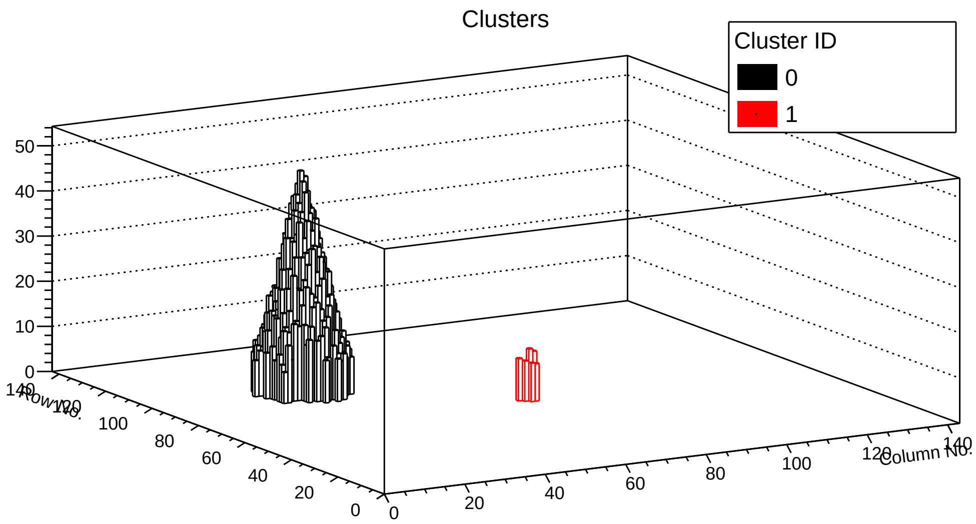

Fig. 5.6 Lego view of an α cluster obtained with the DBSCAN algorithm; the signal —in ADU— seems to follow a Gaussian distribution for the α cluster (black).

Benoit and Hamel also propose for the standard deviation of this gaussian distribution to be the electron practical range in the material (see [63], page S51)

$$\sigma(0) = AE\left(1 - \frac{B}{1+CE}\right). \tag{5.3}$$

For silicon, $A = 0.236$ cm·MeV^{-1}, $B = 0.98$ and $C = 0.003$ keV^{-1}. However, for a 4 MeV α particle this yields a σ of 8.7 mm; this is bigger than the dimensions of the XRPIX2b detector. Indeed, Benoit and Hamel simulated only photons, and their results seem to be relatively adequate for energies below 1 MeV. Kraphol simulates α and β particles, but fails to report the units used for the value of A. As figures 5.2 and 5.6 illustrate, the typical diameter for α clusters is around 20 pixels; hence, this diameter is also equal to 6σ. From this, the correct σ for alpha particles seems to be of the order of ~ 0.1 mm. We therefore establish a cut for A:

$$A = \begin{cases} 0.236 \text{ cm MeV}^{-1} & \text{for } E < 600 \text{ keV} \\ 0.0025 \text{ cm MeV}^{-1} & \text{for } E > 600 \text{ keV} \end{cases} \tag{5.4}$$

The three main charge transportation processes in a semiconductor are the drifting, diffusion and charge repulsion mechanisms. The first one is due to the applied electric field in the detector; though the charges in the material experience acceleration, they are scattered, stopped, and re-accelerated many times before reaching the terminals. This leads to the definition of a *drift velocity* $\mathbf{v}_{\text{drift}}$, which is the mean velocity the charge carriers have while traversing the detector

$$\mathbf{v}_{\text{drift}} = \mu\mathbf{E} \tag{5.5}$$

here, $\mathbf{E}$ is the applied electric field and μ is a quantity known as the mobility, that models the nonlinear dependence of the velocity to $\mathbf{E}$ and the temperature T. Jacoboni et al. have studied the charge transport properties of silicon [64], and propose the next expression for the mobility of electrons and holes in the material:

$$\mu = \frac{\mu_0}{\left[1 + \left(\frac{E}{E_c}\right)^{\beta}\right]^{1/\beta}} \tag{5.6}$$

with Diffusion is the result of the presence of a density gradient (in this case, a charge density). The change in charge density ρ with time is given by

$$\frac{\partial\rho}{\partial t} = D\nabla^2\rho \tag{5.7}$$

Parameter	Electrons	Holes	Units
μ_0	$-1.53 \times 10^9 \times T^{-2.42}$	$1.306 \times 10^8 \times T^{-2.2}$	$\mathrm{cm}^2\ \mathrm{V}^{-1}\ \mathrm{s}^{-1}$
E_c	$1.01 \times T^{1.55}$	$1.24 \times T^{1.68}$	$\mathrm{V\ cm}^{-1}$
β	$2.57 \times 10^{-2} \times T^{0.66}$	$0.46 \times T^{0.17}$	

Table 5.1 parameters for equation (5.6) in the case of Silicon. All the temperatures are measured in Kelvin. The minus sign of μ_0 for electrons assures that negative charged particles move in the opposite direction of field lines.

where D is known as the diffusivity. From the Einstein relation, for thermal equilibrium one obtains

$$D = \frac{\mu k_B T}{q} \tag{5.8}$$

where k_B is the Boltzmann constant, and q the charge of the diffusing particle. For a spherical Gaussian charge distribution, the solution of equation (5.7) is

$$\rho(r,t) = \frac{Q}{8\,(\pi D t)^{3/2}} \exp\left(-\frac{r^2}{4Dt}\right) \tag{5.9}$$

where Q is the total charge distributed. Assuming this charge Q is due to N particles of charge q (this is, $Q = qN$), one can divide equation (5.9) by Q and interpret the result as a probability density function for the position of one of the diffusing particles. Hence, the probability of finding a particle in the small range dr around r after a time Δt is given by

$$P(r,\Delta t)dr = \frac{1}{8\,(\pi D \Delta t)^{3/2}} \exp\left(-\frac{r^2}{4D\Delta t}\right) 4\pi r^2 dr. \tag{5.10}$$

and the probability of finding the particle at the vicinity dr of r after a time $k\Delta t$ is just

$$P(r,N\Delta t)dr = \frac{1}{8\,(\pi D k \Delta t)^{3/2}} \exp\left(-\frac{r^2}{4Dk\Delta t}\right) 4\pi r^2 dr.$$

It is easily shown (see, for example, [65]) that this is the same equation governing the position of a particle following a *random walk*, with a Gaussian step size of zero mean and variance equal to $2D\Delta t$ after taking k steps.

In order to account for the electric repulsion from the charge cloud that each charge carrier experiences, the diffusion equation (5.7) is modified with a term dependent of the electric field $\mathbf{E}_c$ created by this charge distribution:

$$\frac{\partial \rho}{\partial t} = D\nabla^2 \rho - \mu \nabla \cdot (\rho \mathbf{E}_c) \tag{5.11}$$

notice here that $\mathbf{E}_c$, the field created by the charge cloud, is different from $\mathbf{E}$, the field applied to the detector. In these simulations, following the previous works, we decouple the drifting from the diffusion-repulsion mechanism. As a first approximation, Benoit and Hamel assume that the spherically symmetric gaussian charge density approximation remains valid for times t different than zero. From this, as time advances, the size of the cloud increases. Mathematically, they state that the solution for equation (5.11) at any time t is

$$\rho(r,t) = \frac{Nq}{(2\pi\sigma^2(t))^{3/2}} \exp\left(-\frac{r^2}{2\sigma^2(t)}\right). \tag{5.12}$$

Replacing this and

$$\mathbf{E}_c(r,t) = \frac{1}{4\pi\varepsilon_0\varepsilon_r r^2} \int_0^r \rho(s,t) ds\, \hat{r}$$

(where ε_0 is the vacuum permittivity, and ε_r is the relative permittivity of the material, equal to 11.68 for silicon) in equation (5.11) a differential equation for $\sigma(t)$ is obtained:

$$\frac{\partial\sigma(t)}{\partial t} = \frac{1}{2\sigma(t)}\left(D + \frac{\mu Nq}{24\pi^{3/2}\varepsilon_0\varepsilon_r\sigma(t)}\right). \tag{5.13}$$

Repulsion is included in the simulation replacing the diffusivity D by

$$D_r(t) = D + \frac{\mu Nq}{24\pi^{3/2}\varepsilon_0\varepsilon_r\sigma(t)}. \tag{5.14}$$

With these ingredients, the proposed simulation process is as follows:

1. Obtain the deposited energy E and interaction coordinates $\mathbf{x}_i$ from Geant4.
2. Calculate the number N of electron-hole pairs generated, using a Gaussian distribution with mean $\mu = E/\varepsilon$ and variance equal to 0.115μ.
3. Since N can be extremely big, simulate n charge elements; each element with a charge of Nq/n, where q is the charge of the original carriers. Usually, a value of $n = 20$ is enough for β and γ rays. α rays may require for n to be larger than 1500.
4. Locate each electron-hole pair in the detector, following a Gaussian distribution with mean in $\mathbf{x}_i$ and σ given by equation (5.3).
5. Transport the charges for an interval Δt. Assuming the applied electric field is uniform throughout the detector, and it points in the z direction, transporting includes drifting, with $\Delta z = \mu E \Delta t$, and diffusion-repulsion, where Δx, Δy and Δz are random walk processes with a Gaussian step length of zero mean and variance equal to $2D_r t$, with

D_r given by equation (5.14). This requires solving equation (5.13) for each time interval, which is done numerically. A Step time of $\Delta t = 0.1$ ns is usually employed.

As the charges displace, they induce a current in the terminals, which is amplified and transformed in a pulse. Effectively, the charge collection does not happen when the charges reach the anodes, but it starts from the moment the charges begin to move. This is the celebrated result of Shockeley and Ramo [66, 67]. The amount of induced charge can be calculated by the means of the Shockeley-Ramo theorem: the induced charge in pixel p by one of the n charge carriers moving from position x_1 to position x_2 is given by the expression

$$Q_{\text{ind}} = \left(\frac{Nq}{n}\right)[\phi_p(x_1) - \phi_p(x_2)] \tag{5.15}$$

where $\phi_p(x)$ is known as the weighting potential for pixel p, and it corresponds to the electric potential that is obtained when this pixel is held at a potential of 1 volt, whereas the rest of the electrodes are grounded. A plot of the weighting potential for the XRPIX2b pixels is given in figure 5.7. Though the shape of the pixels is rectangular, we assume the weighting potential is symmetric around the z coordinate, and it only depends in the radial distance to the center of the cluster.

From here then, the next step in the simulation is:

6. After transporting the charges, obtain the new position $x(t + \Delta t)$, and calculate the induced charge using the weighting potential.

Notice that the shape of the weighting potential in figure 5.7 implies that charge elements moving below one pixel can induce a current in neighboring pixels as well. Hence, for the charge induction process, a 3×3 pixels grid was employed, and the charge induced by a charge element on pixel p and its eight neighbors was calculated. This process is repeated until all charges are collected, or until the integration time is reached (for simulation purposes, the integration time was taken to be 500 ns).

The first results are shown in figure 5.8. β and γ simulations appear to reproduce correctly the data obtained. However, though the geometrical properties of the real and the simulated clusters are similar, the charge distribution for simulated α clusters does not follow the true one. Effectively, Kraphol found the same results when performing his simulations; a possible explanation is that the initial charge distribution may deviate from a Gaussian one. Indeed, figure 5.9 shows the charge distribution in function of the distance to the cluster center for 56 α-like clusters with signals between 9000 and 11000 ADU, and 30 α-like clusters with signals between 13500 and 16500 ADU. These clusters were obtained from ^{241}Am, and the selection method was to demand from them to be bigger than 200 pixels, and to have an

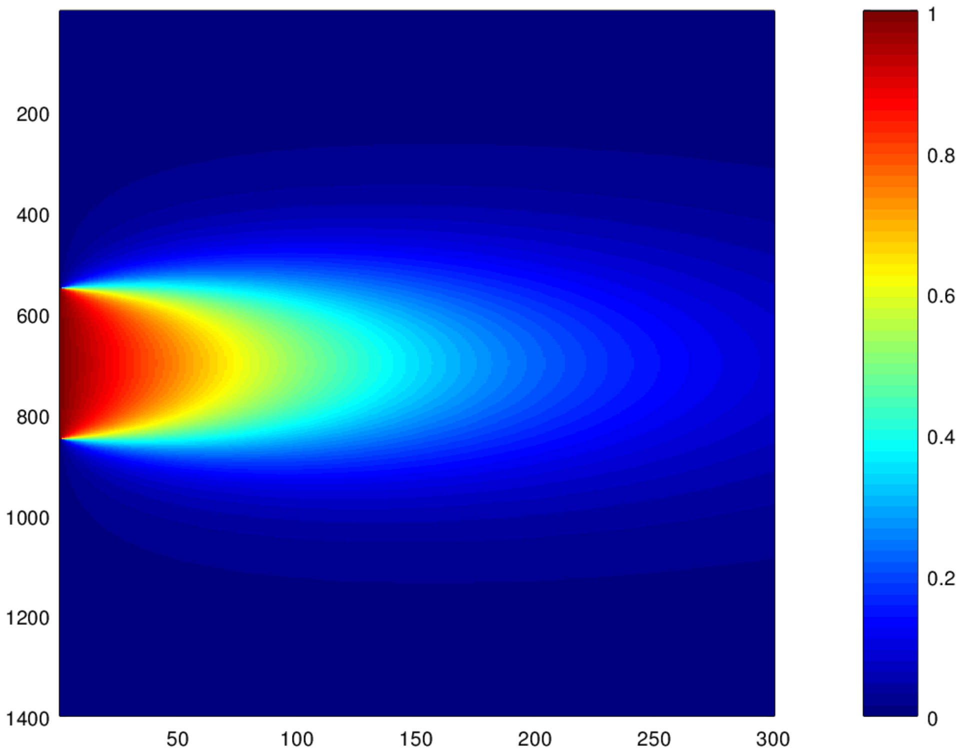

Fig. 5.7 Weighting potential for the XRPIX2b pixels; the pixel is centered at 700 μm, and extends from 550 μm to 850 μm. The marks in the x axis show the thickness of the silicon bulk, in μm.

occupation ratio larger than 0.65. Since α particles of different energies have different sizes, a comparison is only valid when the cluster energies are similar. Hence, only clusters whose total signal differ in less than 10% are grouped together. This is, clusters with signals E such that

$$E \in [0.9E_0, 1.1E_0]$$

for a specific value E_0.

The best Gaussian fit with $\mu = 0$ for both cases is also shown; as it can be appreciated, the Gaussian assumption is indeed correct; however, it somehow underestimates the charge amount for pixels near the center, and in the tail of the distribution. Moreover, the best fit gives for the histogram in the left a σ of 3.82855 ± 0.02923, whereas the one in the right has a σ of 3.0709 ± 0.02516. However, from equation (5.3), the value of σ for the second histogram should be bigger, since the energy deposited is larger.

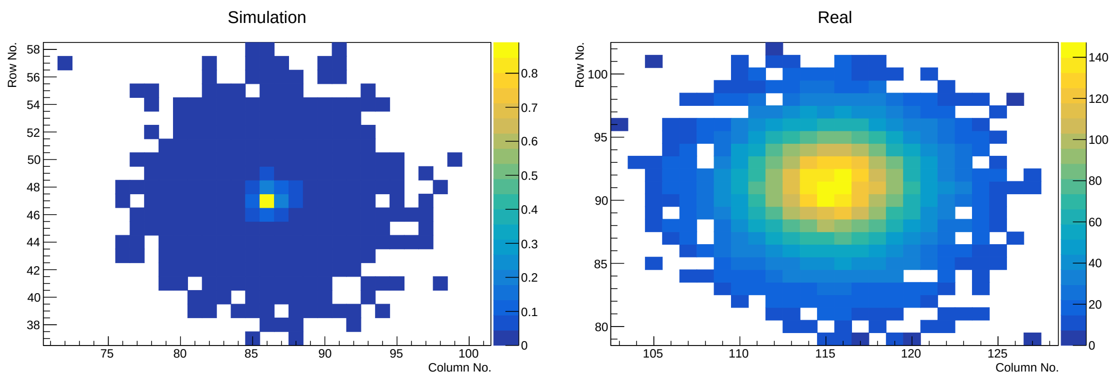

(a) α clusters

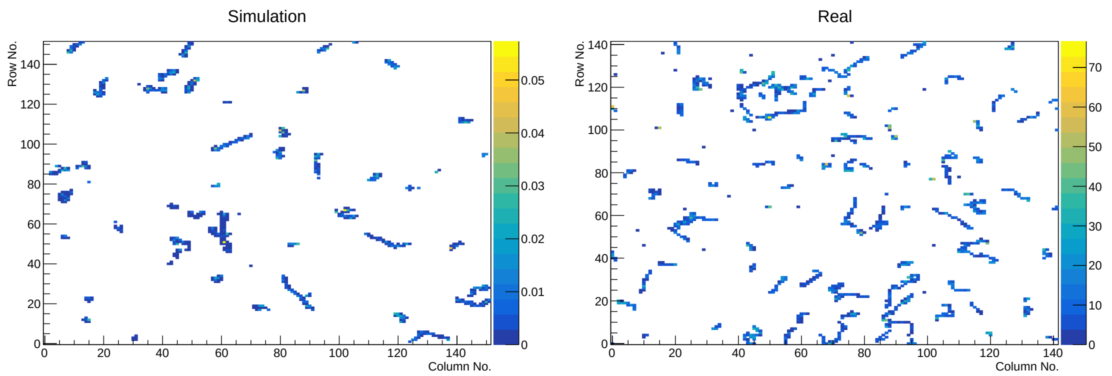

(b) β clusters

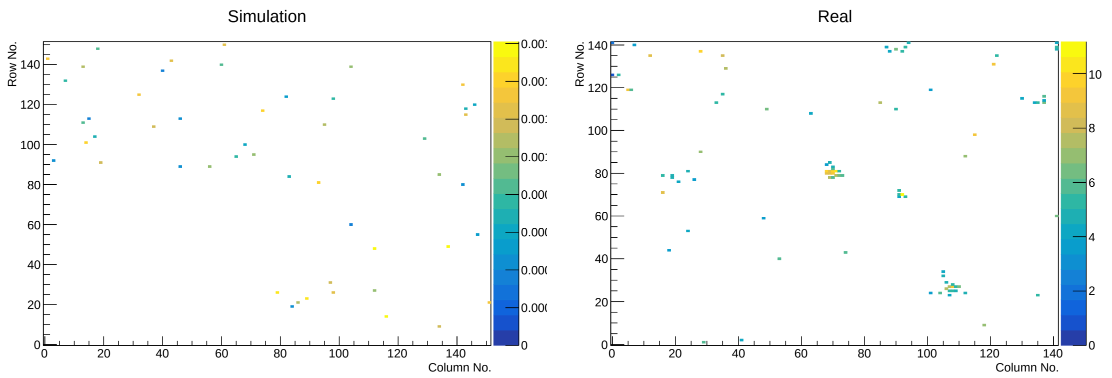

(c) γ clusters

Fig. 5.8 Simulated (left) and real (right) events. In *(a)*, the real event corresponds to an alpha particle emitted by Am-241; the simulated one is an alpha particle with energy of 6 MeV. In *(b)*, both the simulated and the real data correspond to beta rays from Sr-90. Finally, in *(c)*, the simulated data comes from an uniform source of photons with energies from 0.1 keV to 500 keV; the real is, again, Am-241. The bigger clusters for the real data in *(c)* are due to photons with energies bigger than 1 MeV.

A study on alpha clusters performed by M. Campbell et al [68] revealed that the assumption 5.3 is not adequate for an α-cluster, since given the high number of electron-hole pairs produced by the alpha particle, plasma and funnelling effects take place.

Luckily, this setback seems to have no effect on the β and γ simulations; this is due to the fact that the energies deposited in a single hit by these two kind of particles are rather

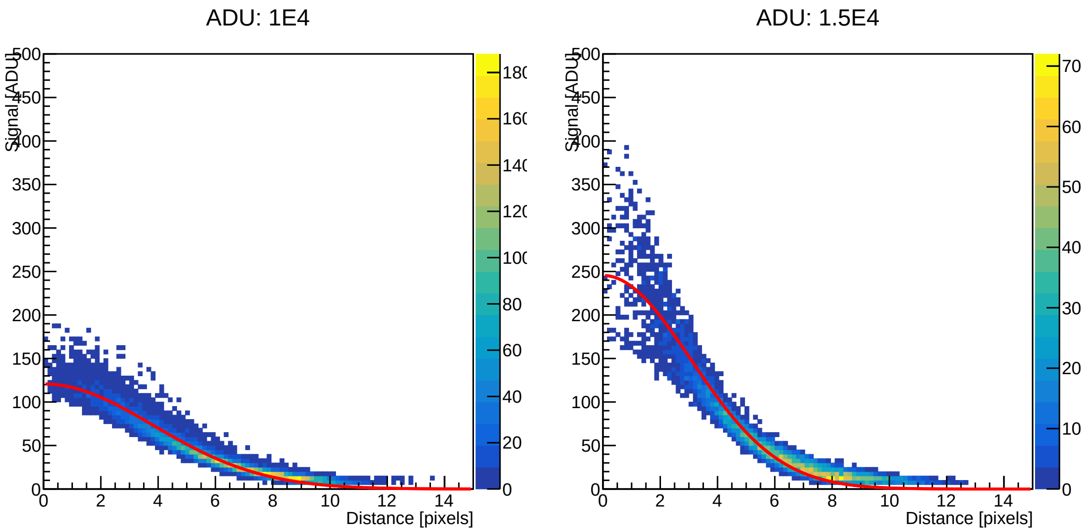

Fig. 5.9 In the left: pixel signal (in ADU) as a function of the distance to the center of the cluster for α-like clusters with a total signal of $(1 \pm 0.1) \times 10^4$ ADU. *In the right:* the same, for α-like clusters with a total signal of $(1.5 \pm 0.15) \times 10^4$ ADU. Notice that the σ of the right distribution does not increase in comparison with the left one, in contradiction with equation (5.3).

low, leading to a value of $\sigma(0)$ which is usually smaller than the dimensions of a single pixel. Hence, the initial charge distribution for β and γ clusters does not matter for the current granularity of the detector. Furthermore, the identification of α clusters can be done using the size and occupation ratio of the cluster, whose values are independent of the charge distribution inside the cluster. We therefore regard the matter of the correct expression for the initial charge distribution to another job.

Since most of the γ clusters are single pixels, and the production of simulated α clusters data is computationally expensive, the exactitude of the simulations was tested by comparing the simulated β clusters obtained for a ^{90}Sr source against some real measurements performed. The relevant histograms on total energy, cluster size, cluster and box centers' distance, difference between the number of columns and the number of rows spanned by the cluster, and the occupied fraction of the cluster are shown in figure 5.10. Though the correspondence between the two data sets gets lower as the energy increases, the fit is rather good for energies below 30 keV. We attribute the differences to the data size for both files (the simulation corresponds to 10^4 frames, with one electron penetrating the sensitive volume in each one; the real data corresponds to 5×10^5 frames, with multiple events per frame) and to the absence of a preamplifier circuit model in the simulation; also, the preprocessing condition for real events (equation 5.1) effectively reduces the size of the clusters, which is reflected in the discrepancies seen in the histograms.

Once the simulations are validated, we proceed to study the case of β and γ clusters with energies below 0.3 MeV. The original energy spectra for electrons and photons is uniform,

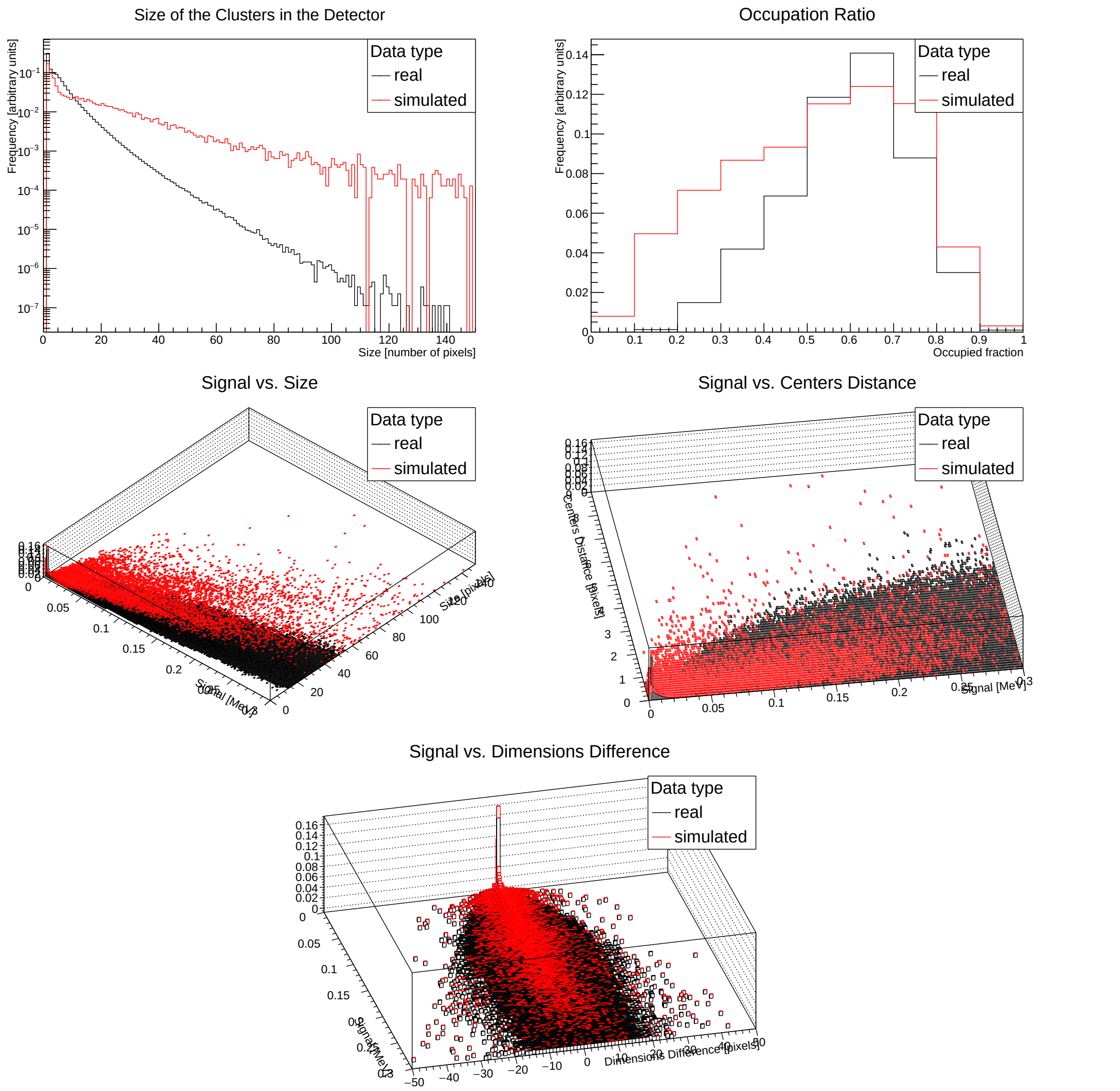

Fig. 5.10 Simulations (red) versus real data (black) of β clusters for Stronium-90. From left to right and top to bottom: size of the clusters in the detector; occupation ratio of the clusters; size in function of the signal; distance between the bounding box center and the cluster center in function of the signal; and occupation ratio in function of the signal. All histograms are normalized to their respective number of entries.

and they were fired from random positions and in random directions; both simulations contain roughly 10^4 clusters. The results are shown in figure 5.11. Electrons tend to deposit larger amounts of energy, and to leave bigger tracks. Of special relevance are the histograms on the left side, which show the cluster parameters for clusters with energies below 15 keV. It is easily seen that the physical properties of the clusters cannot be used to completely differentiate between β and γ radiation, which reinforces the statement made at the beginning of this chapter: low energy electrons and photons tend to have very similar signals. There are still some cases when the distinction can be clearly made: a cluster with an occupation ratio smaller than 0.5 is definitely a β one; the same for clusters in which the number of rows and columns differ by more than 4. These long, low energetic β clusters are likely to be produced by electrons with energies above 30 keV that escape the sensitive region before depositing all their energy.

It rests to be seen if an improvement of the simulations leads to different results. The implementation of a preamplifier and the introduction of noise cutoffs seem to be the first things to try. Effectively, the fact that the difference between the number of rows and the number of columns is pretty similar for the simulation and the real data, whereas the size of the clusters is bigger for the simulations, suggests that both the number of rows and the number of columns increase by the same amount; this effect can be attributed to charge diffusion, and it should be attenuated by imposing a threshold on the pixels' signals. The consequences of charge diffusion can also be appreciated in the distance between the bounding box and the cluster centers: for small sizes, the simulated distance is bigger than the real one, which can be explained by the charge diffusion increasing the box size, but not displacing the center of the cluster.

It seems convenient to study the signal shape produced by different particles in the detector: since the main difference between low energy electrons and photons is the number of interactions both undergo before loosing all their energy, the number of electron-hole showers and the total charge a single shower induces is likely to differ among different types of radiation.

From these results we conclude that there is not mechanism —at least at hand— to fully reject β background at low energies. Moreover, from the analysis done in chapter 4, external β radiation is very unlikely to penetrate through the shielding materials; hence, the radioactivity from the detector components is probably the most important source for this kind of signal. Measurements on this topic are already being performed; the results obtained so far are shown in appendix A.

Once the rate of electrons produced by internal radioactivity is determined, it is necessary to estimate the fraction of these electrons that generates γ-like clusters; this requires the implementation of a more detailed simulation.

5.3 First Background Data Taken With the XRPIX

We conclude this chapter with a brief analysis of the first background measurements performed with the XRPIX detector. This data corresponds to 32.5 hours of exposure, inside the thermal chamber. No shields, besides the walls of the thermal chamber, were implemented. The temperature was set to 223.15 K (-50 °C) in order to reduce the thermal noise.

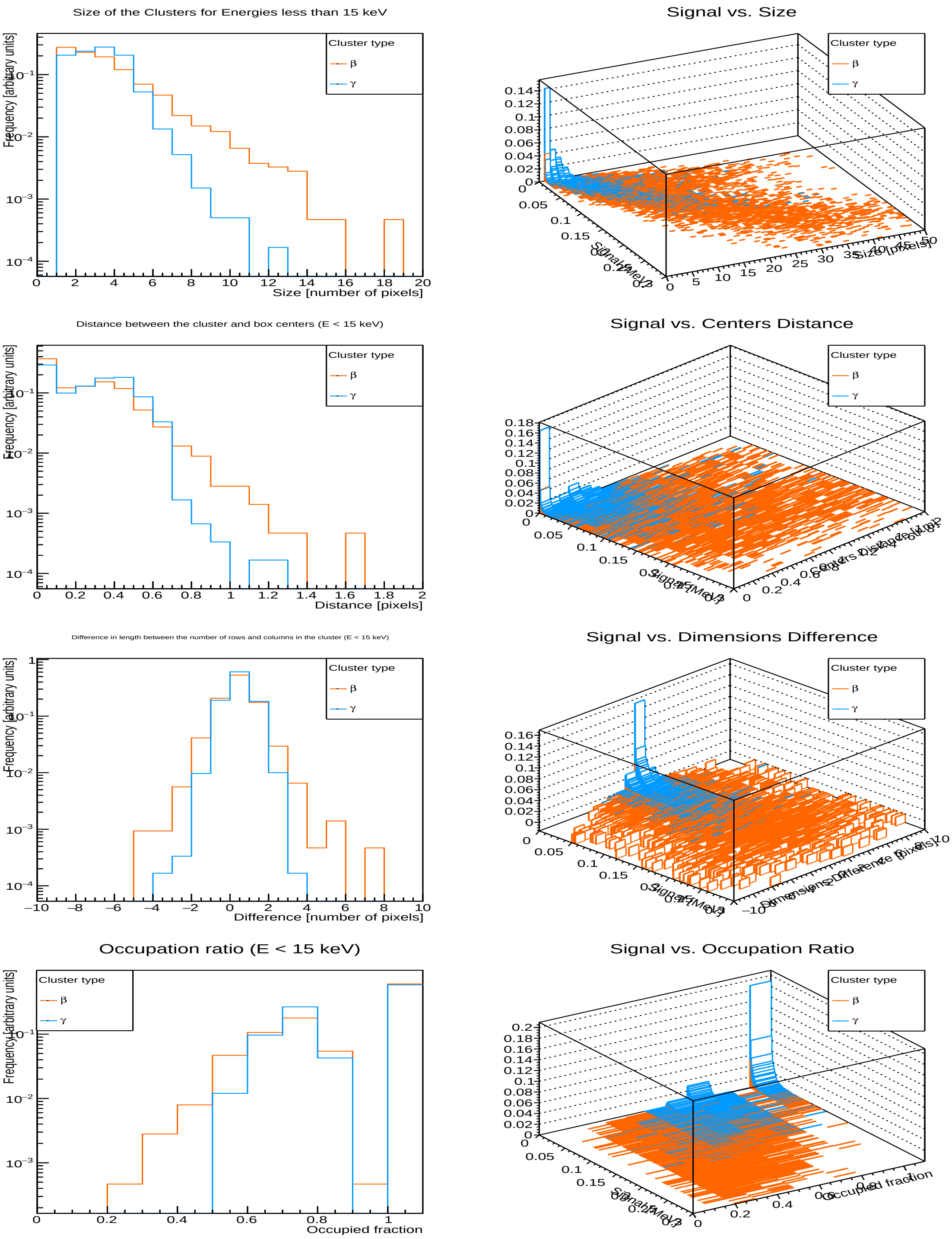

Fig. 5.11 Simulations of β (orange) and γ (blue) clusters with uniform energies between 0 - 0.3 MeV. Each histogram on the left represents the values for clusters with energies under 15 keV. From top to bottom: energy deposited vs. size of the cluster; energy deposited vs. distance between the bound box and the cluster centers; energy deposited vs. difference between the number of rows and columns of the cluster; energy vs. fraction of the bounding box occupied by the cluster. All histograms are normalized to their own number of entries.

We present the spectrum obtained in figure 5.12, together with its most prominent peaks. Recalling from the previous chapter, we see that the events rate for energies between 0.5 keV and 5 keV is still very high, even though the thermal noise is expected to dimish; the histogram integral gives a total of $6.717 \times 10^7 \pm 8.195 \times 10^3$ events. This reinforces the conclusion of the non-viability of a WIMP search at this stage. On the other hand, the number of events in the 14.4 ± 1.3 keV range was 60, for the whole 32.5 hours.

The most prominent peak can be due to back scattering of an unknown γ source. If that is the case, using the expression for the energy transferred by a back-scattered photon:

$$E' = E_0 \left(1 - \frac{1}{1 + \frac{2E_0}{0.511\ \mathrm{MeV}}} \right) \tag{5.16}$$

with E_0 the initial energy of the photon, we can solve for the energy of the original γ source; it would have an energy of 294.89 keV. The source of this peak is currently under study.

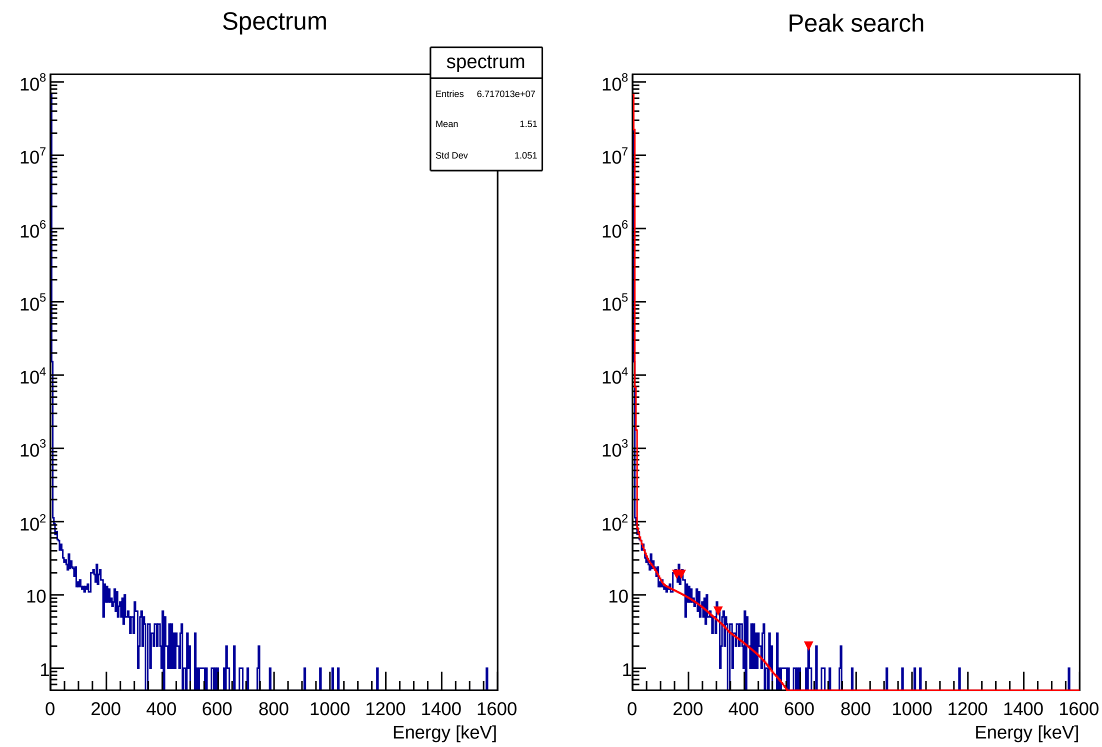

Fig. 5.12 Energy spectrum for the first background data in the thermal chamber. The peaks are located at: 158 keV, 174 keV, 306 keV and 630 keV.

Analyzing the cluster sizes, two clusters with more than 150 pixels (155 and 187 pixels) were found. These are shown in figure 5.13. The biggest one corresponds to two beta clusters emitted from the same point (probably a pair production process), whereas the next one corresponds to a cosmic ray and an associated δ electron. The rest of the events with sizes bigger than 100 pixels (10 in total) where identified with β rays.

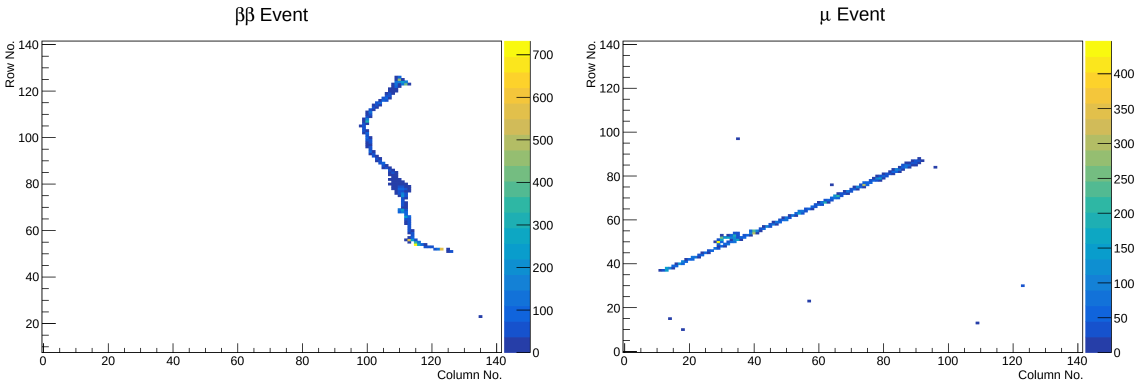

Fig. 5.13 Two β event (left) and a cosmic muon event (right).

Since β and γ particles can be produced by multiple means, when looking for radioactive contamination is useful to search for α clusters. Though at first it seems like there are no α decays in the data obtained (from the cluster size results), events in the border of the detector have different properties; in this case, we require for the occupation ratio to be higher than 0.75, for the size of the cluster to be higher than 15, and for its center to be near the border of the detector (within 2 pixels). With this, 6 candidates appeared, shown in figure 5.14.

There seems to be a cluster with the adequate spatial extension and shape to be an α candidate. The energy deposited is 56.593 keV, which is at least eight times smaller than an usual α energy. It is quite likely that this particle deposited most of its energy in the non-sensitive region of the detector at the borders of the chip.

This partially illustrates the use that can be made of the clustering framework. In order to conduct a spectral analysis using the cluster shapes, however, it is necessary to accumulate more statistics. Also, in order to study the internal background sources, the external sources should be made as negligible as possible; it is compulsory then to test the validity of the conclusions done in chapter 4 by implementing a simple setup, and then to proceed to measure the background spectrum under the lead and copper shields, inside the thermal chamber.

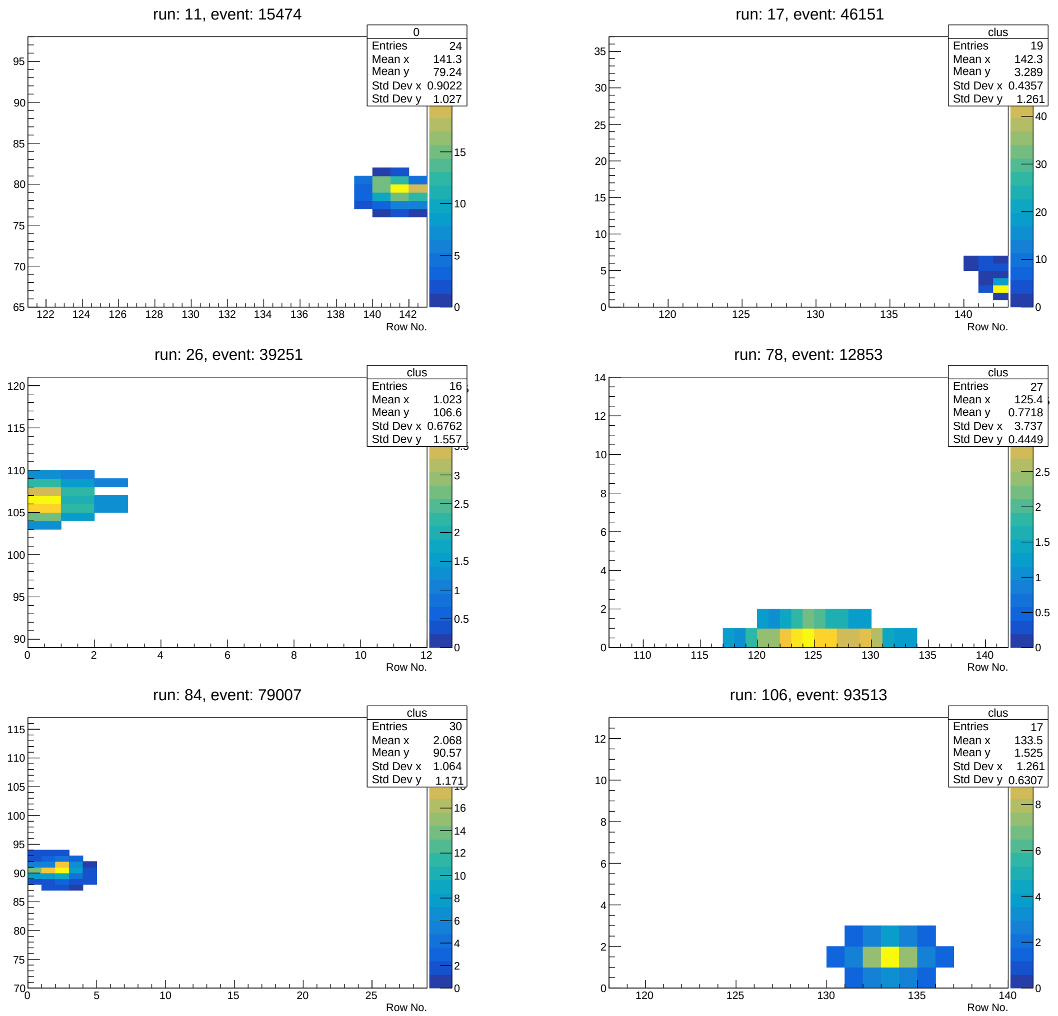

Fig. 5.14 Clusters in the border with a significant number of pixels. From this images, the cluster at run 78, event 12853 looks like and α particle. The enegies for each cluster are, from left to right and from top to bottom: 176.860 keV, 234.754 keV, 33.934 keV, 56.593 keV, 165.816 keV and 57.278 keV.

Chapter 6

Conclusions and Future Prospects

This concludes the analysis of this work. As seen in chapter 4, one of the main external background sources are γ rays produced in the rear of the lead shields by the interaction of cosmic muons with the shield material, and by radioactive decays outside the shields. It is expected for the introduction of a VETO scintillator to reduce the background to a level comparable to the current benchmark set by Derbin *et al* [19]. A thicker copper shield, though desirable, seems not necesary if one haves in mind that the measurements shown in chapter 4 were done outside the thermostatic chamber, and that the chamber effectively acts as an extra shielding layer; moreover, the thermal noise is also reduced. As a final note, it was suggested to perform a similar analysis with longer times, using the XRPIX detector; the radioactivity of the detector components seems to have the biggest impact in the background rate (according to the value of K_o), so this aspect must also be evaluated. These studies are being conducted now. As a final remark, table 6.1 presents the comparison with former experiments and the current one; the energy resolution and the background levels are promising in order to obtain a new, more stringent constraint.

In chapter 5 we showed the limitations that the original analysis framework for the event mode in the XRPIX had, and developed a new one, able to extend the applicability of the detector to other kind of particles different from photons. We used this clustering

Experiment:	**Namba (2007)**	**Derbin (2011)**	**Current**
Background $[\times 10^{-3}/(\text{mm}^2\ \text{h keV})]$	1.76	1.09	< 1.23
Energy resolution at 14.4 keV [keV]	2.36	1.48	0.58^{*}
Temperature [K]	205	77.35	223.15

Table 6.1 Comparison between former and current experiments searching for Axions using ^{57}Fe.

framework to study the signal properties different kind of particles had, hoping that, as in higher energy ranges, the clusters' physical properties were enough to distinguish among different kinds of radiation; in doing so, we developed a simulation of the physical response of the detector, which aimed to reproduce the cluster shapes left by different types of particles. The conclusion was that β and γ events of the same energy are clearly distinguishable for energies above 100 keV, but for energies below this threshold they can only be partially differentiated from their cluster shapes. A detailed study of the background sources inside the detector (since external beta radiation is safely rejected by the shielding materials, as shown in chapter 4) is needed, as well as an analysis of the frequency of γ-like β-clusters occurrency for the energies of interest; this last study can only be done by the means of simulated data, so a more precise and faster simulation model must be developed.

Finally, we used this new framework to analyze the first group of background data taken with the XRXPIX2b chip. These results reinforce the conclusion that a WIMP search is non-viable at the current stage, given the high rate of background events; it also allowed us to calculate a first background rate for the XRPIX detector in the region of 14.4 ± 1.3 keV. The events rate was calculated to be 0.08725 h^{-1} mm^{-2} keV^{-1}, which is only 5.3 times bigger than the background obtained for the 6Cu configuration; this seems to indicate that the internal background soruces in the XRPIX detector are indeed lower than in the CdTe one, and offer further evidence that the background rate calculated in this work and shown in table 6.1 is actually smaller. The presence of α and β like clusters was shown; however, the amount of data currently available is not enough to perform a search for decay chains traces, which would help to determine the nature of the radioactive sources present in the experiment.

From now on, more background data will be accumulated. Once the XRPIX5b gets delivered, a first run of the whole experimental setup will be performed, using two stacks of XRPIX5b detectors; without ^{57}Fe foils, these measurements would help to estimate the background level and to identify its sources, in the presence of lead and copper shields. In the mean time, a more detailed simulation of the cluster generation process is to be developed, taking into account the electronics of the preamplifier, as well as a more realistic model of the charge distribution, transport and collection processes. The clustering algorithm is also expected to be modified to include more clustering properties (border size, maximum distance inside the cluster, endpoints' positions) and to identify, when possible, the kind of particle to which the cluster belongs.

References

[1] R. Peccei, “The Strong CP Problem, Axions,” *Lecture Notes on Physics*, 2008.

[2] R. Peccei, “Discrete, Global Symmetries in Particles Physics,” in *Lecture Notes on Physics*, 1999.

[3] D. V. S. Michael E. Peskin, *An Introduction to Quantum Field Theory*. Westview Press, 1995.

[4] C.G. Callan, R.F. Dashen, D.J. Gross, “The Structure of the Gauge Theory Vacuum,” *Physics Letters B*, vol. 63, pp. 334–340, August 1976.

[5] V. Baluni, “CP-nonconserving effects in quantum chromodynamics,” *Physical Review D*, vol. 19, pp. 2227–2230, April 1979.

[6] R.J. Crewther, P. Di Vecchia, G. Veneziano, E. Witten, “Chiral Estimate of the Electric Dipole Moment of the Neutron in Quantum Chromodynamics,” *Physics Letters B*, vol. 88, pp. 123–1237, December 1979.

[7] S. Narison, “A Fresh Look into the Neutron EDM, Magnetic Susceptibility,” *Physics Letters B*, vol. 666, pp. 455–461, September 2008.

[8] G. Schierholz, “Towards a Dynamical Solution of the Strong CP Problem,” *Nuclear Physics B*, vol. 37, pp. 203–210, August 1993.

[9] R.D. Peccei, Helen R. Quinn, “CP Conservation in the Presence of Pseudoparticles,” *Physical Review Letters*, vol. 38, pp. 1440–1443, June 1977.

[10] William A. Bardeen, R.D. Peccei, T. Yanagida, “Constraints on Variant Axion Models,” *Nuclear Physics B*, vol. 279, pp. 401–428, January 1987.

[11] A. Ringwald, L.J. Rosenberg, G. Rybka, “Axions, Other Similar Particles,” in *Hypothetical Particles, Concepts*, 2016.

[12] P. Sikivie, “Experimental Tests of the "Invisible" Action,” *Physical Review Letters*, vol. 51, pp. 1415–1417, October 1983.

[13] Y. Inoue, Y. Akimoto, R. Ohta, T. Mizumoto, A. Yamamoto, M. Minowa, “Search of solar axions with mass around 1 eV using coherent conversion of axions into photons,” *Physics Letters B*, vol. 668, pp. 93–97, October 2008.

[14] M. Arik (et al), “New solar axion search using the CERN Axion Solar Telescope with ^{4}He filling,” *Physical Review D*, vol. 92, July 2015.

[15] S. Moriyama, "Proposal to Search for a Monochromatic Component of Solar Axions Using ^{57}Fe," *Physical Review Letters*, vol. 75, pp. 3222–3225, October 1995.

[16] M. Srednicki, "Axion couplings to matter," *Nuclear Physics B*, vol. 260, April 1985.

[17] W.C. Haxton, K.Y. Lee, "Red-Giant Evolution, Metallicity, New Bounds on Hadronic Axions," *Physical Review Letters*, vol. 66, pp. 2557–2560, May 1991.

[18] T. Namba, "Results of a search for monochromatic solar axions using ^{57}Fe," *Physics Letters B*, vol. 645, January 2007.

[19] A.V. Derbin, V.N. Muratova, D.A. Semenov, E.V. Unzhakov, "New limit on the mass of 14.4-keV solar axions emitted in an M1 transition in ^{57}Fe nuclei," *Physics of Atomic Nuclei*, vol. 74, pp. 596–602, April 2011.

[20] F. Zwicky, "On the Masses of Nebulae, of Clusters of Nebulae," *The Astrophysical Journal*, vol. 86, pp. 217–246, October 1937.

[21] J. Oort, "The force exerted by the stellar system in the direction perpendicular to the galactic plane, some related problems," *Bulletin of the Astronomical Institutes of the Netherlands*, vol. 6, pp. 249–287, August 1932.

[22] M. Milgrom, "A modification of the Newtonian dynamics as a possible alternative to the hidden mass hypothesis," *The Astrophysical Journal*, vol. 270, pp. 365–370, July 1983.

[23] J.R. Brownstein, J.W. Moffat, "Galaxy cluster masses without non-baryonic dark matter," *Monthly Notices of the Royal Astronomical Society*, vol. 367, pp. 527–540, April 2006.

[24] D. Clowe, M. Bradac, A.H. Gonzalez, M. Markevitch, S.W. Randall, C. Jones, D. Zaritsky, "A direct empirical proof of the existence of dark matter," *The Astrophysical Journal Letters*, vol. 648, August 2006.

[25] P. Dress, G. Gerbier, "Dark Matter," in *Astrophysics, Cosmology*, 2015.

[26] O. Lahav, A.R. Liddle, "The Cosmological Parameters," in *Astrophysics, Cosmology*, 2015.

[27] The AMS Collaboration, "Precision Measurement of the $(e^+ + e^-)$ Flux in Primary Cosmic Rays from 0.5 GeV to 1 TeV with the Alpha Magnetic Spectrometer on the Internatiotal Space Station," *Physical Review Letters*, vol. 113, November 2014.

[28] The AMS Collaboration, "Precision Measurement of the Proton Flux in Primary Cosmic Rays from Rigidity 1 GV to 1.8 TV with the Alpha Magnetic Spectrometer on the International Space Station," *Physical Review Letters*, vol. 114, May 2015.

[29] The AMS Collaboration, "Precision Measurement of the Helium Flux in Primary Cosmic Rays of Rigidities 1.9 GV to 3 TV with the Alpha Magnetic Spectrometer on the International Space Station," *Physical Review Letters*, vol. 115, November 2015.

[30] L.A. Cavasonza, H. Gast, M. Kramer, M. Pellen, S. Schael, "Constraints on leptophilic dark matter from AMS-02 experiment," *The Astrophysical Journal*, vol. 839, May 2017.

[31] J. Tiffenberg (et al), “DAMIC: a novel dark matter experiment,” in *Proceedings, 33rd International Cosmic Ray Conference (ICRC2013): Rio de Janeiro, Brazil, July 2-9, 2013*, p. 1243, 2013.

[32] C. E. Aalseth (et al), “CoGeNT: A Search for Low-Mass Dark Matter using p-type Point Contact Germanium Detectors,” *Physical Review D*, vol. 88, 2013.

[33] R. Bernabei (et al), “DAMA/LIBRA results, perspectives,” in *RICAP16, 6th Roma International Conference on Astroparticle Physics*, 2017.

[34] M. Yamashita, “Direct Dark Matter Search with XMASS-I,” in *The 12th Conference on the Intersections of Particle, Nuclear Physics in Vail, CO, U.S.A.*, 2015.

[35] J.D. Lewin, P.F. Smith, “Review of mathematics, numerical factors,, corrections for dark matter experiments based on elastic nuclear recoil,” *Astroparticle Physics*, vol. 6, June 1996.

[36] L. Baudis, “Dark matter searches,” *Annalen der Physik*, vol. 528, September 2015.

[37] E. Aprile (et al), “First Dark Matter Search Results from the XENON1T Experiment,” May 2017.

[38] A. Takeda (et al), “Design, Evaluation of an SOI Pixel Sensor for Trigger-Driven X-Ray Readout,” *IEEE Transactions on Nuclear Science*, vol. 60, April 2013.

[39] A. Takeda (et al), “First Performance Evaluation of an X-Ray SOI Pixel Sensor for Imaging Spectroscopy, Intra-Pixel Trigger,” *IEEE Transactions on Nuclear Science*, vol. 58, October 2011.

[40] O. Brass, “C10200 (ASTM B152) Oxygen Free Copper Alloy Data Specifications.” Online.

[41] International Atomic Energy Agency, *Generic procedures for assessment, response during a radiological emergency*, August 2000.

[42] A. Suzuki, T. Iida, J. Moriizumi, Y. Sakuma, “The Effects of Different Types of Concrete on Population Doses,” *Radiation Protection Dosimetry*, vol. 90, March 2000.

[43] S. Tavernier, *Experimental Techniques in Nuclear, Particle Physics*. Springer, 2010.

[44] M.J. Berger, J.S. Coursey, M.A. Zucker, J. Chang, “Stopping-Power & Range Tables for Electrons, Protons and Helium Ions,” June 2017.

[45] H. Bichsel, D.E. Groom, S.R. Klein, “Passage of particles through matter,” in *Experimental Methods, Colliders*, 2012.

[46] J.H. Hubbell, S.M. Seltzer, “Tables of X-Ray Mass Attenuation Coefficients, Mass Energy-Absorption Coefficients from 1keV to 20 MeV for Elements Z=1 to 92, 48 Additional Substances of Dosimetric Interest,” June 2017.

[47] X. Mougeot, R.G. Helmer, “K-40,” in *Mini-table of radionuclides*, 2009.

[48] J. Beatty, J. Matthews, S.P. Wakely, “Cosmic Rays,” in *Astrophysics, Cosmology*, 2015.

[49] C. Hagmann, D. Lange, J. Verbeke, D. Wright, "Monte Carlo Simulation of Proton-induced Cosmic-ray Cascades in the Atmosphere." Distributed with the CRY package, February 2012.

[50] C. Hagmann, D. Lange, J. Verbeke, D. Wright, *Cosmic-ray Shower Library (CRY)*. Lawrence Livermore National Laboratory, March 2012.

[51] D.E. Groom, N.V. Mokhov, S.I. Striganov, "Muon Stopping Power, Range Tables 10 MeV – 100 TeV," *Atomic Data, Nuclear data Tables*, vol. 76, July 2001.

[52] Clear-Pulse, "CdTe Detector Integrated Low Noise Preamplifier Model 579/CdTe." Online.

[53] A.V. Derbin, V.N. Muratova, D.A. Semenov, E.V. Unzhakov, "New Limit on the Mass of 14.4-keV Solar Axions Emitted in a $M1$ Transition in ^{57}Fe Nuclei," *Physics of Atomic Nuclei*, vol. 74, no. 4, 2011.

[54] S. Agostinelli (et al), "GEANT4–a simulation toolkit," *Nuclear Instruments and Methods in Physics Research A*, vol. 506, July 2003.

[55] J.R.T. de Mello Neto, "The DAMIC dark matter experiment," in *34th International Cosmic Ray Conference, The Hague, The Netherlands*, 2015.

[56] T. Holy (et al), "Pattern recognition of tracks induced by individual quanta of ionizing radiation in Medipix2 silicon detector," *Nuclear Instruments, Methods in Physics Research A*, vol. 591, June 2008.

[57] A. Aguilar-Arevalo (et al), "Measurement of radioactive contamination in the high-resistivity silicon CCDs of the DAMIC experiment," *JINST*, vol. 10, June 2016.

[58] M. Ester, H.P. Kriegel, J. Sander, X. Xu, "A Density-Based Algorithm for Discovering Clusters in Large Spatial Databases with Noise," in *2nd International Conference on Knowledge Discovery, Data Mining*, 1996.

[59] R. Brun, F. Rademakers, "ROOT - An object oriented data analysis framework," *Nuclear Instruments & Methods in Physics Research A*, vol. 389, April 1997.

[60] M. Benoit, L.A. Hamel, "Simulation of charge collection processes in semiconductor CdZnTe γ-ray detectors," *Nuclear Instruments, Methods in Physics Research A*, vol. 606, July 2009.

[61] D. Krapohl, *Monte Carlo, Charge Transport Simulation of Pixel Detector Systems*. PhD thesis, Mid Sweden University, March 2015.

[62] U. Fano, "Ionization Yield of Radiations, II. The Fluctuation of the Number of Ions," *Physical Review*, vol. 72, July 1947.

[63] C. Wohl (et al), "Review of Particle Properties," *Review of Modern Physics*, vol. 56, April 1984.

[64] C. Jacaboni, C. Canali, G. Ottaviani, A. Alberigi Quaranta, "A review of some charge transport properties of Silicon," *Solid-State Electronics*, vol. 20, February 1977.

[65] A. F. Ghoniem, “Grid-free Simulation of Diffusion Using Random Walk Methods,” *Journal of Computational Physics*, vol. 61, October 1985.

[66] W. Shockeley, “Currents to Conductors Induced by a Moving Point Charge,” *Journal of Applied Physics 9*, vol. 635, 1938.

[67] S. Ramo, “Currents Induced by Electron Motion,” *Procedings of the IRE*, vol. 27, September 1939.

[68] M. Campbell *et al.*, “Study of the charge sharing in a silicon pixel detector by means of α-particles interacting with a Medipix2 device,” *Nuclear Instruments and Methods in Physics Research A*, vol. 591, pp. 38–41, June 2008.

Appendix A

Radioactivity of the detector components

The next table lists the components included in the XRPIX chip board and if, measured, the activity generated by ^{238}U contamination.

Components of the XRPIX Chip Board				
QTY	**Catalog**	**Manufacturer**	**Category**	**Activity [mBq/unit]**
1	SM17-029	Shiima Elec.	PCB	
2	FH28D-74S-0.5SH	Hirose	Conector	1.6 ± 0.1
1	INA103KU	TI	Instr. amp.	0.25 ± 0.16
1	PVG5H103C03R0O	Boums	Potentiometer	0.22 ± 0.24
2	BLM21BB4715N1D	Murata	Ferrite beads	0.011 ± 0.006
4	NFM18PS105R0J3D	Murata	EMI filter	0.096 ± 0.011
1	GRM31CR72H473KW09	Murata	Capacitor	
6	CL32A107MPVNNNE	Samsung	Capacitor	4.67 ± 0.09
19	GRM188B11E104KA01D	Murata	Capacitor	0.061 ± 0.008
4	GRM188R61A106KE69D	Murata	Capacitor	
1	RK73H2BTTD1002F	KOA	Resistor	
1	ERA3AEB6041V	Panasonic	Resistor	
1	RK73H1JTTD1002F	KOA	Resistor	
1	CT262K	Kiyocera	Ag paste	0.1 ± 0.06
1	XRPIX5b	Lapis	ASIC	

Appendix B

Calibration of the Enviromental Data

In order to calibrate the environmental data, a ^{241}Am γ source was used, at the same temperature inside the thermal chamber. We then obtain the signal for clusters consisting of a single pixel (which are more likely to be generated by γ rays), normalize both the environmental and the Americium histograms, subtract them, and look for peaks in the resulting histogram. The original distributions, as well as the resulting spectrum after the subtraction are shown in figure B.1.

The position of the four peaks used for the fit (indicated by a red arrow in figure B.1) and their respective energy values are shown in figure B.2, together with the fit obtained. The reason there characteristic peak ath 59.6 is because clusters with this energy probably have a size bigger than 1.

The parameters of the fit are:

$$[\text{keV}] = 0.129161 \times [\text{ADU}] + 0.132144. \tag{B.1}$$

The mean error obtained with these parameters, with $N = 4$ the total number of points used for the fitting, and n the n-th point, is

$$\text{Error} = \frac{1}{N}\sqrt{\sum_{n=1}^{N} [[\text{keV}]_n - (0.129161 \times [\text{ADU}]_n + 0.132144)]^2} = 1.035 \text{ eV} \tag{B.2}$$

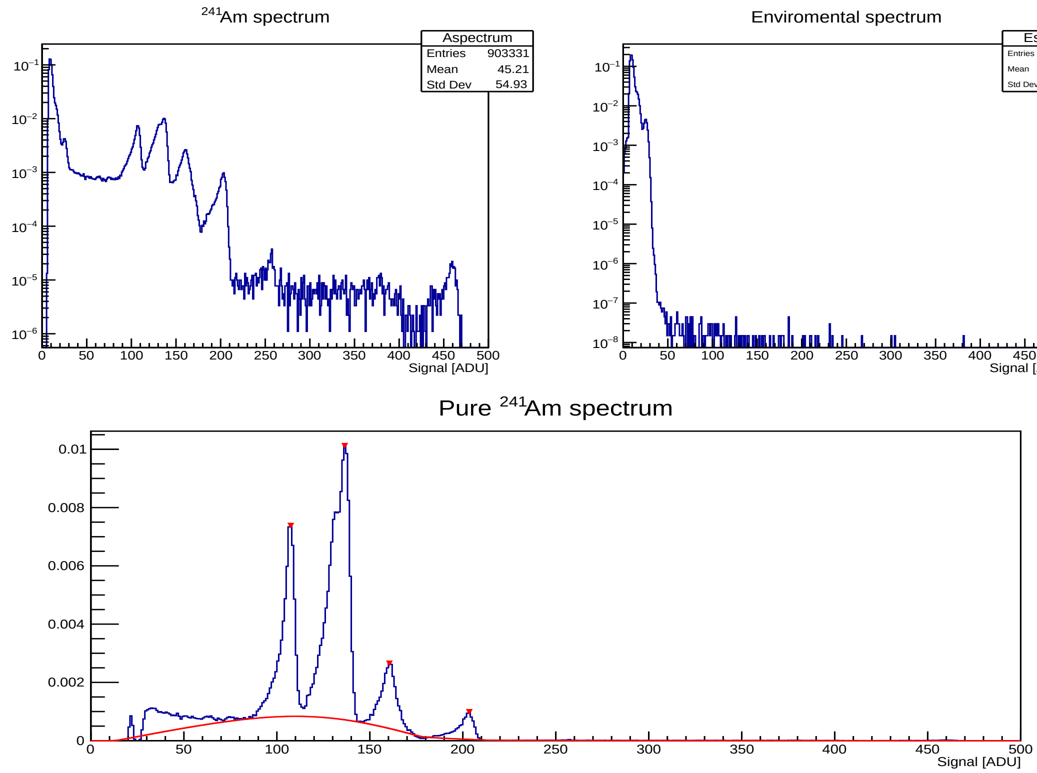

Fig. B.1 Top: ADU spectra for Americium 241 (left) and the environmental radiation inside the thermal chamber (right). *Bottom:* Histogram obtained by subtracting the environmental spectrum from the ^{241}Am original one; any negative bin was set to zero. Notice that the first two histograms are in a logarithmic scale.

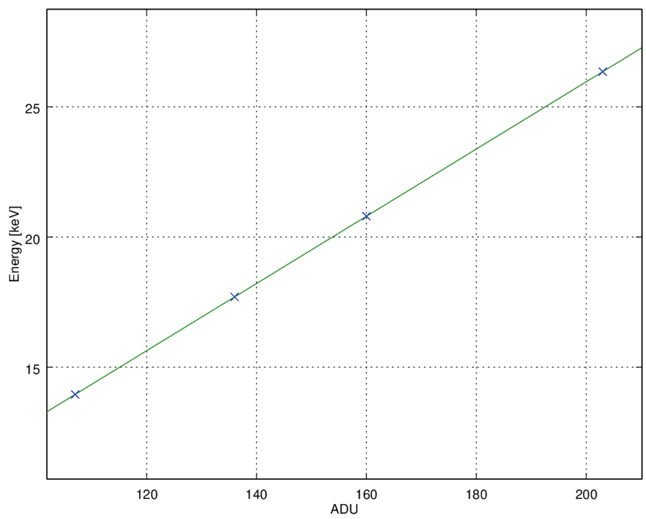

Fig. B.2 Fit used for the data calibration. The values in the *x* axis (ADU) correspond to: [107, 136, 160, 203]. The corresponding energy values are, in keV: [13.95 17.7 20.8 26.35].